Department of Physics and Astronomy

University of Heidelberg

Master thesis

in Physics

submitted

2016 by

Sebastian Hornung

born in Speyer

Study of heavy-flavour hadron production in pp collisions with ALICE

This Master thesis has been carried out by Sebastian Hornung

at the

Physikalisches Institut in Heidelberg

under the supervision of

Dr. rer. nat., Priv.-Doz. Silvia Masciocchi

Abstract

Measurements of heavy-flavour hadrons in proton-proton collisions are important to test pertubative Quantum ChromoDynamics and as a reference for measurements in heavy-ion collisions. ALICE has measured several observables in this sector, e.g. the p_{T}-differential production cross-sections of prompt D mesons and semi-electronic decays of hadrons with beauty or charm quarks at different energies. These measurements are compared to theoretical calculations, like Fixed-Order plus Next-to-Leading-Logarithms, which are affected by large systematic uncertainties introduced by the heavy-quark mass, the renormalisation and factorization scale. A possible way to reduce the systematic uncertainty on the models is to consider ratios of p_{T}-differential production cross-sections at different centre-of-mass energies. Therefore, such ratios were studied to investigate the possibility to reduce the large range of values the theoretical parameters can assume. Unfortunately, the existing data has too large uncertainties to be distinctive. Therefore, the production cross-section of electrons from decays of heavy-flavour hadrons in pp collisions at a collision energy of $\sqrt{s} = 2.76\,\mathrm{TeV}$ was measured with a new method to reduce the systematic uncertainties. The resulting cross-section and a measurement in Pb–Pb was used to improve the precision of the nuclear modification factor.

Zusammenfassung

Messungen von Heavy-Flavour Hadronen in Proton-Proton Kollisionen bieten die Möglichkeit die Ergebnisse der pertubativen QuantenChromoDynamik zu überprüfen und stellen eine wichtige Referenz für Messungen in Schwerionenkollisionen dar. Daher wurden in diesem Sektor diverse Messungen mit Hilfe des ALICE Detektors durchgeführt, z.B. wurde der p_{T}-differentielle Produktionsquerschnitt von direkten D Mesonen und semi-elektronischer Zerfälle von Hadronen mit beauty und charm Quarks bei unterschiedlichen Kollisionsenergien gemessen. Diese Messungen werden mit Berechnungen basierend auf verschiedenen Theorien vergleichen, wie zum Beispiel Fixed-Order plus Next-to-Leading-Logarithms. Die systematischen Fehler der Ergebnisse dieser Theorien ist durch die Auswahlmöglichkeiten der Renormierungs-, Faktorisierungsmaßstab und der Heavy-Quark Masse groß. Verhältnisse zwischen p_{T}-differentiellen Produktionsquerschnitten bei verschiedenen Kollisionsenergien bieten die Möglichkeit diesen Fehler einzuschränken. Daher wurden solche Verhältnisse ausgewertet, um zu untersuchen, ob der Bereich, in dem die Werte der theoretischen Parameter gewählt werden können, eingeschränkt werden kann. Leider sind die Messungenauigkeiten der Daten noch zu groß. Daher wurden der Produktionsquerschnitt von Elektronen aus semi-elektronischen Zerfällen von Hadronen mit beauty und charm Quarks in pp Kollisionen bei einer Kollisionsenergie von $\sqrt{s} = 2.76\,\mathrm{TeV}$ mit Hilfe einer neuen Methode bestimmt, um die systematischen Unsicherheiten zu reduzieren. Das Ergebnis dieser Messung und eine Pb–Pb Messungen wurden verwendet um die Genauigkeit des nuklearen Modifikationsfaktors zu erhöhen.

Contents

1. Introduction

1.1. Heavy quarks

The (bare) mass of the heavy quarks, i.e. charm and beauty, is significantly larger than the Quantum ChromoDynamics (QCD) scale parameter $\lambda_{QCD} \approx 0.2\,\mathrm{GeV}$, e.g. the mass of the beauty quark $m_b \approx 4.75\,\mathrm{GeV}/c^2$) or the charm quark ($m_c \approx 1.5\,\mathrm{GeV}/c^2$). Therefore, their production can be described theoretically via perturbative QCD (pQCD) over the full range of momenta while gluon and light quarks can only be treated perturbatively at high transverse momenta [1]. Theoretical calculations achieve reasonable accuracy because of this unique feature of the heavy-quark production. In hadronic collisions, the heavy quarks are produced in initial hard scattering processes, which are at Leading Order (LO) gluon fusion and quark-antiquark annihilation (Figure 1.1), and at Next-to-Leading Order (NLO) processes such as gluon splitting and flavour excitation have to be considered in addition [1] (Figure 1.2).

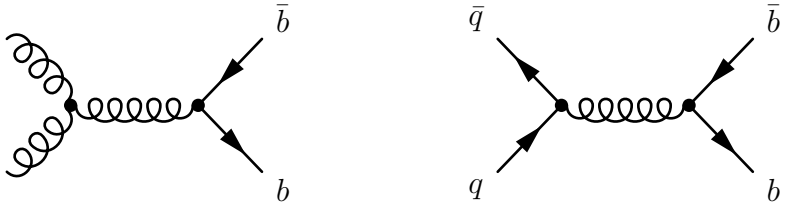

Figure 1.1: Examples for leading order Feynman diagrams for the production of a $b\bar{b}$ pair. The left diagram shows gluon fusion and the right one quark-antiquark-annihilation.

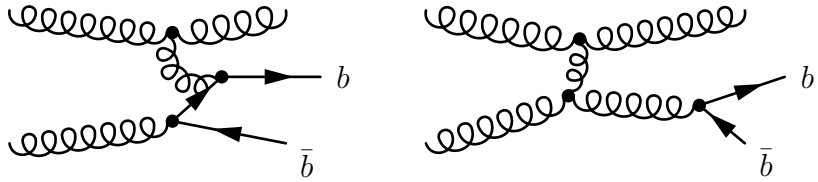

Figure 1.2: Examples for next-to-leading order Feynman diagrams for the production of a $b\bar{b}$ pair. The left diagram shows flavour excitation and the right one gluon splitting.

Heavy-flavour quarks hadronise and form relatively long-lived particles, for example D mesons. The lifetimes of the charm hadrons are in the order of 500 to 1000 fs and the lifetimes of the beauty hadrons are about 1500 fs. Measurements of the production cross-section of beauty and charm in pp collisions can be compared to pQCD calculations to check our understanding of the underlying processes. In addition, these measurements provide an important reference for the measurements in Pb–Pb collisions, where the de-confined state of matter, the Quark-Gluon-Plasma, is expected to be formed. The measurements of heavy-flavour hadron decays can be performed in two different ways. Either the hadron is fully reconstructed directly via its decay products, e.g. hadronic decay $D^0 \rightarrow K^-\pi^+$, or measurements of electrons and muons from heavy-flavour hadron decays are performed. The first method is affected by a large combinational background while the measurements in the lepton channels have to handle with a hugh electron background from various other sources, like π^0 Dalitz-decays. These background contributions have to be evaluated and subtracted. Until now the theory describes the data very well but it is affected by large uncertainties. The measurements for observables linked to the charm and beauty quark tend to be at the upper edge of the FONLL [2, 3] calculations, see e.g. Figure 4.1 or Figure 1.4.

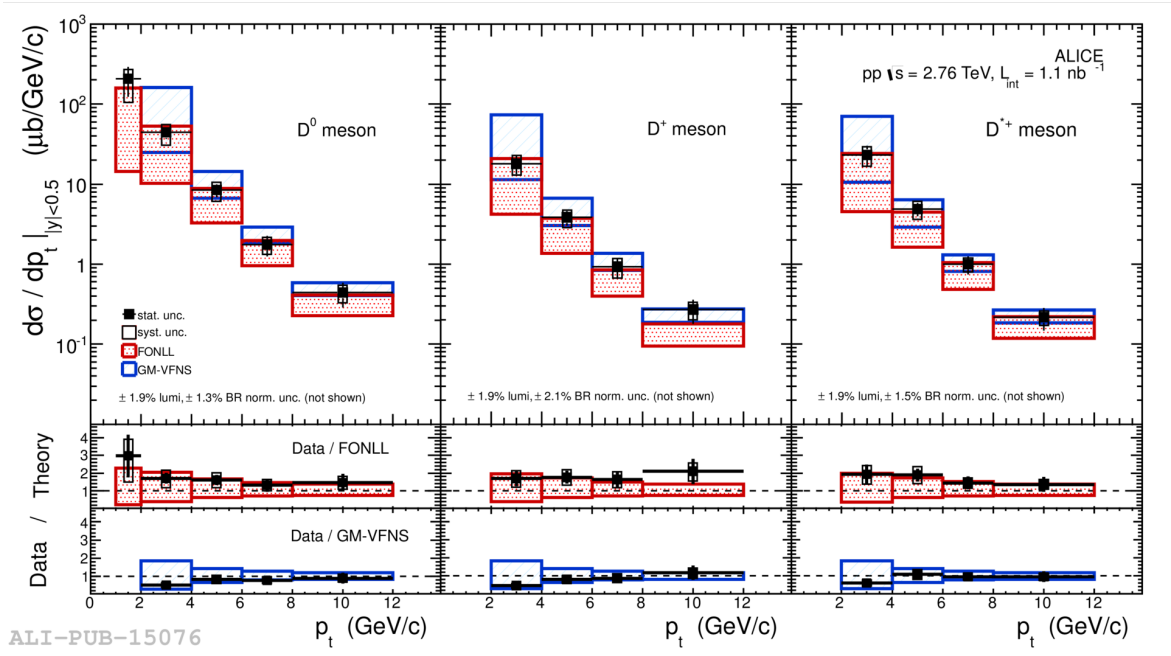

Figure 1.3: Top : p_{T}-differential cross-section for prompt D^0, D^+ and D^{*+} mesons in pp collisions at $\sqrt{s}$ = 2.76 TeV compared with FONLL [2, 3] and GM-VFNS [4, 5] theoretical calculations. Bottom: The ratio of the measured cross-section and the central FONLL and GM-VFNS calculations. This plot is taken from [6].

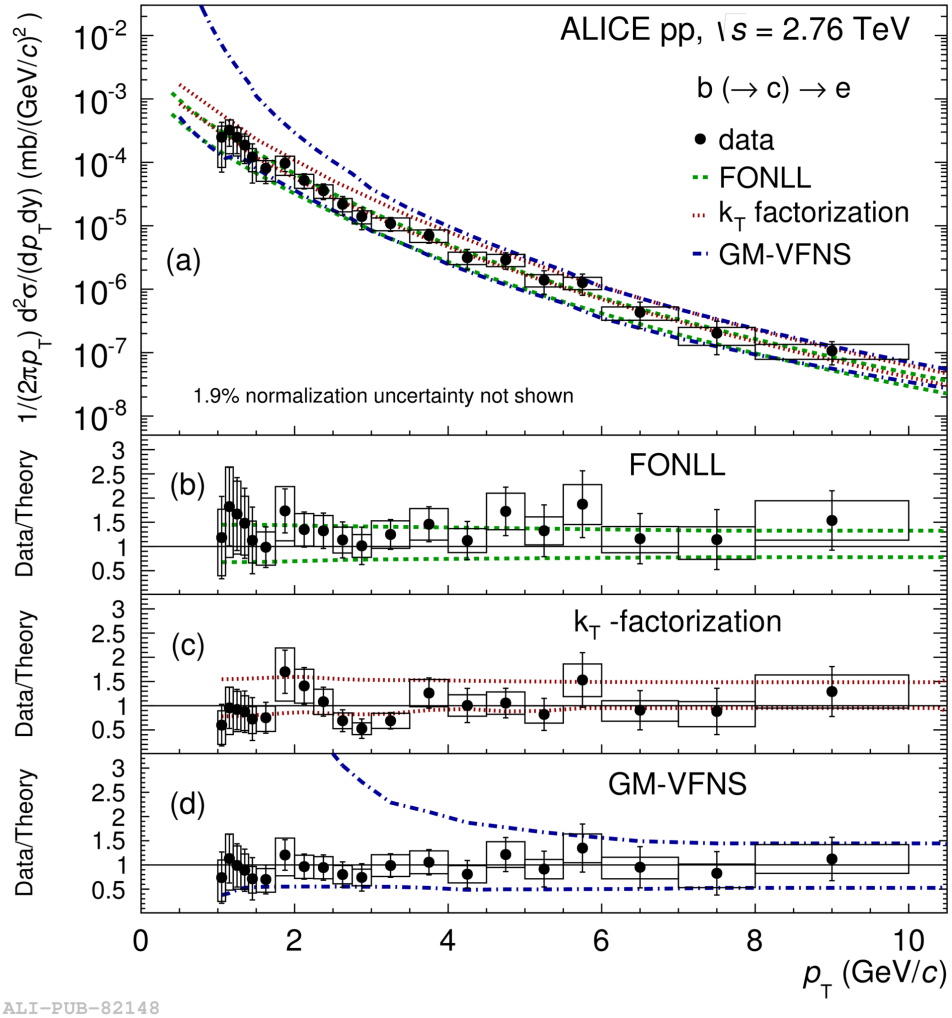

Figure 1.4: (a) p_{T}-differential inclusive production cross-section of electrons from beauty hadron decays. The green dashed, red dotted, and blue dot-dashed lines represent the FONLL [2, 3], kT-factorization [7], and GM-VFNS [4, 5] uncertainty range, respectively. (b)-(d) Ratios of the data and the central calculation of pQCD calculations for electrons from beauty hadron decays. For all panels, the error bars (boxes) represent the statistical (systematic) uncertainties. This plot is taken from [8].

This behaviour indicates that the measurements could provide information about the FONLL parameters. Therefore, we tried to use these measurements to reduce the range of the FONLL parameter and, hereby, decrease the FONLL uncertainty bands. The spread of the FONLL curves for the different scale choices is discussed briefly in subsection 3.1.2.
A brief description of the ALICE detector can be found in chapter 2, where only the sub-

detectors used for the analysis descripted in chapter 6 are discussed in detail. The third chapter deals with the theoretical description of the analysed processes. Not only the basic steps to calculate or simulate the cross-sections are shown but also a study of the different sources of uncertainties. In chapter 4 the published data used in this thesis are described. The ratios of differential cross-sections at different centre-of-mass energies is calculated and discussed in chapter 5. In chapter 6, the cross-section of the electrons from semi-electronic decays of heavy-flavour hadrons at 2.76 TeV is measured using the method of tagging of the electrons from photonic background.

2. The ALICE Detector

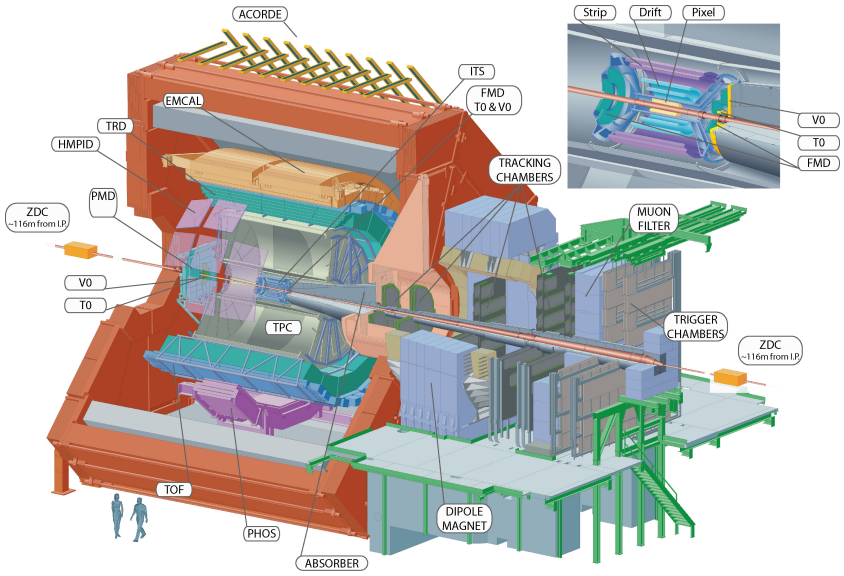

Figure 2.1: The ALICE detector is built up of 18 different detectors which are indicated by their acronyms. The central detectors (left side) are mounted inside the large solenoid magnet which had already been part of the L3 detector at LEP. The Muon spectrometer with its dipole magnet is placed in forward direction (right side). An additional blow-up of the innermost region, showing the Inner Tracking System, the forward trigger and the multiplicity detectors, was added on the top right position. This picture is taken from [9].

ALICE is one of the four main experiments at the Large Hadron Collider (LHC) at CERN. It was primarily designed for data taking at heavy-ion collisions which is indicated by the fact that the name is an acronym for ”A Large Ion Collider Experiment”.

The standard coordinate system in ALICE is a right-handed Cartesian coordinate system where the origin is fixed by the interaction point. The z axis is aligned to the beam pipe and the x axis points to the centre of the LHC. ϕ is the azimuthal angle around the z axis and θ

is the polar angle with respect to the beam axis. The polar angle is often expressed in terms of pseudorapidity η. The two quantities are linked via Equation 2.1.

$$\eta = \frac{1}{2} \ln \left(\frac{p + p_z}{p - p_z} \right) \equiv - \ln \left[\tan \left(\frac{\theta}{2} \right) \right] \tag{2.1}$$

The ALICE detector has an overall size of 16 × 16 × 26 m^3 and a total weight of about 10 000 t and was optimized to cope with the high particle densities expected from heavy-ion collisions. It can be divided into two parts: the central-barrel detectors and the MUON spectrometer. The MUON spectrometer covers the range of $-4 < \eta < -2.5$ and is used for measurements of muons, quarkonia and light vector mesons. The very heart of ALICE are the central-barrel detectors which are covering the midrapidity region ($|\eta| < 0.9$). They are embedded in the L3 solenoid magnet providing a uniform magnetic field of 0.5 T along the beam direction. These detectors are the Inner Tracking System (ITS), the Time Projection Chamber (TPC), the Transition Radiation Detector (TRD), the Time Of Flight detector (TOF), the Photon Spectrometer (PHOS), the Electromagnetic Calorimeter (EMCal) and High Momentum Particle Identification Detector (HMPID) [10]. Inside the central region there are three additional detectors, the Forward Multiplicity Detector (FMD), V0 and T0. These detectors are used to determine the number of particles produced in the collision and their spatial distribution. T0 is also used to measure the time when the collision has taken place very precisely.
The ALICE detector is described in full details in [11]. In the following sections, more detailed information about the sub-detectors needed for the analysis presented in chapter 6 is given.

2.1. Inner Tracking System (ITS)

The ITS is the innermost detector system of the central barrel and is built up of six cylindrical layers with three different types of silicon detectors. At radii of 3.9 cm and 7.6 cm from the beam axis, the two innermost layers are mounted, the Silicon Pixel Detectors (SPD). These provide a very good spatial resolution in the transverse plane (12 µm) and in the beam direction (100 µm) [12]. The SPD layers are of central importance for the reconstruction of primary and secondary vertices and for determining the distance of closest approach to the primary vertex of reconstructed tracks. Both aspects are essential for the current way of analysing heavy-flavour hadron decays. The intermediate and outer layers consist of Silicon Drift Detectors (SDD) and double-sided Silicon Strip Detectors (SSD) at radii between 15 cm

and 43 cm. These two parts are also capable of providing particle identification information via deposited energy. The ITS provides spatial resolution information (tracking) for charged particles near the beam pipe [12] and contributes to the high momentum and angular resolution of particle trajectories at ALICE.

2.2. Time Projection Chamber (TPC)

The main tracking detector of ALICE is the TPC. It provides momentum and particle identification information. The TPC is a cylindrical drift detector with a length of 5 m and a diameter of 5.6 m covering a pseudorapidity range of $|\eta| = 0.9$. During all the runs which are relevant for this thesis, it was filled with Ne (85.5%), CO_2 (9.5%) and N_2 (4.8%). The TPC is divided into two drift regions by a central high-voltage electrode and the readout is divided into 159 pad rows in radial direction [13]. Charged particles, passing through it, ionize the gas molecules and, thereby, free electrons. These electrons drift towards the end plates of the TPC which are equipped with multi-wire proportional chambers [12]. The coordinates transverse to the beam direction are given by the signal position at the end-cap while the third dimension is reconstructed via the drift time. The TPC is one of the main detectors for particle identification which is determined by the specific energy loss per unit length $\left(\frac{dE}{dx}\right)$ given by the collected charge.

2.3. Time of Flight detector (TOF)

The TOF is a gas detector consisting of Multigap Resistive Plate Chamber (MRPCs), a type of detector developed to meet the requirements of time resolution and number of read-out channels [9]. It contains more than 150 000 individual cells with an area of $2.5 \times 3.5\,cm^2$ at a radius of 3.7 m [12] from the beam axis covering $|\eta| = 0.9$ and the full azimuth. The TOF array provides additional information for particle identification by measuring the flight time of the individual particles between the collision and the point were it is mounted. The moment of collision is determined by the T0 detector, which is an array of quartz Cherenkov counters positioned at $+370$ cm and -70 cm along the beam axis, if it is available [12]. If this information is not available, the collision time is estimated using the arrival time of the particles in the TOF or the bunch crossing time from the LHC. The resolution of the particle arrival time is better than 100 ps which results in an overall time of flight resolution of about 150 ps. Using the time of flight and the momentum of a particle, one can determine its mass

and therefore identify the particle. The particle identification information provided by the TOF detector complements the particle identification capability of the TPC.

3. Theoretical calculations and simulations

The essential parameters of theoretical calculations and simulations are:

- the heavy-quark masses,
- the Parton Distribution Functions (PDFs),
- the renormalisation and factorisation scales.

In this thesis, $m_{\mathrm{c}} = 1.5\,\mathrm{GeV}/c^2$ is used for charm quarks and $m_{\mathrm{b}} = 4.75\,\mathrm{GeV}/c^2$ for beauty quarks, because these are the default values for FONLL [2] and POWHEG [14]. Additional parameters like the renormalisation and factorisation scale are chosen in line with common practice. Hence, the transverse mass of the heavy-quark was set as the central value $\mu = m_T = \sqrt{m^2 + p_{\mathrm{T}}^2}$. To estimate the systematic uncertainties introduced by these parameters, the calculations and simulations are repeated varying the values of the heavy-quark masses and renormalisation and factorisation scales. The charm quark mass was varied from $1.3\,\mathrm{GeV}/c^2$ to $1.7\,\mathrm{GeV}/c^2$ and the beauty quark mass from $4.5\,\mathrm{GeV}/c^2$ to $5.0\,\mathrm{GeV}/c^2$. The factorisation and renormalisation scales were varied using the 7-point scale variation:

$$(\mu_R, \mu_F) = [(0.5, 0.5), (1, 0.5), (0.5, 1), (1, 1), (1, 2), (2, 1), (2, 2)] \cdot m_T. \tag{3.1}$$

The calculations and simulations reported in this thesis are computed using the set of PDF called CTEQ6.6 as default. The systematic uncertainties related to this choice of PDFs were obtained by repeating them for the full error set of these PDFs. The full uncertainty band was calculated adding the uncertainties from mass, scales and PDFs in quadrature.

3.1. FONLL

3.1.1. Basic concept

The Fixed-Order plus Next-to-Leading-Logarithms (FONLL) calculations are based on a factorisation approach developed by Matteo Cacciari, Paolo Nason and Mario Greco [2]. The cross-section of a particle l is obtained by numerical convolution of the perturbative cross-section of the heavy-quark Q ($\mathrm{d}\sigma_Q^{FONLL}$), a non-perturbative fragmentation function ($D^{NP}_{Q\to H_Q}$) and decay function ($g_{H_Q\to l}$)

$$\mathrm{d}\sigma_l^{FONLL} = \mathrm{d}\sigma_Q^{FONLL} \otimes D^{NP}_{Q\to H_Q} \otimes g_{H_Q\to l}. \tag{3.2}$$

The perturbative cross-section is obtained by matching fixed next-to-leading order (NLO) QCD with all-order resummation up to next-to-leading log (NLL) accuracy [3]. This is done according to the following prescription

$$\mathrm{d}\sigma_{\mathrm{FONLL}} = \mathrm{d}\sigma_{\mathrm{FO}} + (\mathrm{d}\sigma_{\mathrm{RS}} - \mathrm{d}\sigma_{\mathrm{FOM0}}) \times G(m, p_{\mathrm{T}}). \tag{3.3}$$

$\mathrm{d}\sigma_{\mathrm{FO}}$ is the massive NLO cross-section in which the mass of the heavy-quark is kept as a non-vanishing parameter and its flavour enters only in the partonic scattering through flavour creation processes, but not in the PDFs. $\mathrm{d}\sigma_{\mathrm{FO}}$ matches the terms up to order α_s^3 in the resummed approach. To subtract from the resummed cross-section in massless limit ($\mathrm{d}\sigma_{\mathrm{RS}}$) the fixed-order terms already contained in the FO, an approximation to the latter where only logarithmic mass terms are retained ($\mathrm{d}\sigma_{\mathrm{FOM0}}$), is used [2]. $G(m, p_{\mathrm{T}})$ is a matching function which tends to unity in the massless limit $p_{\mathrm{T}} \gg m$, where FO approaches the afore mentioned approximation of the fixed-order terms in the massless limit, FOM0, and its functional form is

$$G(m, p_{\mathrm{T}}) = \frac{p_{\mathrm{T}}^2}{p_{\mathrm{T}}^2 + a^2 m^2}, \tag{3.4}$$

with $a = 5$, because the difference $\mathrm{d}\sigma_{\mathrm{RS}} - \mathrm{d}\sigma_{\mathrm{FOM0}}$ turned out to be abnormally large below $p_{\mathrm{T}} = 5m$ [15]. For the resummation formalism the pertubative fragmentation functions (pFF) for the parton i into a heavy-quark h are needed. Here i runs over all light partons (the light quarks and anti-quarks, and the gluon), as well as the heavy-quarks and anti-quarks. These fragmentation functions satisfy the Altarelli-Pairisi evolution equations and

their initial values at a given scale μ_0 are calculable pertubatively. In the modified minimal subtraction ($\overline{MS}$) scheme they are given by

$$D_h(x,\mu_0) = \delta(1-x) + \frac{\alpha_s(\mu_0)\,C_F}{2\pi}\left[\frac{1+x^2}{1-x}\left(\log\frac{\mu_0^2}{m^2} - 2\log(1-x) - 1\right)\right]_+, \tag{3.5}$$

$$D_g(x,\mu_0) = \frac{\alpha_s(\mu_0)\,T_F}{2\pi}(x^2+(1-x)^2)\log\frac{\mu_0^2}{m^2}, \tag{3.6}$$

$$D_i(x,\mu_0) = 0, \text{ for } i{\neq}g,h. \tag{3.7}$$

The first term describes the probability of a heavy-quark h to go into a heavy-quark h'. The second term refers to the gluon-splitting contribution $g \to h\bar{h}$ and the third term is related to the coupling of light to heavy quarks, which occurs only at next-to-next-to-leading order and is therefore neglected. As usual, the first group invariant of the colour algebra T_F is $\frac{1}{2}$ and the second C_F is $\frac{4}{3}$.
The pFFs are evolved to factorisation scale μ_F and convoluted with the NLO cross-section for massless partons and $D^{NP}_{Q\to H_Q}$. $D^{NP}_{Q\to H_Q}$ is a non-perturbative fragmentation function which describes the hadronisation of the heavy quarks into heavy-flavour hadrons. These functions for beauty and charm are based on a fit to LEP data [16, 17]. The integral of these fragmentation functions is called fragmentation fraction. If needed, a function ($g_{H_Q\to l}$) referring to the decay of the heavy-flavour hadron to the particle l has to be used [3, 15]. The decay functions and branching ratios are extracted from experimental data. FONLL can only yield calculations for one-particle inclusive heavy-quark distributions because the degrees of freedom linked to the other particle are integrated over. Hence, it is not possible to study correlations of the produced heavy-flavour quark or hadron with other objects in the final state.

3.1.2. Spectra and uncertainties

The FONLL calculations were obtained using the published framework [18]. An overview of the parameters used can be found in Table A.1. The FONLL calculations were performed in p_{T}-steps of 0.1 GeV/c. The FONLL calculations for the p_{T}-differential cross-section of the charm quark via reconstruction of D^0, D^+ and D^{*+} at $\sqrt{s} = 7$ TeV at midrapidity (|y|<0.5) are shown in Figure 3.1. The corresponding plot for the cross-section at $\sqrt{s} = 2.76$ TeV can be found in the appendix, Figure A.1.

From second panel of the afore mentioned figures, it is evident, that the FONLL uncertainty band is driven by the variation of the factorisation and renormalisation scale. The

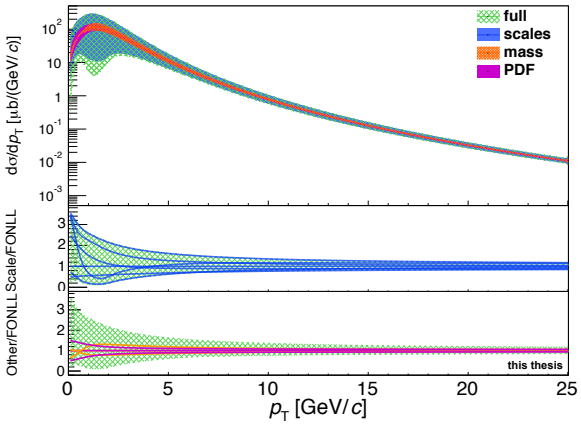

(a) FONLL band and single curves for D^0

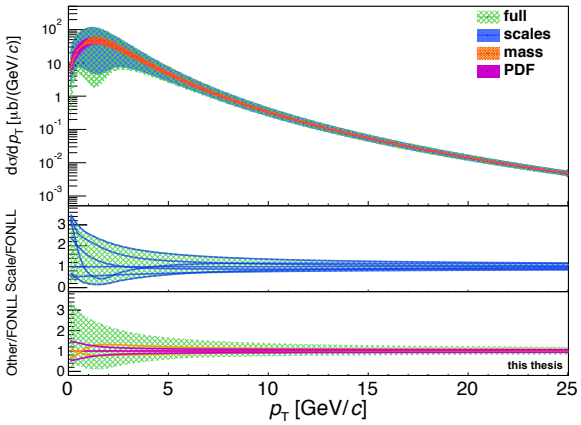

(b) FONLL band and single curves for D^+

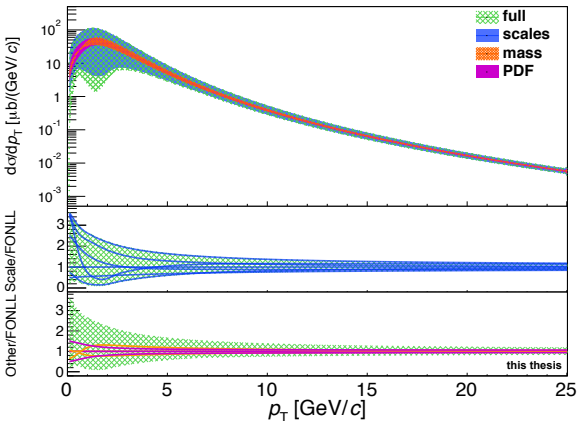

(c) FONLL band and single curves for D^{*+}

Figure 3.1: The calculations for the p_T-differential cross-section of D^0, D^+ and D^{*+} at $\sqrt{s} = 7$ TeV obtained within the FONLL framework. The uncertainties introduced by the scales, the quark mass and the PDFs are shown as blue, orange and violet band, respectively. The full uncertainty band is shown in green. The two pads below show the ratios of the scale and mass variation, as well as, the curves belonging to the maximum and minimum deviations caused by the PDF uncertainties to the central value of FONLL.

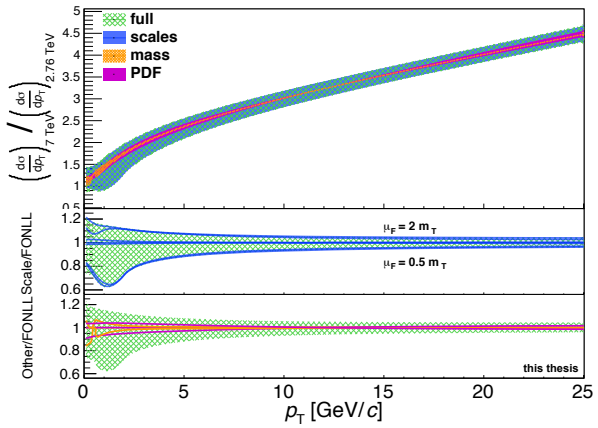

(a) FONLL band and single curves for D^0

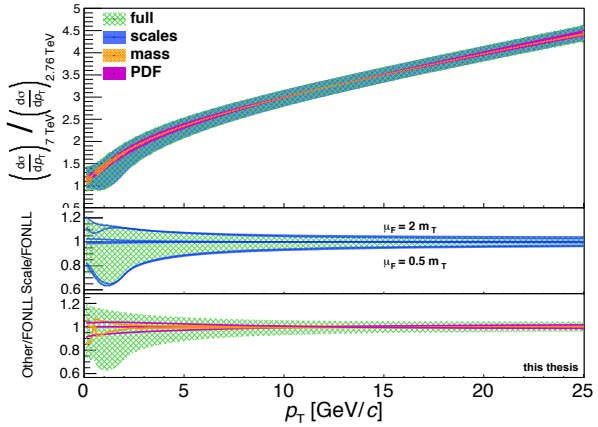

(b) FONLL band and single curves for D^+

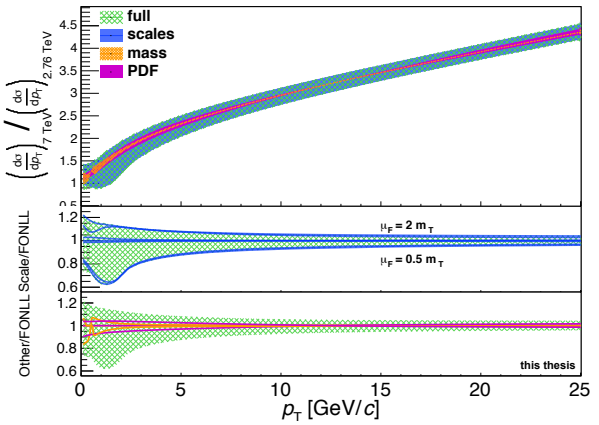

(c) FONLL band and single curves for D^{*+}

Figure 3.2: The ratio of the calculations for the p_T-differential cross-section of D^0, D^+ and D^{*+} at $\sqrt{s} = 7\,\text{TeV}$ and $\sqrt{s} = 2.76\,\text{TeV}$ obtained within the FONLL framework. The uncertainties introduced by the scales, the quark mass and the PDFs are shown as blue, orange and violet band, respectively. The full uncertainty band is shown in green. The two pads below show the ratios of the scale and mass variation, as well as, the curves belonging to the maximum and minimum deviations caused by the PDF uncertainties to the central value of FONLL.

curves belonging to the different parameter values fill the FONLL band in a way that it is hard to disfavour any parameter value on a three sigma level. The FONLL authors propose that the ratios of such cross-sections at different collision energies gain more insights on the different parameters [19]. Figure 3.2 shows the ratios of the calculations for the cross-section of D^0, D^+ and D^{*+} at $\sqrt{s} = 7\,\text{TeV}$ divided by the ones at $\sqrt{s} = 2.76\,\text{TeV}$. Hereby, the ratios were evaluated for each choice of the parameters separately because these are considered fully correlated at different energies [19]. The curves for the different choices of the scales group according to the choice of the factorisation scale which clearly helps to exclude specific choices for this scale, see panel (b) of Figure 3.3. An exclusion of a combination of parameter values using the ratio would be easier but this requires high precision data because the width of the FONLL band itself decreases by about a factor of six. In addition, the FONLL uncertainty band on the single measurements at one specific energy will not be reduced by much because there the FONLL band is not driven by the factorisation scale but by the factor between the two scales, see panel (a) of Figure 3.3.

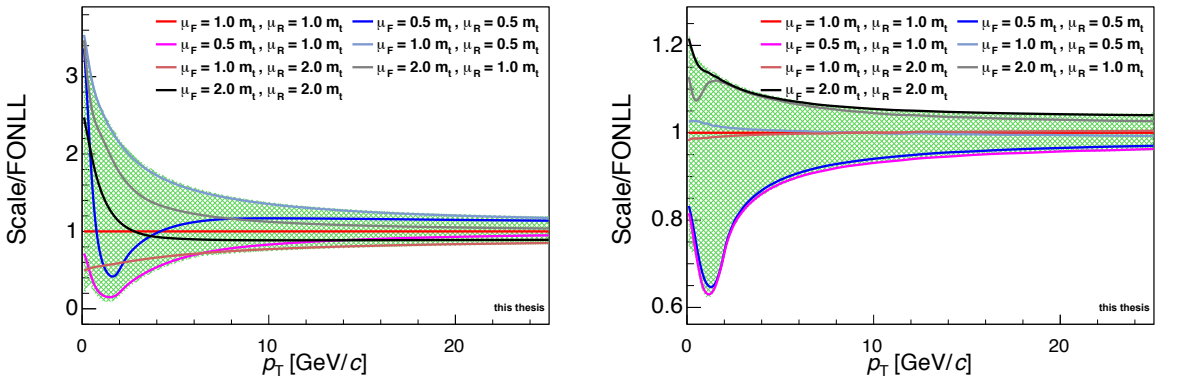

(a) FONLL scale curves at $\sqrt{s} = 7\,\text{TeV}$

(b) FONLL scale curves for the ratio of $\sqrt{s} = 7\,\text{TeV}$ to $\sqrt{s} = 2.76\,\text{TeV}$

Figure 3.3: The FONLL calculation of the cross-section of D^0 at $\sqrt{s} = 7\,\text{TeV}$ (a) and the ratio of the cross-section at $\sqrt{s} = 7\,\text{TeV}$ and $\sqrt{s} = 2.76\,\text{TeV}$ with its full uncertainty band (green) and the curves belonging to the different choices of the factorisation and renormalisation scale.

For the calculations with electronic final state, the differential cross-sections were computed according to

$$\left.\frac{1}{2\pi p_T}\frac{d^2\sigma^{e^\pm}}{dp_T dy}\right|_{|y|<0.5} = \left.\frac{1}{2\pi p_T}\frac{d\sigma^{e^\pm}}{\Delta y\, dp_T}\right|_{|y|<0.5}. \tag{3.8}$$

The results from direct semi-electronic decay of beauty hadrons and decays via charm hadrons were added up. The corresponding plots for the cross-sections of semi-electronic decay of beauty and charm hadrons can be found in the appendix, Figure A.2, Figure A.3 and Figure A.4.

3.2. POWHEG

The POsitive Weight Hard Event Generator (POWHEG) [14] can be used to generate events with heavy-flavour (top, beauty or charm) quark anti-quark pairs, which can be fed through any Shower Monte Carlo program that compiles with the requirements of the Les Houches Interface for User Processes [20], like PYTHIA [21, 22], to generate complete events. Therefore, this approach is not limited to inclusive production but offers a more complete description of the final state, including decay kinematics, particle identification and, if needed, detector response. The precision of POWHEG is NLO in the hard and leading-logarithm accuracy in the soft/collinear regime by consistent combination of NLO calculation with parton showers. In the POWHEG approach, the massive quarks are not active partons in the PDFs and large logarithms are not resummed into heavy-quark PDFs. The production mechanism for heavy-flavour quarks are flavour-excitation in the initial-state parton shower or gluon splitting. In contrast to FONLL, only a subset of large logarithms are resummed because of complex colour flow in parton-parton scattering which lead to only leading-logarithm accuracy of the Sudakov form factor for light partons [15]. For this thesis, POWHEG BOX V1 and PYTHIA 6.4 with Perugia 2011 tune [23] were used to produce the charm and beauty events and then shower, hadronise and decay them to stable particles. Note, that Pythia uses the Lund string model for hadronisation which is tuned to data at leading, not next-to-leading order accuracy. An overview of the parameters used for POWHEG-Box can be found in Table A.2.

3.2.1. Event selection and yield extraction

Events having a primary vertex which is displaced by more than 10 cm were rejected, as well as events with a multiplicity above 5 000 particles. The POWHEG events were analysed in order to evaluate the yield of D mesons multiplied by the respective event cross-section in between 0 GeV/c and 40 GeV/c. The values were stored depending on the particle type, transverse momentum, polar angle and rapidity. The full range of the polar angle was used, while the rapidity was restricted to the range from -2 to 2. For the D meson analysis, D^0, D^+ and D^{*+} were identified in each event and it was checked if they really belong to a charm quark by tracing back up to quark level. Most of the D mesons came from charm quarks, only about 0.6% were feed-down from beauty and about 5‰ belong neither to charm nor to beauty. Even though these non-charm and non-beauty D mesons were unexpected their contribution is low enough to reject them without introducing any bias in the analysis. The particle type, transverse momentum, polar angle and rapidity of the remaining D mesons

were stored weighted by the event cross-section.
The POWHEG simulation for electrons from heavy-flavour hadron decays was not performed for this thesis to save computing resources, knowing already from [15] that POWHEG will not describe the data more accurate than FONLL does.

3.2.2. Simulated production cross-sections

The yields times the event cross-sections were transformed into differential cross-sections by integrating over the polar angle and from -0.5 to 0.5 in rapidity. Then the differential cross-section was calculated by dividing by the number of events, the p_{T}-binwidth ($0.2\,\mathrm{GeV}/c$) and a factor of 2 coming from the averaging of anti-particle and particle, as well as, multiply by a factor of 1000 to go from mb to μb, as reported in Equation 3.9.

$$\frac{\mathrm{d}\sigma}{\mathrm{d}p_{\mathrm{T}}} = \left.\frac{\mathrm{N}_{\mathrm{D}/\bar{\mathrm{D}}}}{2\Delta\mathrm{y}\Delta p_{\mathrm{T}}}\right|_{|\mathrm{y}|<0.5} \cdot \frac{\sigma_{\mathrm{event}}}{\mathrm{N}_{\mathrm{events}}} \tag{3.9}$$

The uncertainties on the POWHEG values were determined by variation of the heavy-quark masses, the renormalization and factorization scale using the already mentioned 7-point scale variation. The upper and lower uncertainties on the POWHEG cross-section was determined by taking the maximum and minimum of all the values calculated with the different variation settings per bin, respectively. After rebinning the maximum and minimum variation values to the binning of the measurement at the respective centre-of-mass energy, the uncertainties were given by subtracting the central value. The POWHEG results for the cross-sections are compared to the measured data and the FONLL calculation. Figure 3.4 shows the cross-sections at 7 TeV, the corresponding plots for 2.76 TeV can be found in the appendix Figure A.5.

All cross-section results match the data and the FONLL calculations within the uncertainty bands, but the data has a tendency to lie at the upper edge of the FONLL band.

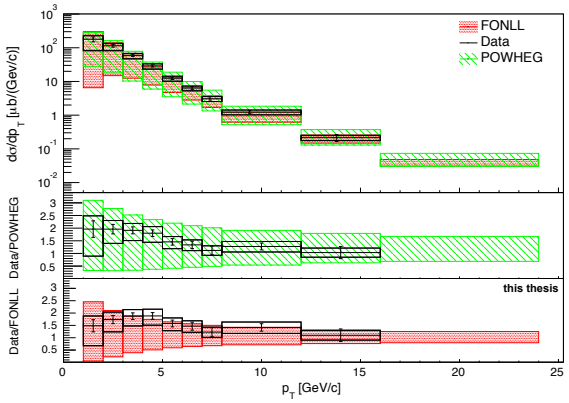

(a) p_{T}-differential cross-section for D^0

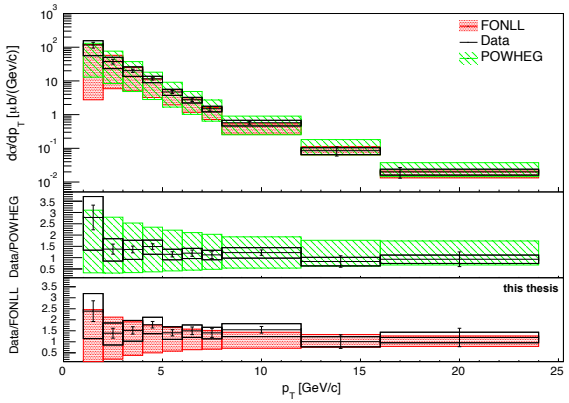

(b) p_{T}-differential cross-section for D^+

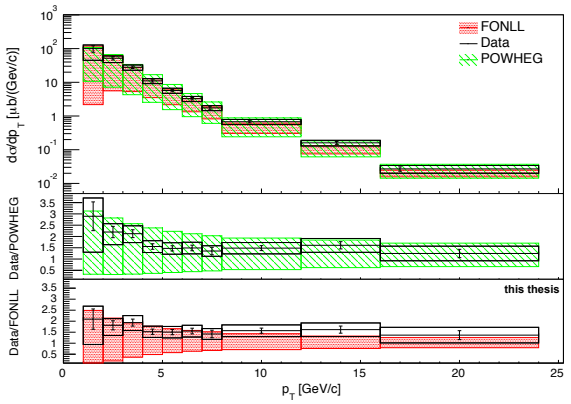

(c) p_{T}-differential cross-section for D^{*+}

Figure 3.4: Comparison of the measured p_{T}-differential cross-section of D^0, D^+ and D^{*+} production at $\sqrt{s} = 7\,\mathrm{TeV}$ to FONLL calculations (red) and POWHEG simulations (green). The two panels below show the ratios of data to the central value of POWHEG and FONLL. In all panels, the statistical and systemtical uncertainties are represented by the bars and boxes, respectively.

4. Published ALICE data

Table 4.1: Overview of published measurements of the charm and beauty cross-sections from ALICE

Measurement	Energy	L_{int}	|y|	p_T	reference
D mesons	2.76 TeV	$1.1\,\mathrm{nb}^{-1}$	0.5	$1 - 12\,\mathrm{GeV}/c$	[6]
D mesons	7 TeV	$5\,\mathrm{nb}^{-1}$	0.5	$1 - 24\,\mathrm{GeV}/c$	[24]
$H_{b/c} \to e$	2.76 TeV	$1.1\,\mathrm{nb}^{-1}$	0.8	$0.5 - 12\,\mathrm{GeV}/c$	[13]
$H_{b/c} \to e$	7 TeV	$2.6\,\mathrm{nb}^{-1}$	0.5	$0.5 - 8\,\mathrm{GeV}/c$	[12]
$H_b \to e$	2.76 TeV	$0.9\,\mathrm{nb}^{-1}$	0.8	$1 - 10\,\mathrm{GeV}/c$	[8]
$H_b \to e$	7 TeV	$2.2\,\mathrm{nb}^{-1}$	0.8	$1 - 8\,\mathrm{GeV}/c$	[25]
$H_b \to J/\psi$	7 TeV	$5.6\,\mathrm{nb}^{-1}$	0.9	$1.3 - 10\,\mathrm{GeV}/c$	[26]
D_s^+	7 TeV	$4.8\,\mathrm{nb}^{-1}$	0.5	$2 - 12\,\mathrm{GeV}/c$	[27]
c vs multiplicity	7 TeV	$\simeq 5\,\mathrm{nb}^{-1}$	0.5	$1 - 20\,\mathrm{GeV}/c$	[28]
b vs multiplicity	7 TeV	$\simeq 5\,\mathrm{nb}^{-1}$	0.9	$> 1.3\,\mathrm{GeV}/c$	[28]

The analysis discussed in this thesis requires measurements of the same observable at two different collision energies in a comparable rapidity range. Therefore, only the D meson measurements and the measurements of electrons from semi-electronic decays of hadrons carrying charm or beauty quarks can be used. These measurement are briefly described in the following sections.

4.1. D meson analyses

The p_T-differential cross-sections of prompt, i.e. feed-down subtracted, charmed mesons were measured via reconstruction of their hadronic decays $D^0 \to K^-\pi^+$, $D^+ \to K^-\pi^+\pi^+$ and $D^{*+} \to D^0\pi^+$ and their charged conjugates [24, 6]. These measurements were performed in the rapidity range $|y| < 0.5$ and for transverse momenta in the range $1 < p_T < 12\,\mathrm{GeV}/c$ at 2.76 TeV and $1 < p_T < 24\,\mathrm{GeV}/c$ at 7 TeV.

Due to their large lifetime ($c\tau \approx 123\,\mu m$ and $312\,\mu m$ for D^0 and $D^{\pm}$, respectively), the D mesons do not decay at the primary vertex. The high-precision tracking provided by the Inner Tracking System (ITS) and the Time Projection Chamber (TPC) is used to reconstruct the displaced secondary vertices. To further reduce the combinatorial background, the decay $\pi^{\pm}$ and $K^{\pm}$ are identified using the measurement of the specific energy loss dE/dx in the gas of the TPC and the time of flight of the particle from the interaction point to the Time-Of-Flight (TOF) detector. The final signal yields were extracted using an invariant mass analysis. The secondary vertex belonging to the decay $D^{*+} \rightarrow D^0\pi^+$ cannot be resolved from the primary vertex. Hence, topological selections on the D^0 and kinematic selections on the final decay products were applied. For low p_T, the additional pion is expected to have low momentum and is referred to as a 'soft pion'.
The p_T-differential cross-section for D^0 production can be calculated from the raw signal yield extracted with the invariant mass analysis via the following formula:

$$\left.\frac{d\sigma^{D^+}}{dp_T}\right|_{|y|<0.5} = \frac{1}{2}\frac{1}{\Delta y \Delta p_T}\frac{f_{\text{prompt}}(p_T)\cdot N^{D^{\pm}\text{raw}}(p_T)\Big|_{|y|<y_{\text{fid}}(p_T)}}{(\text{Acc}\times\epsilon)_{\text{prompt}}(p_T)\cdot \text{BR}\cdot L_{\text{int}}} \tag{4.1}$$

where $N^{D^{\pm}\text{raw}}(p_T)$ is the measured inclusive raw yield and f_{prompt} is the fraction of prompt mesons in the raw yield, which was obtained using the production cross-section for B mesons from FONLL pQCD calculations. More details about this can be found in [24]. The acceptance times the efficiency $(\text{Acc}\times\epsilon)_{\text{prompt}}$ accounts for the vertex reconstruction, track reconstruction and selection as well as the topological cuts [24]. It was determined using Monte Carlo simulations based on the GEANT 3 transport code [29]. Δp_T is the width of the p_T-bins used in the analysis. BR stands for the respective decay branching ratio. L_{int} is the integrated luminosity, which is given by the number of minimum bias events divided by the respective cross-section. The cross-section is given for the average over particle and anti-particle, therefore, an additional factor $\frac{1}{2}$ comes along. The results of the measurements at $\sqrt{s} = 7\,\text{TeV}$ and $\sqrt{s} = 2.76\,\text{TeV}$ are shown in Figure 4.1 and Figure 1.3, respectively.

A description of systematic uncertainties and their treatment can be found in section 4.2 of [24] and section 3.2 of [6]. The BR cancel in the calculation of ratios of differential cross-sections at two different collision energies because it is independent of the collision energy.

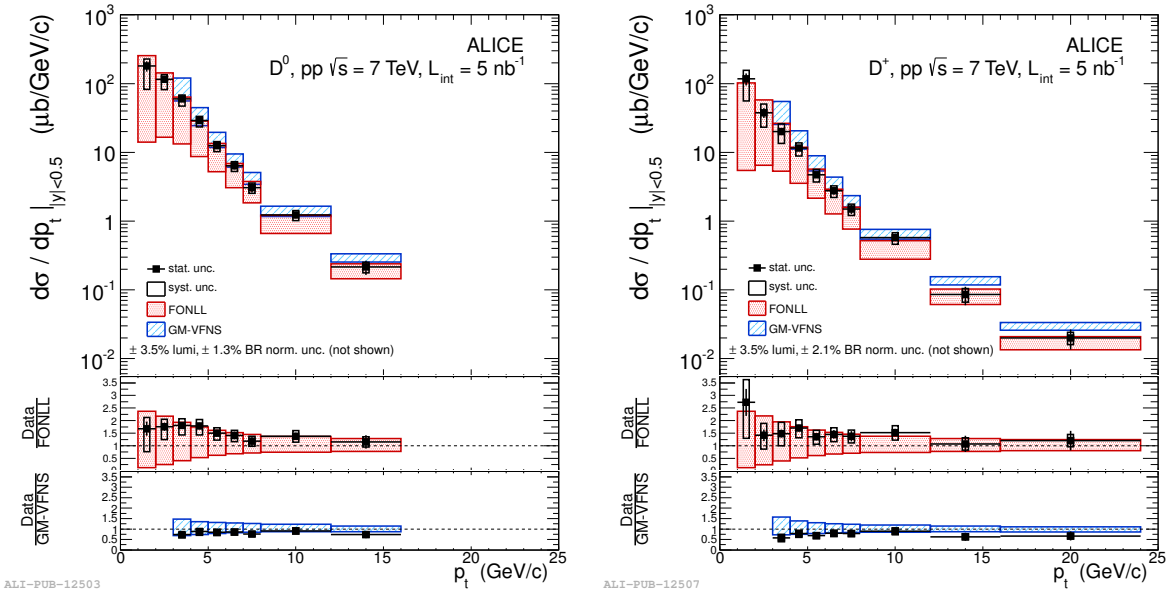

(a) D^0 (b) D^+

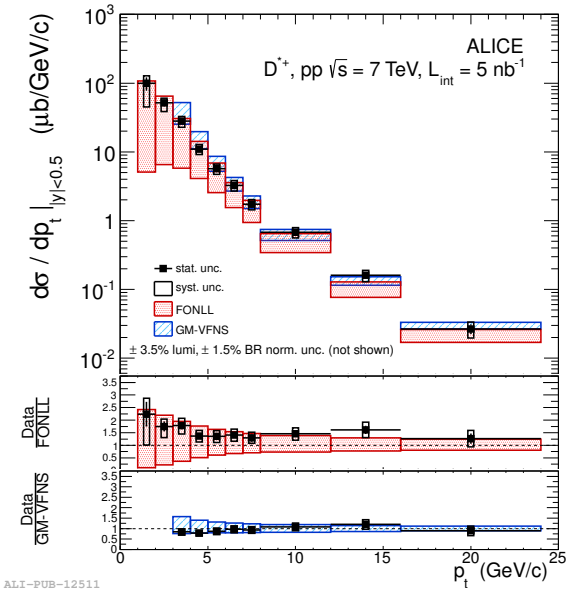

(c) D^{*+}

Figure 4.1: The p_{T}-differential cross-section for prompt D^0, D^+ and D^{*+} in pp collisions at $\sqrt{s} = 7$ TeV compared with FONLL [2, 3] and GM-VFNS [4, 5] theoretical calculations. The symbols are positioned horizontally at the centre of each p_{T} interval. The normalization uncertainty is not shown. This plot is taken from [24].

4.2. Semi-electronic decay of heavy-flavour hadrons

The p_{T}-differential cross-section of electrons from semi-electronic decays of heavy-flavour hadrons was measured in proton-proton collisions at mid-rapidity in the momentum range of $0.5 < p_{\mathrm{T}} < 8\,\mathrm{GeV}/c$ and $0.5 < p_{\mathrm{T}} < 12\,\mathrm{GeV}/c$ at 7 TeV and 2.76 TeV, respectively.
The first step was to select tracks which fulfil some electron identification cuts, e.g. specific energy loss ($\frac{\mathrm{d}E}{\mathrm{d}x}$) in the TPC between one standard deviation below and three standard deviations above the expected value of electrons and TOF-based discrimination for low momenta. A detailed description of these cuts can be found in section 3.4 of [12] and in [13]. Then corrections for acceptance and efficiency were applied. The resulting inclusive electron and positron yields per minimum bias triggered collision were averaged because the spectra of decay electron and positron are identical for all relevant sources [12]. Equation 4.2 summarizes how the yield of electrons from semi-electronic decays of heavy-flavour hadrons was calculated.

$$\frac{1}{2\pi p_{\mathrm{T}}}\frac{\mathrm{d}^2 N^{e^{\pm}}}{\mathrm{d}p_{\mathrm{T}}\mathrm{d}y} = \frac{1}{2}\frac{1}{2\pi p_{\mathrm{T}}^{\mathrm{centre}}}\frac{1}{\Delta y \Delta p_{\mathrm{T}}}\frac{N_{\mathrm{raw}}^{e^{\pm}}(p_{\mathrm{T}})}{(\epsilon^{\mathrm{geo}} \times \epsilon^{\mathrm{reco}} \times \epsilon^{\mathrm{eID}})}\frac{1}{N_{\mathrm{MB}}} \tag{4.2}$$

To remove the electron background from other sources, like Dalitz-decays of light neutral mesons, the so-called 'cocktail subtraction' method [12] was used. For the cocktail subtraction method measured momentum distributions of the relevant background sources are used and a cocktail of electrons from these is calculated using a Monte-Carlo hadron-decay generator. The cocktail contains electron distributions from the following sources:

- Dalitz-decays of light neutral mesons (π^0, η and η')
- conversion of decay photons
- dielectron decays of light vector mesons (ρ, ω and ϕ)
- dielectron decays of heavy quarkonia (J/ψ and Υ)
- weak K $\rightarrow e\pi\nu$ (K_{e3}) decays
- partonic hard scattering processes, like Drell-Yan processes and the conversion of direct real and virtual photons

A detailed description of the cocktail and its ingredients can be found in Figure 4.3. The final differential cross-sections of the electrons from semi-electronic decays of heavy-flavour

hadrons are calculated by multiplying with the minimum bias cross-section (σ_{MB}) and are shown in Figure 4.2 and Figure 4.3.

4.3. Semi-electronic decays of beauty hadrons

This measurement is similar to the measurement of electrons from semi-electronic decays of heavy-flavour hadrons because it selects electron candidates using the TPC and TOF detectors. In addition to the cocktail subtraction method, one uses the fact that beauty hadrons decay at a displaced secondary vertex because of their long lifetime ($c\tau \approx 500\,\mu\mathrm{m}$). This leads to a broad distribution of the distance of closest approach to the primary vertex, denoted as impact parameter, for the electrons coming from their decay. Therefore, a selection on the impact parameter was used to maximize the signal-to-background ratio. The remaining background was estimated using a PYTHIA [22] simulation which was re-weighted to match the p_{T}-distributions of the relevant electron sources measured with ALICE. The background cocktail surviving the selection cuts were subtracted from data. In addition, an analysis technique based the azimuthal electron-hadron correlations [13] was tested for the 2.76 TeV data. The resulting measurements are shown in Figure 1.4 and Figure 4.4. A detailed description can be found in [8] and [25].

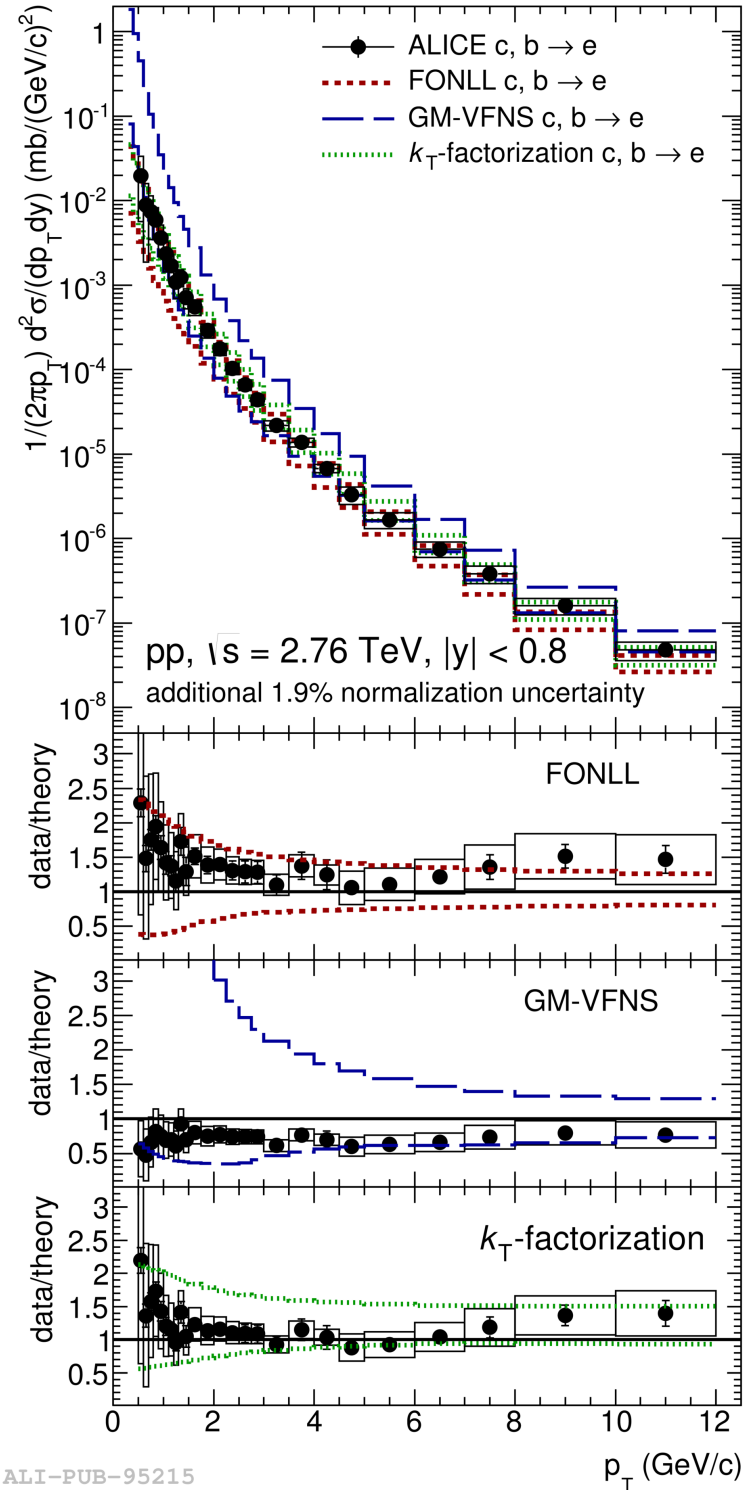

Figure 4.2: p_T-differential cross-section of electrons from heavy-flavor hadron decays compared to pQCD calculations from FONLL (red) [2, 3], GM-VFNS (blue) [4, 5] and kT-factorization (green) [7]. Uncertainties on the theory calculations originate from the variation of the factorization and the renormalization scales and from the heavy-quark masses. The ratios data/theory are shown in the lower panels, where the dashed lines indicate the additional theoretical uncertainties relative to unity. This plot is taken from [13].

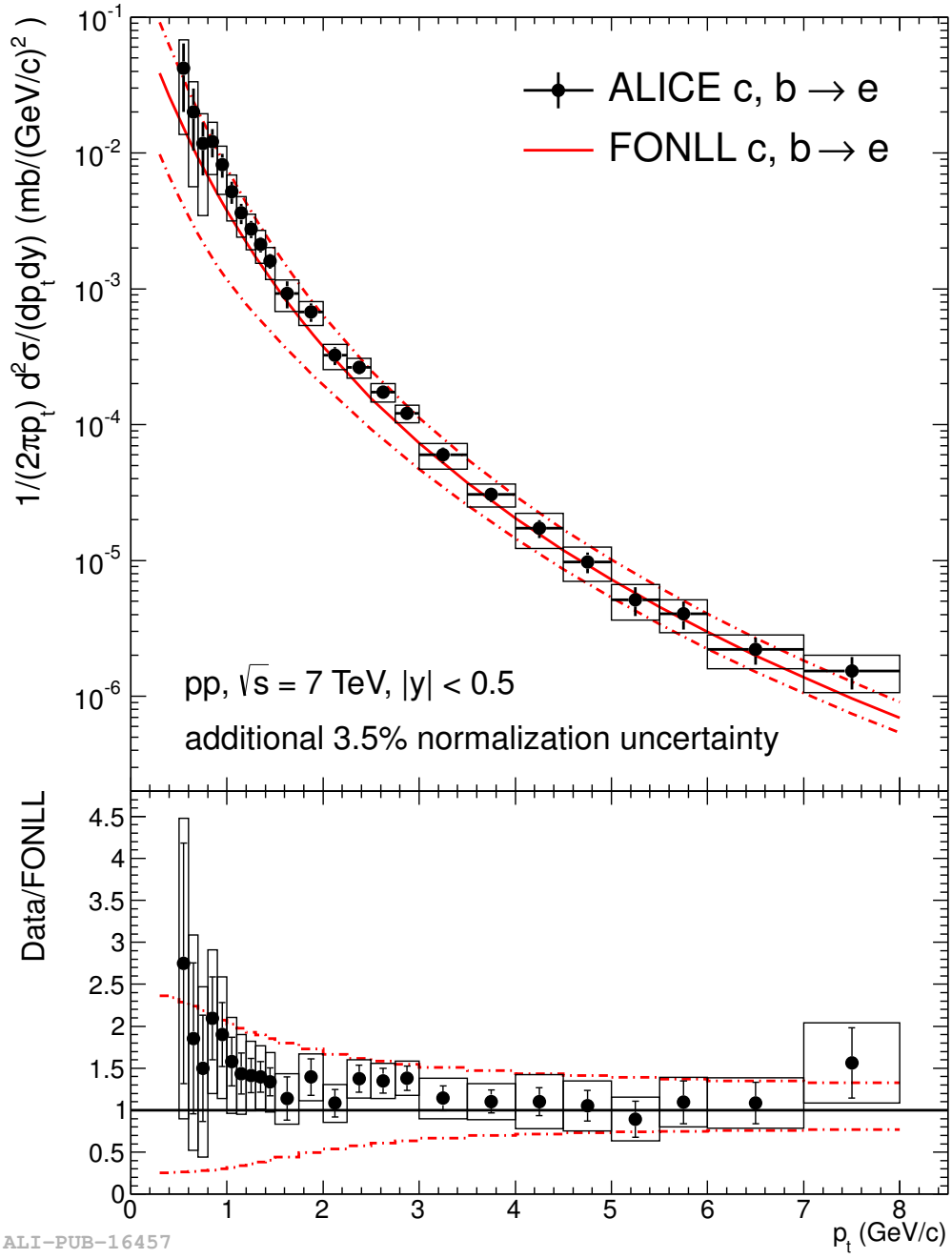

Figure 4.3: The measured electron spectrum from heavy-flavour hadron decays is compared to a FONLL calculation for inclusive charm and beauty hadron semileptonic decays on an absolute scale in the upper panel. The ratio of the measured spectrum to the FONLL pQCD calculation is shown in the lower panel. This plot is taken from [12].

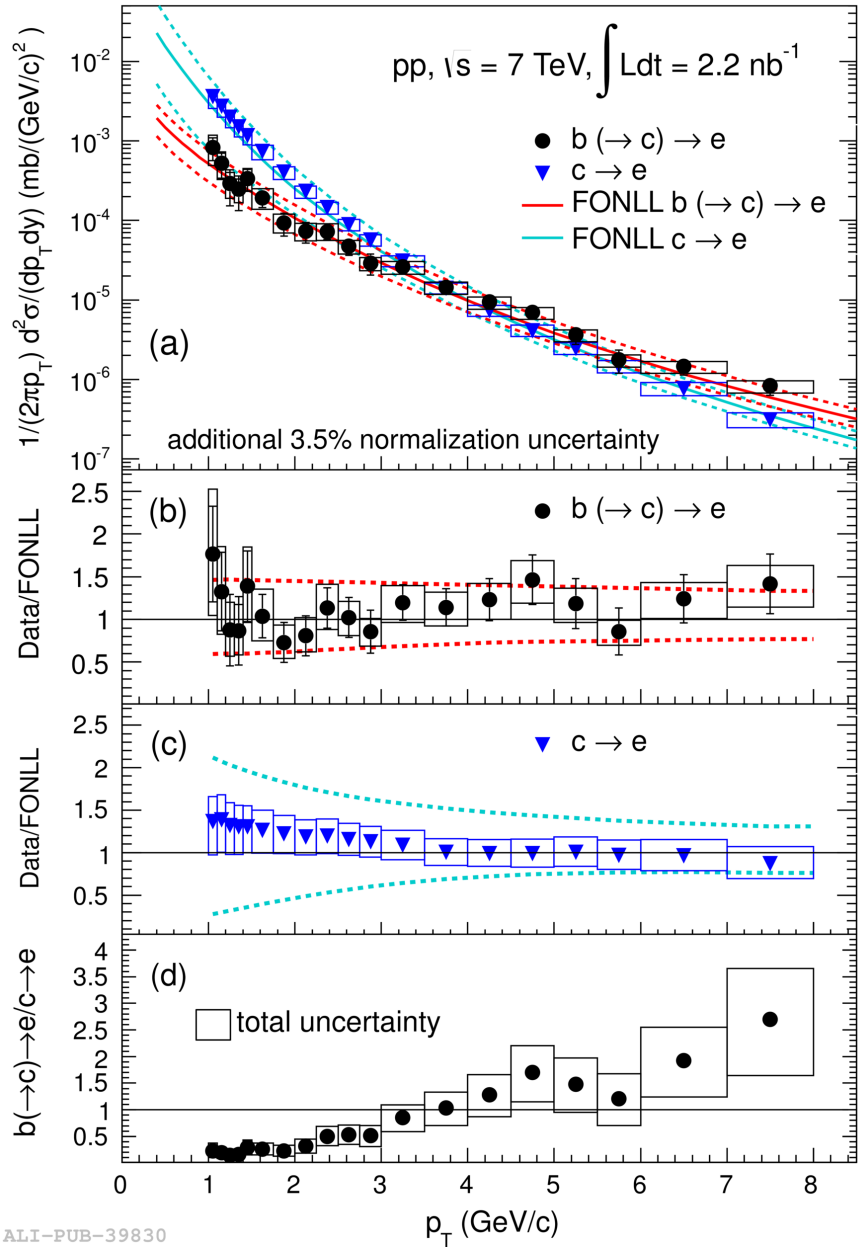

Figure 4.4: (a) p_{T}-differential invariant cross sections of electrons from beauty and from charm hadron decays. The error bars (boxes) represent the statistical (systematic) uncertainties. The solid (dashed) lines indicate the corresponding FONLL calculations (uncertainties) [2, 3]. Ratios of the data and the FONLL calculations are shown in (b) and (c) for electrons from beauty and charm hadron decays, respectively, where the dashed lines indicate the FONLL uncertainties. (d) Measured ratio of electrons from beauty and charm hadron decays with error boxes depicting the total uncertainty. This plot is taken from [25].

5. Ratios of production cross-sections at different collision energies

5.1. Measurements

Table 5.1: Published data used and the corresponding database links

Measurement	**Energy**	**Database link**
D mesons [6]	2.76 TeV	hepdata.cedar.ac.uk/view/ins1115187/short
D mesons [24]	7 TeV	hepdata.cedar.ac.uk/view/ins944757/short
$H_{b/c} \rightarrow e$ [13]	2.76 TeV	hepdata.cedar.ac.uk/view/ins1296860/short
$H_{b/c} \rightarrow e$ [12]	7 TeV	hepdata.cedar.ac.uk/view/ins1115824/short
$H_{b} \rightarrow e$ [8]	2.76 TeV	hepdata.cedar.ac.uk/view/ins1296861/short
$H_{b} \rightarrow e$ [25]	7 TeV	hepdata.cedar.ac.uk/view/ins1126962/short

The measured cross-section values corresponding to the ALICE publications, used in this thesis, are taken from the Durham database (Table 5.1). The data are given with a total and a statistical uncertainty per bin. Therefore, the systematic uncertainties were recalculated via quadratic subtraction of the statistical uncertainties on a bin per bin base:

$$\Delta_{\mathrm{syst,i}} = \sqrt{\Delta^2_{\mathrm{total,i}} - \Delta^2_{\mathrm{stat.,i}}} \tag{5.1}$$

The normalization uncertainties of the measurements at different energies are different because these are related to the minimum bias cross-section. Hence, these uncertainties were added again to the systematic uncertainties as shown in Equation 5.2.

$$\Delta_{\mathrm{syst,i}} = \sqrt{\Delta'^2_{\mathrm{syst,i}} + \Delta^2_{\mathrm{norm,i}}} \tag{5.2}$$

$$\Delta_{\mathrm{norm,i}} = \left(\frac{\mathrm{d}\sigma}{\mathrm{d}p_{\mathrm{T}}}\right)_{\mathrm{i}} \cdot \mathrm{f}_{\mathrm{norm.,i}} \tag{5.3}$$

The i denotes the respective p_{T}-bin and the normalisation uncertainties are calculated by multiplying the value of the differential cross-section in the corresponding bin with the values of the relative normalization uncertainty ($f_{\mathrm{norm.,i}}$) taken from the respective publication. As already discussed in chapter 4 the uncertainties on the branching ratios are not taken into account for the analysis of the ratios. For this analysis, the systematic and statistical uncertainties were treated separately.

5.2. Rebinning

The cross-sections have to be measured with equal binning in order to calculate the ratios. Therefore, the measurements at 7 TeV were rebinned to be in line with the measurement at 2.76 TeV. For the measurements of electrons from semi-electronic decay of heavy-flavour hadrons, two bins between 5 and 6 GeV/c were averaged. Since this production cross-section is normalized to the mean transverse momentum of each bin, the following formula has to be used to

$$c_{\mathrm{new}} = \frac{c_1 \cdot p_{\mathrm{T},1} + c_2 \cdot p_{\mathrm{T},2}}{p_{\mathrm{T},1} + p_{\mathrm{T},2}} \tag{5.4}$$

Here, c_1 and c_2 are the values of the cross-section in the first and the second bin, respectively, while $p_{\mathrm{T},1}$ and $p_{\mathrm{T},2}$ are the corresponding mean transverse momenta. For the D meson measurements, the bin contents of two bins in the following ranges were averaged in the usual way, 2-4 GeV/c, 4-6 GeV/c and 6-8 GeV/c. The statistical uncertainties of the different bins were added in quadrature and divided by the number of bins added up. Assuming that the systematic uncertainties in neighbouring bins are correlated, these were added linearly. For the D mesons, the following formulas were used

$$\Delta_{\mathrm{stat.,new\ bin}} = \frac{1}{2}\sqrt{\Delta^2_{\mathrm{stat.,bin1}} + \Delta^2_{\mathrm{stat.,bin2}}} \tag{5.5}$$

$$\Delta_{\mathrm{syst.,new\ bin}} = \frac{1}{2}(\Delta_{\mathrm{syst.,bin1}} + \Delta_{\mathrm{syst.,bin2}}), \tag{5.6}$$

while the electron uncertainties have to be recalculated taken the mean transverse momentum of the bins into account:

$$\Delta_{\text{stat.,new bin}} = \frac{\sqrt{(\Delta_{\text{stat.,bin1}} \cdot p_{\text{T},1})^2 + (\Delta_{\text{stat.,bin2}} \cdot p_{\text{T},2})^2}}{p_{\text{T},1} + p_{\text{T},2}} \tag{5.7}$$

$$\Delta_{\text{syst.,new bin}} = \frac{(\Delta_{\text{syst.,bin1}} \cdot p_{\text{T},1} + \Delta_{\text{syst.,bin2}} \cdot p_{\text{T},2})}{p_{\text{T},1} + p_{\text{T},2}} \tag{5.8}$$

5.3. Ratios

The ratios were calculated by dividing the measurements at 7 TeV by the ones at 2.76 TeV. The upper and lower uncertainties were determined according to the following equations, where R denotes the ratio:

$$\frac{\Delta \text{R}_{\text{up}}}{\text{R}} = \sqrt{\left(\frac{\Delta\sigma_{\text{7TeV,up}}}{\sigma_{\text{7TeV}}}\right)^2 + \left(\frac{\Delta\sigma_{\text{2.76TeV,down}}}{\sigma_{\text{2.76TeV}}}\right)^2} \tag{5.9}$$

$$\frac{\Delta \text{R}_{\text{down}}}{\text{R}} = \sqrt{\left(\frac{\Delta\sigma_{\text{7TeV,down}}}{\sigma_{\text{7TeV}}}\right)^2 + \left(\frac{\Delta\sigma_{\text{2.76TeV,up}}}{\sigma_{\text{2.76TeV}}}\right)^2} \tag{5.10}$$

The POWHEG and FONLL ratios were calculated for every variation separately because the theoretical parameters were assumed to be equal for the different energies. The variations with respect to the PDF error set were not performed with POWHEG because according to [15] the resulting uncertainties are subdominant in the kinematic region of interest. The total uncertainty band is calculated by adding the uncertainties introduced by the different types of variations in quadrature. To simplify the comparision with data, the FONLL and POWHEG ratios were rebinned to match the data binning. The POWHEG simulations for the measurements of the electrons from semi-electronic decays of beauty and charm hadrons were not evaluated because the comparison with the FONLL calculations already indicates that the measurements of the electrons from semi-electronic decays of beauty and charm hadrons have too large uncertainties.

5.4. Results

Figure 5.1 and Figure 5.2 show that both the statistical and systematic uncertainties of the data are much larger than the FONLL uncertainty bands and, therefore, nothing can be learned about the parameters. Most of the problems concerning the statistical uncertainty are connected to the low statistics available for the data at 2.76 TeV. Since the systematic uncertainty

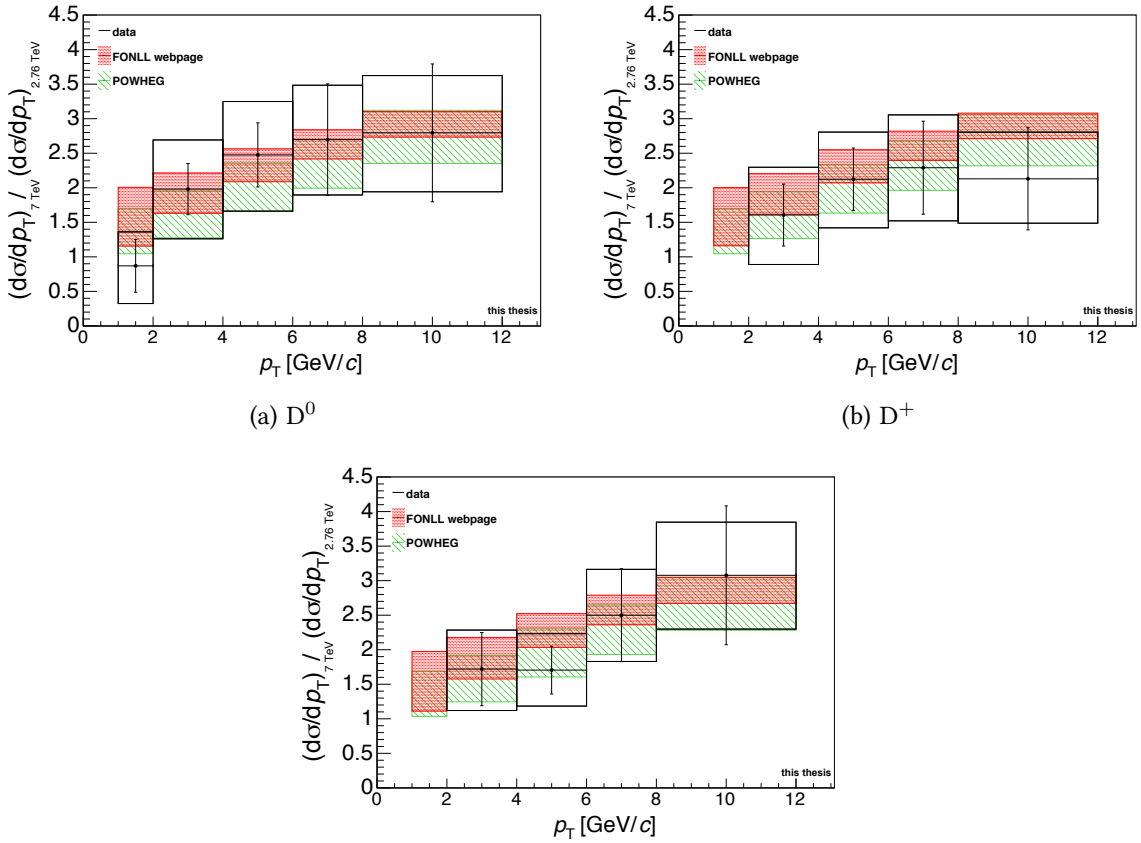

(a) D^0

(b) D^+

(c) D^{*+}

Figure 5.1: The ratio of p_T-differential cross-sections of D^0, D^+ and D^{*+} at $\sqrt{s} = 7$ TeV and 2.76 TeV measured with ALICE compared to POWHEG simulation (green) and FONLL (red).

are too large, too, the suggestion cannot only be to take more data to reduce the statistical uncertainties, the analysis techniques have to evolve to reduce the systematic uncertainties as well.

The FONLL bandwidth was used to estimate the maximum uncertainty allowed to be able to reject a specific setting of FONLL parameter at a 3σ-level to estimate how much the uncertainties have to be reduced. When re-analysing with improved methods, the position of the ratio points will probably change. Therefore, two different cases were analysed.

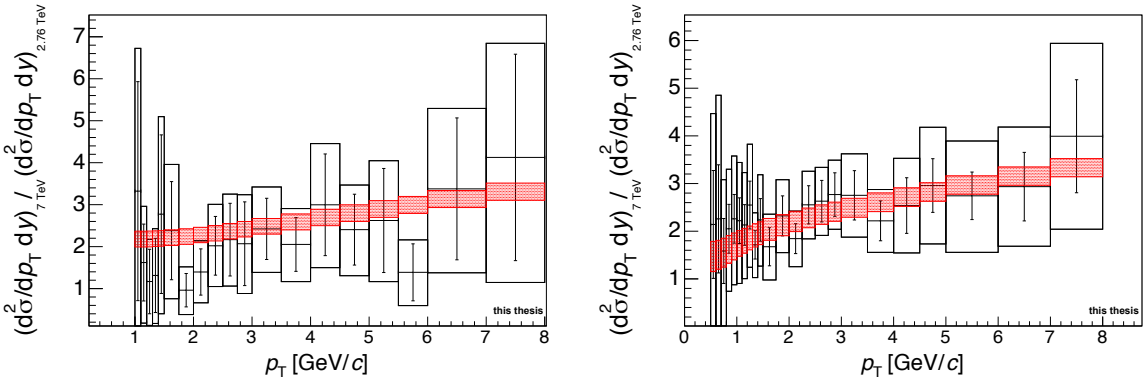

(a) $H_b \to e$ (b) $H_{b/c} \to e$

Figure 5.2: The ratio of p_T-differential cross-sections of electrons from semi-electronic decays of beauty and charm hadrons at $\sqrt{s} = 7$ TeV and 2.76 TeV measured with ALICE compared to FONLL (red boxes).

In the first case, the maximum allowed uncertainties were calculated using the distance between the extreme and the central values of the FONLL band.

$$\Delta R_{\text{data, upper}} = \frac{1}{3}(R_{\text{FONLL, max}} - R_{\text{FONLL, central}}) \tag{5.11}$$

$$\Delta R_{\text{data, lower}} = \frac{1}{3}(R_{\text{FONLL, central}} - R_{\text{FONLL, min}}) \tag{5.12}$$

The resulting mocked-up data for the D mesons can be seen in Figure 5.3 and Figure 5.4. For the second case, the assumption that the data points lie at the upper or lower edge of the FONLL band was used. The maximum total uncertainty on the data ratio allowed would be $\frac{1}{3}$ times the distance of the lowest and the highest FONLL values for this scenario.

$$\Delta R_{\text{data, max}} = \frac{1}{3}(R_{\text{FONLL, max}} - R_{\text{FONLL, min}}) \tag{5.13}$$

The plots showing the mocked-up data sets for electrons from semi-electronic decays of beauty and charm hadrons can be found in the appendix, Figure A.6 and Figure A.7. The uncertainty estimates were performed in five different p_T-bins, see Table 5.2, which summarizes the maximum uncertainties on the ratio of cross-section measurements at $\sqrt{s} = 7$ TeV and 2.76 TeV allowed in order to be able to disfavour some parameter values.

Table 5.2: Maximum allowed total uncertainty on the single measurement of heavy-flavour cross-sections determined using the ratio of FONLL calculations at $\sqrt{s} = 7\,\text{TeV}$ and 2.76 TeV assuming the relative uncertainties is the same for both energies.

p_{T}-bin [GeV/c]	$\mathbf{D^0}$	$\mathbf{D^+}$	$\mathbf{D^{*+}}$	$\mathbf{H_b \to e}$	$\mathbf{H_c \to e}$
Data at the upper edge of the FONLL band					
$0-1$	9.0%	9.0%	8.9%	3.6%	8.2%
$1-2.5$	9.1%	9.0%	9.4%	3.5%	5.0%
$2.5-4$	5.7%	5.8%	6.0%	3.2%	3.6%
$4-6$	4.3%	4.3%	4.5%	3.0%	2.8%
$6-25$	2.3%	2.3%	2.3%	2.1%	1.7%
Data at the lower edge of the FONLL band					
$0-1$	14.7%	14.7%	14.4%	4.2%	12.5%
$1-2.5$	14.8%	14.7%	15.7%	4.1%	6.3%
$2.5-4$	7.6%	7.7%	8.1%	3.7%	4.2%
$4-6$	5.2%	5.3%	5.5%	3.5%	3.2%
$6-25$	2.5%	2.5%	2.6%	2.2%	1.9%
Data at the centre of the FONLL band					
$0-1$	$^{+4.0\%}_{-6.6\%}$	$^{+3.9\%}_{-6.7\%}$	$^{+4.1\%}_{-6.4\%}$	$^{+1.5\%}_{-2.4\%}$	$^{+2.1\%}_{-6.8\%}$
$1-2.5$	$^{+2.9\%}_{-7.3\%}$	$^{+2.9\%}_{-7.2\%}$	$^{+3.0\%}_{-7.6\%}$	$^{+1.4\%}_{-2.3\%}$	$^{+2.0\%}_{-3.4\%}$
$2.5-4$	$^{+2.2\%}_{-4.0\%}$	$^{+2.3\%}_{-4.1\%}$	$^{+2.3\%}_{-4.3\%}$	$^{+1.3\%}_{-2.0\%}$	$^{+1.7\%}_{-2.2\%}$
$4-6$	$^{+1.8\%}_{-2.8\%}$	$^{+1.8\%}_{-2.8\%}$	$^{+1.9\%}_{-2.9\%}$	$^{+1.3\%}_{-1.9\%}$	$^{+1.4\%}_{-1.6\%}$
$6-25$	$^{+1.1\%}_{-1.3\%}$	$^{+1.1\%}_{-1.3\%}$	$^{+1.1\%}_{-1.3\%}$	$^{+1.0\%}_{-1.1\%}$	$^{+1.0\%}_{-0.8\%}$

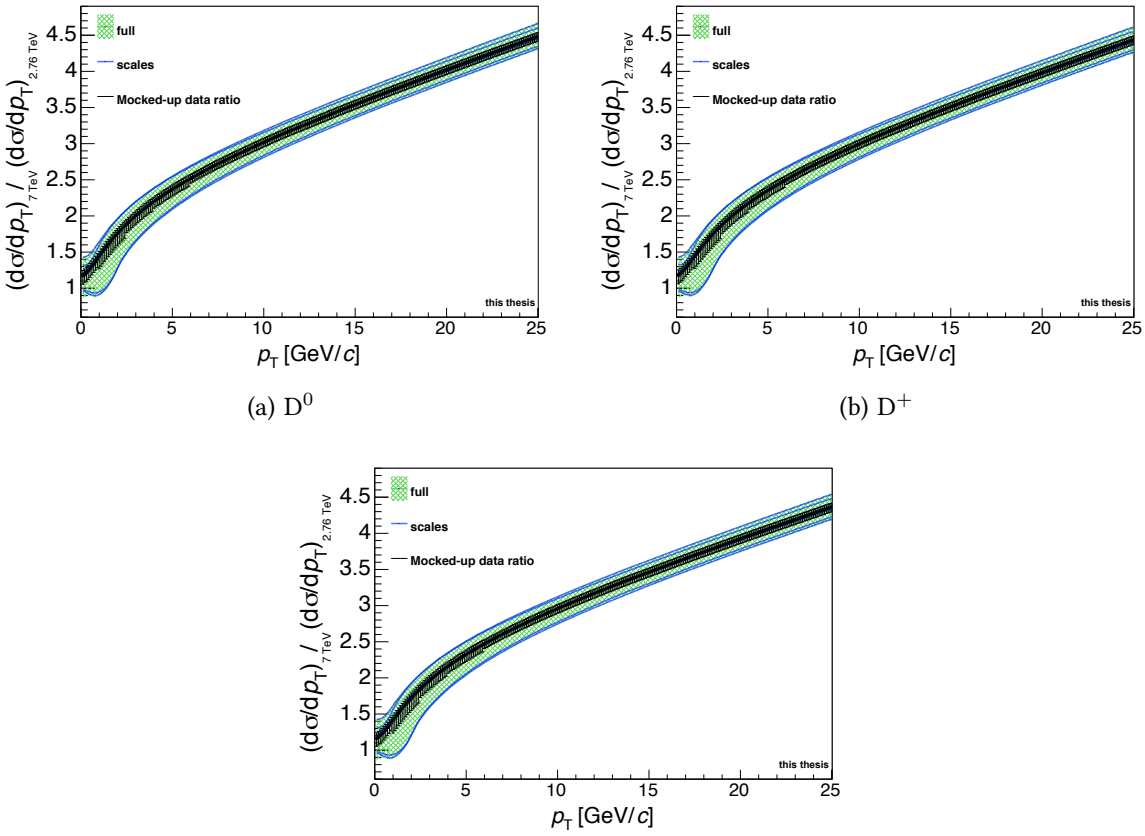

(a) D^0

(b) D^+

(c) D^{*+}

Figure 5.3: The ratio of p_T-differential cross-sections of D^0, D^+ and D^{*+} at $\sqrt{s} = 7\,\text{TeV}$ and 2.76 TeV evaluated using FONLL. Here the mocked-up data is assumed to lie at the centre of the FONLL reference, which leads to rather small asymmetric uncertainties allowed to be still decisive.

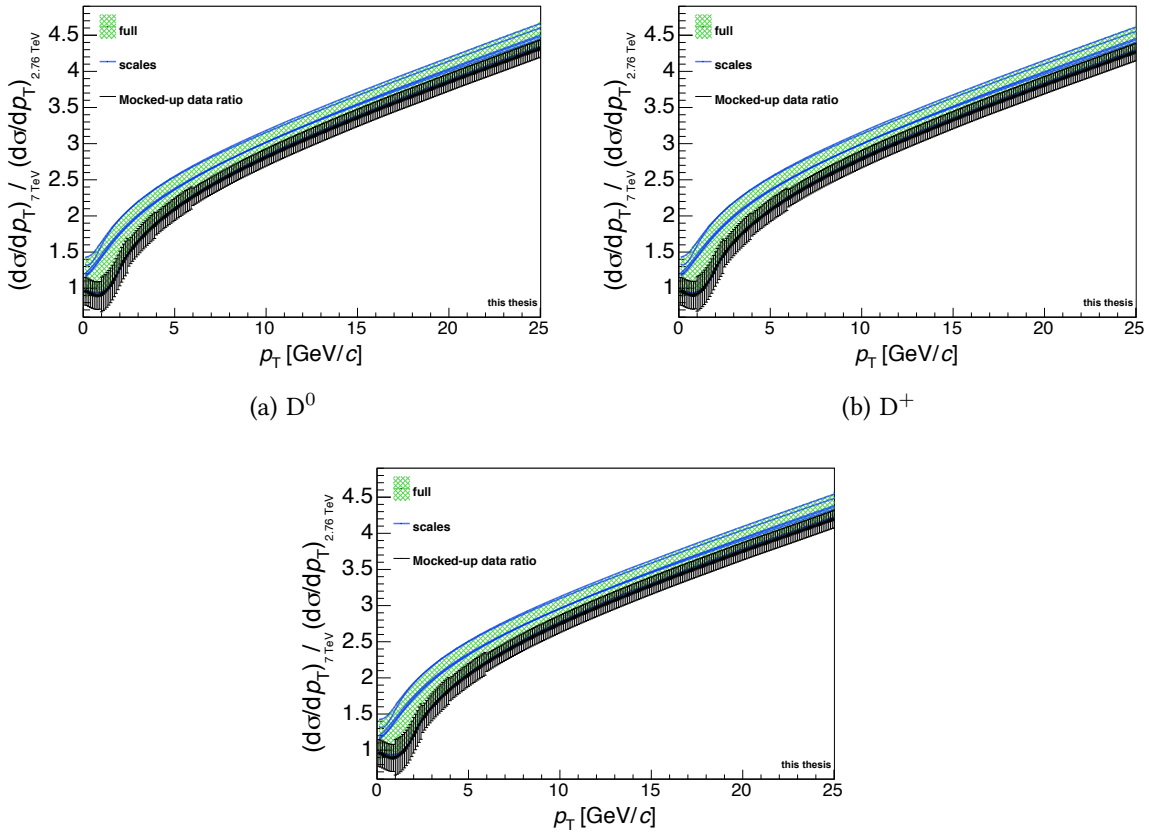

(a) D^0

(b) D^+

(c) D^{*+}

Figure 5.4: The ratio of p_T-differential cross-sections of D^0, D^+ and D^{*+} at $\sqrt{s} = 7$ TeV and 2.76 TeV evaluated using FONLL. Here the mocked-up data is assumed to lie at the lower edge of the FONLL reference, which leads to a little bit larger uncertainties allowed to be still decisive compared to the first case.

6. Electrons from heavy-flavour hadron decays in pp collisions at $\sqrt{s} = 2.76\,\mathrm{TeV}$

In the previous chapter, we learned that we have to improve the precision of our measurements to constrain the parameters of the theory and, hereby, learn more about the production processes. Since the signal-to-background ratio in the measurements of electrons from heavy-flavour hadron decays is very low at low transverse momenta, the systematic uncertainty is dominated by the contribution from the background subtraction in this kinematic region. In the published analysis [13], the electron background was subtracted using the cocktail-subtraction method. The cocktail of electrons from the various background sources is calculated from the measured spectra of these sources using a Monte-Carlo hadron-decay generator. It contains electron distributions from the following sources:

- Dalitz-decays of light neutral mesons (π^0, η and η')
- conversion of decay photons
- dielectron decays of light vector mesons (ρ, ω and ϕ)
- dielectron decays of heavy quarkonia (J/ψ and Υ)
- weak K $\rightarrow e\pi\nu$ (K_{e3}) decays
- partonic hard scattering processes, like Drell-Yan processes and prompt real and virtual photons

The dominating sources of background electrons are the Dalitz-decays of light neutral mesons and the photon conversions, while the hard scattering processes get important towards high p_{T}, too. A detailed description of the cocktail and its ingredients can be found in Figure 4.3.

To avoid large systematic uncertainties affected by the use of the background cocktail, another analysis method was applied, which does not use a background cocktail to reject the electrons from the dominating sources. This method, called photonic method in this thesis, exploits the fact that these processes create electron-positron pairs which can be identified in data directly via their low invariant mass. The electron candidate tracks belonging to such pairs are excluded from the analysis.

Figure 6.1 shows the comparison of the spectra of electrons from heavy-flavour hadron decays obtained via cocktail-subtraction and the photonic method measured in p–Pb collisions at $\sqrt{s_{\text{NN}}} = 5.02\,\text{TeV}$ [30]. The spectra are compatible within uncertainties but the result using the photonic method has much smaller systematic uncertainties especially in the low p_{T}-region.

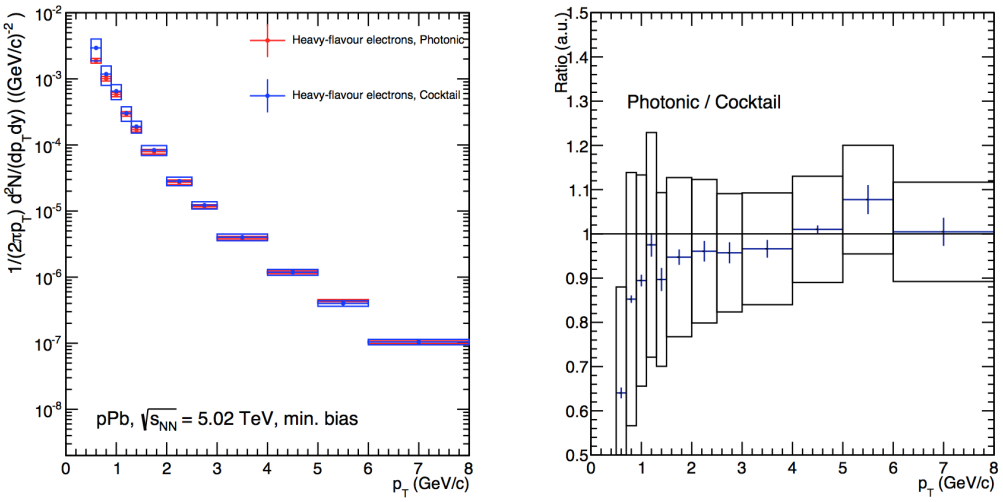

Figure 6.1: Comparison of the heavy-flavour electron p_{T}-spectrum obtained via the cocktail-subtraction method and photonic method for p–Pb collisions at $\sqrt{s_{\text{NN}}} = 5.02\,\text{TeV}$. The left panel shows the respective p_{T}-spectra and the right panel the ratio of both [30].

Therefore, the data collected in pp collisions at $\sqrt{s} = 2.76\,\text{TeV}$ were re-analysed using the photonic method. The resulting production cross-section of electrons from semi-electron decays of charm and beauty hadrons can be also used as an improved reference spectrum for the Pb–Pb collisions [31].

6.1. Data set and Monte Carlo simulations

For this analysis, the minimum bias data sample taken in pp collisions at $\sqrt{s} = 2.76\,\text{TeV}$ in spring 2011, the LHC11a period, was used. The minimum bias trigger requires at least one hit in the SPD or in either of the two V0 arrays, which has to coincide with the signal from the beam position monitors. During this data taking period, the Silicon Drift Detector (SDD) layers were not read out for a sizeable fraction of events because these detectors are slower than the other silicon detector types and the data taking period was very short. Correspondingly, there are two versions of reconstructed data for this period, one with the SDD information and another one without it. The latter sample offers higher statistics because all events are included, also those with SDD available but its information is not used in the reconstruction procedure.
The analysis presented in this thesis is based on the second reconstruction pass (pass 2) of the data sample without SDD and was performed on Event Summary Data (ESD). The ESD contains lists of global event properties, e.g. the information about the triggers, and reconstructed tracks or particles including their associated detector hits and calorimetric clusters. The data sample without SDD was only used for cross-checks.
Two additional reconstruction passes are available which could not be used to perform this analysis. The description of the expected signals in the TPC for the various particle types, called TPC splines, were fitted to raw data without correction for the η-flattening in pass 3 which oppose the use of this data sample. For Pass 4, no Monte Carlo (MC) simulation with enhancement of electrons from heavy-flavour existed. In addition, the statistics of the minimum bias MC for both of these reconstruction passes is low. Since the Time of Flight detector (TOF) was used for particle identification (PID), the data selection was reduced to eight runs in which the performance of the TOF detector is considered good. In total about 43.8M events were analysed, which correspond to an integrated luminosity $L_{\text{int}} \approx 0.8\,\text{nb}^{-1}$.

Two different Monte Carlo (MC) samples were used for this analysis. The minimum bias Monte Carlo sample (LHC12e6) was produced using the PYTHIA generator [21, 22] and the Geant 3 transport code [29]. For the other sample (LHC12a9), a special PYTHIA MC simulation was used in which a trigger on charm and beauty hadrons decaying semi-electronically was employed. In addition, another enhanced PYTHIA MC simulation (LHC11b10b) was used for cross-checks. For this MC sample, the trigger included events with π^0, η, J/ψ and B $\rightarrow$ J/ψ, too. To perform a MC closure test, which should proof the applicability of the photonic method, two additional minimum bias MC samples (LHC12f1a, LHC12f1b) were

used. These MC samples were generated using the PYTHIA [21, 22] and the PHOJET [32, 33] generator for LHC12f1a and LHC12f1b, respectively.

Table 6.1: Summary of the data sample and Monte Carlo simulations used in this analysis

Period / Sample	Number of events	additional information
Data		
LHC11a	43.8 M	pp, $\sqrt{s} = 2.76$ TeV, minimum bias, 8 runs, reconstruction pass 2
Monte Carlo simulations		
LHC12e6	32.1 M	PYTHIA, minimum bias
LHC12a9	2.29 M	PYTHIA, enhanced (trigger on events with $b\bar{b}$ or $c\bar{c}$ production
LHC11b10b	2.69 M	PYTHIA, enhanced (trigger on events with π^0, η, J/ψ and B $\rightarrow$ J/ψ and $b\bar{b}$ or $c\bar{c}$ production
LHC12f1a	12.6 M	PYTHIA [21, 22], minimum bias, reconstruction pass 4
LHC12f1b	10.7 M	PHOJET [32, 33], minimum bias, reconstruction pass 4

6.2. Event selection

The primary collision vertex can be reconstructed using reconstructed tracks in the event or correlated hits in the two Silicon Pixel Detector (SPD) layers. For this analysis, only events which provide a vertex from reconstructed tracks were used, which are about 80.5% of all the events in the data sample. Edge effects from being at the limit of the central barrel acceptance were minimised by requiring that the primary vertex is within ±10 cm around the nominal centre of the experiment along the beam direction. Pile-up events were identified and rejected using the SPD as in former analyses [12, 13]. About 72% of the events in the data sample fulfil these event selection criteria.

The analysis was performed using the same binning as for the Pb–Pb measurement [31] to improve the statistics in each bin and to be able to calculate the nuclear modification factor R_{AA}. For the R_{AA}, the measured invariant yield in Pb–Pb collisions is compared to the respective result in pp collisions scaled with the average number of binary nucleon-nucleon collisions for the respective centrality class. The R_{AA} is used to to quantify the energy loss in

the Quark-Gluon-Plasma and to learn more about its physical properties by comparing with different theoretical models.

Therefore, neighbouring bins above $p_{\mathrm{T}} = 1.5\,\mathrm{GeV}/c$ were merged at the beginning of the analysis. The bins below $p_{\mathrm{T}} = 1.5\,\mathrm{GeV}/c$ were not merged before the correction steps because the efficiencies used in this analysis have a steep rise in this region and merging bins there would reduce the precision of the final result.

6.3. Track selection

In the magnetic field ($B = 0.5\,\mathrm{T}$) provided by the solenoid magnet, the minimum p_{T} of particles needed to reach the TOF detector is about $0.3\,\mathrm{GeV}/c$. However, the spectra shown in this chapter start at a minimum transverse momentum of $0.5\,\mathrm{GeV}/c$ because of the low signal-to-background ratio and the low and steep efficiencies of finding the electrons from photonic sources, the track selection and the particle identification below $0.5\,\mathrm{GeV}/c$, which makes the analysis very difficult and would lead to large statistical uncertainties. The analysis was performed using tracks inside the pseudorapidity range $|\eta| < 0.8$, which is close to the maximum acceptance of the detectors.
Since electrons from photonic background sources are produced in electron-positron pairs, two categories of analysis tracks were used. The electron candidates fulfil similar selection criteria as the ones used in the former analysis [13]. The associated tracks were used to build up the aforementioned pairs and have to satisfy looser track selection criteria to increase the efficiency of finding the electron-position pairs, see Table 6.2.

- Fake tracks which comprise a significant number of TPC clusters originating from more than one charged particle trajectory were rejected by requiring that the χ^2 per degree of freedom (ndf) of the momentum fit in the TPC is smaller than four.

- The track quality in the TPC is characterised by the number of clusters used for the reconstruction and re-fit of the track. Not all clusters used for tracking are used for the energy loss calculation, e.g. clusters close to the border of TPC sectors are not considered. Only tracks for which at least 110 (out of a maximum of 159) clusters were used for the tracking and at least 80 for the energy loss calculation were accepted in this analysis. The requirement on the number of TPC clusters is used to improve the discrimination of electrons and pion because electron tracks have, on average, a higher number of clusters. This is true due the fact that the energy deposition of electrons

Table 6.2: Summary of the track selection imposed on the electron candidates and the associated tracks

Type	**Electron candidates**	**Associated tracks**
$p_{\mathrm{T}}^{\mathrm{min}}$	$0.5\,\mathrm{GeV}/c$	$0.1\,\mathrm{GeV}/c$
η	0.8	0.8
ITS and TPC refit	required	required
χ^2/ TPC clusters	< 4	< 4
Number of TPC clusters	$\geq$110	$\geq$60
Number of TPC $\frac{\mathrm{d}E}{\mathrm{d}x}$ clusters (PID)	$\geq$80	$\geq$60
Ratio found / findable TPC clusters	> 0.6	> 0.6
Number of ITS hits	$\geq$3	$\geq$2
Requirements of SPD layes	both	any
Distance of closest approach to the primary vertex in xy	< 1 cm	< 1 cm
Distance of closest approach to the primary vertex in z	< 2 cm	< 2 cm
Kink mothers	excluded	excluded
TOF t − TOF $t\vert_{el}$	$\pm 3\,\sigma$	not used
TPC $\frac{\mathrm{d}E}{\mathrm{d}x} - \left\langle \text{TPC } \frac{\mathrm{d}E}{\mathrm{d}x} \right\rangle\vert_{el}$	$^{+3.2}_{-1.0}\,\sigma$	$\pm 3\,\sigma$

on the Fermi plateau is approximately 1.6 times larger than for minimum ionizing particles.

- In addition to the restriction on the minimal number of ITS hits, hits in both SPD layers were required to minimise the contribution from electrons from photon conversions in the ITS.

- To reject background tracks and non-primary tracks, the maximal distance of closest approach (DCA) of the tracks to the primary vertex was restricted to 1 cm in radial direction and 2 cm along the beam direction.

- Tracks which were identified as kink mothers or daughters were rejected from the analysis. Kinks are particle tracks which at some point change direction very rapidly, e.g. pions which decay into muons and neutrinos or electrons which suffer from bremsstrahlung. The track before the change of direction is stored as kink mother and the track afterwards is called kink daughter.

For the analysis described in this thesis the Time Projection Chamber (TPC) and the Time of Flight (TOF) detector were used to identify the electrons. In the p_{T}-region up to about $2\,\mathrm{GeV}/c$, the information from TOF is essential to remove the contamination from hadrons, like pions, kaons and protons, as shown in panel (a) of Figure 6.2.

- The electron selection starts by rejecting all particle tracks outside $\pm 3\,\sigma$ around the expected time-of-flight for electrons which removes hadrons from the electron candidate sample. Since this selection removes kaons, proton and deuterons in the p_{T}-region where their lines cross the electron line in the TPC, a further refinement of the selection can be reached by introducing a rejection of tracks based on the deviation from the expected $\frac{\mathrm{d}E}{\mathrm{d}x}$ for electrons in the TPC, see panel (b) of Figure 6.2.

- During the data recording period used in this analysis the TPC was operated at a high gain which improves the energy loss resolution compared to the data set taken at 7 TeV [12]. As a consequence, the electron-pion separation is improved and tracks within $-1.0\,\sigma$ and $3.2\,\sigma$ instead of $0\,\sigma$ and $3\,\sigma$ can be selected. The upper edge of this selection was changed to $3.2\,\sigma$ to select more electron candidate tracks.

- As in the former analyses [12, 13], the average spectrum of positrons and electrons were determined.

6.4. Determination of the remaining hadron contamination

After these cuts there was still some hadron contamination which had to be subtracted statistically. This was done by assigning to each track (of a given momentum p and transverse momentum p_{T}) a weight which describes the probability of the track to be a hadron. This weight is given by a function obtained by fitting the electron component and the different hadron components of the TPC $\frac{\mathrm{d}E}{\mathrm{d}x}$-distribution in various p-slices with a width of $0.4\,\mathrm{GeV}/c$.

The TPC signal corresponds to several measurement of the energy loss of the particle in an effective track length and, therefore, should follow the Landau distribution of series measurements. To remove the large Landau-tail of the TPC signal distribution, a truncated mean requirement is used which modifies the distribution. This modification can be described by a exponential correction function. In addition, the resulting modified Landau has to be convoluted with a Gaussian to take detector effects into account. More detailed description of

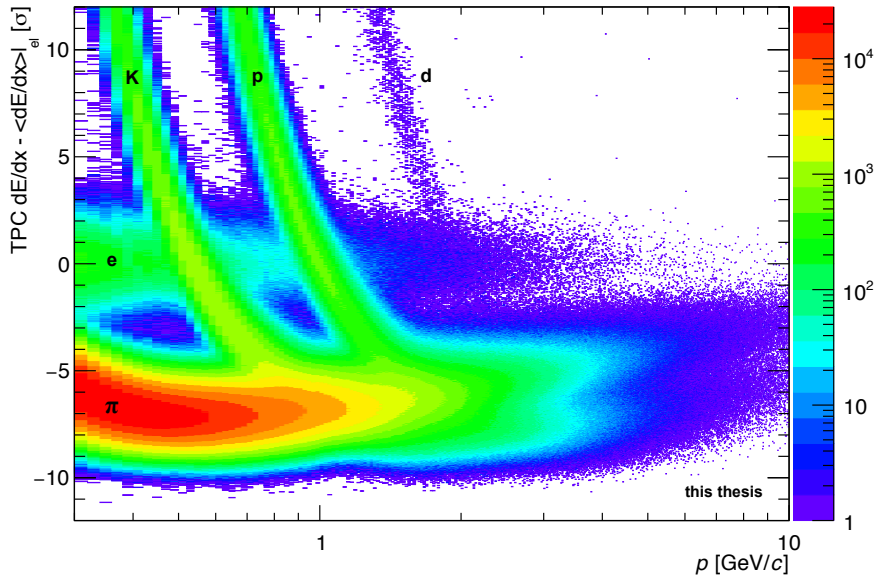

(a) TPC $\frac{\mathrm{d}E}{\mathrm{d}x}$ before TOF selection

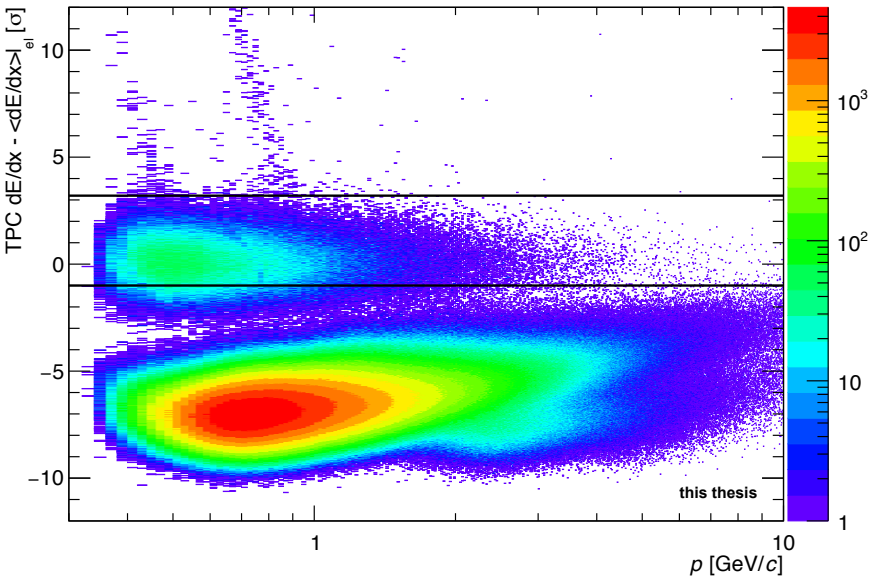

(b) TPC $\frac{\mathrm{d}E}{\mathrm{d}x}$ after TOF selection

Figure 6.2: The TPC $\frac{\mathrm{d}E}{\mathrm{d}x}$ as a function of the momentum before [panel (a)] and after [panel (b)] applying the selection with TOF. In panel (a) the contributions from kaons (K), protons (p), deuterons(d), pions (π) and electrons are indicated by the respective symbol. The TPC PID selection is shown as the black lines in panel (b) and all tracks inside this band are used for the further analysis steps.

the parametrisation of the TPC signal can be found in [34, 12].
The pion and electron $\frac{\mathrm{d}E}{\mathrm{d}x}$-distributions were described by the combination of Landau, exponential and Gaussian function. At low momenta the protons and kaons are suppressed by the TOF selection, while at higher momenta the kaon and proton $\frac{\mathrm{d}E}{\mathrm{d}x}$-lines approach each other [12]. Therefore, a template which was extracted from data was used to fit the kaon and proton $\frac{\mathrm{d}E}{\mathrm{d}x}$-distributions simultaneously. Figure 6.3 shows the distribution of the TPC $\frac{\mathrm{d}E}{\mathrm{d}x}$-signals in the momentum slices between 2.0 GeV/c and 2.4 GeV/c with simultaneous fit of electron (red), pion (green) and kaon (grey) distributions as well as the difference (magenta) and the ratio (blue) of the data to these fits.

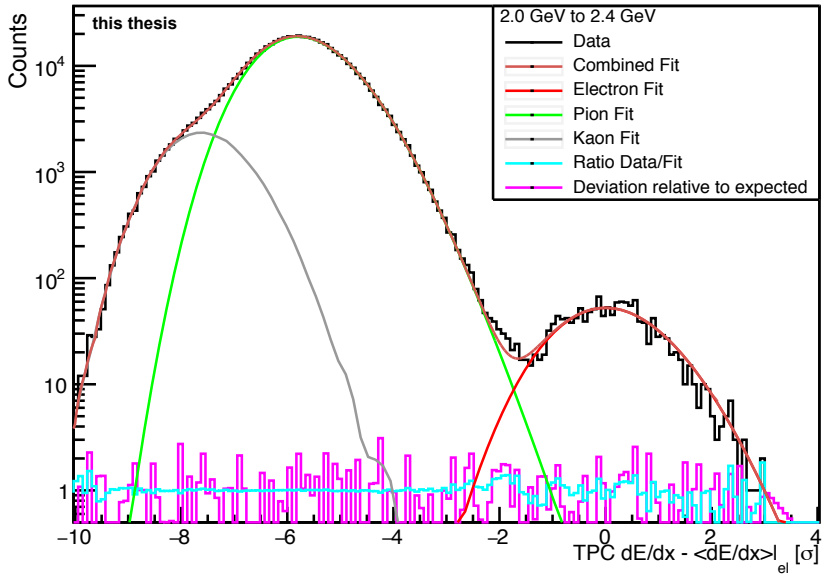

Figure 6.3: The distribution of the TPC $\frac{\mathrm{d}E}{\mathrm{d}x}$ signals in the momentum slices between 2.0 GeV/c and 2.4 GeV/c with simultaneous fit of electron (red), pion (green) and kaon (grey) distributions. In addition, the ratio (blue) between data and fit as well as the deviation (magenta) of the fit relative to the data is shown.

The hadron contamination in each of these slices was evaluated in the following way:

$$\text{Fraction of contamination} = \frac{\int_{x_{\min}}^{x_{\max}} (f_\pi(x) + f_\mathrm{K}(x))\mathrm{d}x}{\int_{x_{\min}}^{x_{\max}} (f_\pi(x) + f_\mathrm{K}(x) + f_\mathrm{el}(x))\mathrm{d}x}, \tag{6.1}$$

where $x_{\min} = -1.0$ and $x_{\max} = 3.2$ are the TPC PID cuts and $f_i(x)$ are the fit functions for the respective particle type i. Figure 6.4 shows the fraction of hadrons as a function of the momentum in linear (left) and logarithmic (right) scale. It was parametrised using different functional forms.

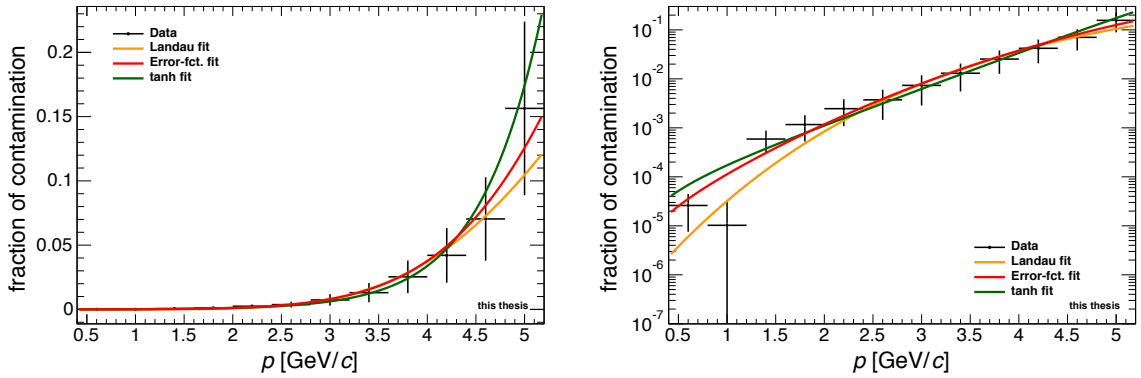

Figure 6.4: The fraction of hadron selected with the PID requirements on the TOF and a selection of tracks with a deviation from the expected energy loss for electrons in the TPC in between -1.0 σ and 3.2 σ.

The hyperbolic tangent does not describe the contamination at low momenta very well and its rise at high momenta seems to be too steep and overestimates the contamination above 4.0 GeV/c. Therefore, it was not used in the further analysis.
The Error function

$$f(p) = 0.499952 + 0.499960 \cdot \text{Erf}(0.446\,076\,(\text{GeV}/c)^{-1} \cdot p - 3.04141) \tag{6.2}$$

describes the hadron contamination best. The Landau function shown was used to evaluate the systematic uncertainty.

The effect of subtracting the hadron contamination from the inclusive electron yield as a function of p_{T} is shown in Figure 6.5. The hadron contamination begins to be important above $p_{\text{T}} = 3\,\text{GeV}/c$ and reaches up to 17% of the yield at 5 GeV/c. At low and intermediate p_{T} the hadron contamination accounts for less than 1% of the inclusive electron yield.
After all these selection steps and the removal of the hadron contamination, we obtained a raw inclusive electron spectrum as a function of transverse momentum.

6.5. Spectrum of electrons from photonic sources

The raw inclusive electron spectrum still contains electrons from various sources. As mentioned before, the most important source of electron background are the Dalitz-decays of light neutral mesons and the photon conversions. Since the resulting electrons are created in pairs of unlike charge sign coming from the decay or conversion of a relatively light par-

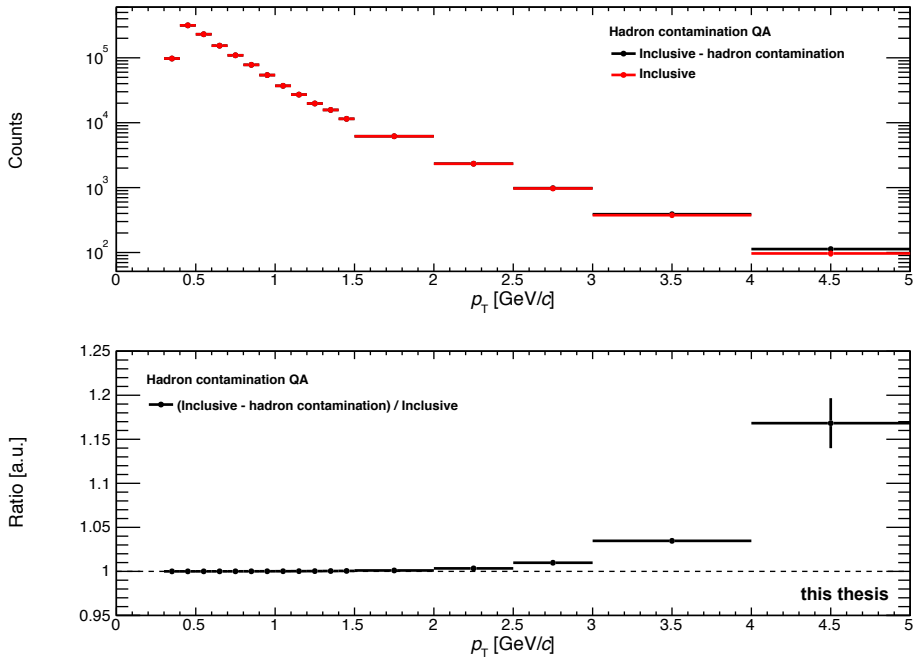

Figure 6.5: The raw yield of inclusive electrons as a function of transverse momentum with (black) and without (red) hadron contamination subtraction.

ticles, they can be identified by reconstructing low mass unlike sign pairs.
The electron candidate tracks, which fulfil the strict track selection, were paired with the associated tracks which have the opposite charge to build up a pool of unlike sign pairs. This pool contains pairs from the sources mentioned above and combinatorial background. The combinatorial background was estimated from like sign pairs which were build up by pairing electron candidates and associated tracks with the same charge. In each p_T-bin of the inclusive electron spectrum, the yield of electrons from photonic sources was evaluated using

$$N_{\text{photonic}} = \frac{N_{\text{ULS}} - N_{\text{LS}}}{\epsilon_{\text{tagging}}} \tag{6.3}$$

$$\text{with } \epsilon_{\text{tagging}} = \frac{N_{\text{found}}}{N_{\text{photonic}}} \tag{6.4}$$

where N_{ULS} and N_{LS} are the amount of unlike and like sign pairs with a invariant mass smaller than the requirement on the pair mass, respectively. In this analysis, the invariant mass was restricted to values below the mass of the π^0 ($0.14\,\text{GeV}/c^2$), see Figure 6.6.

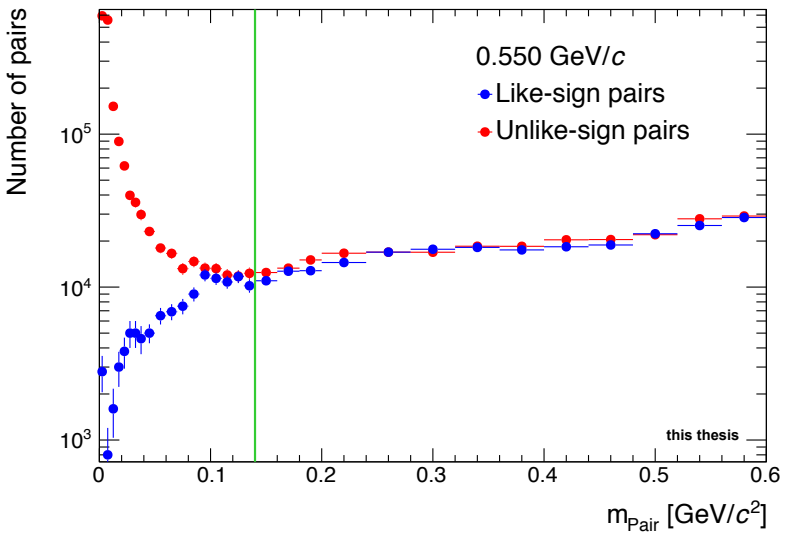

Figure 6.6: The distributions of the unlike and like sign pairs in the p_T-bin of the inclusive electron spectrum between $0.5\,\text{GeV}/c$ and $0.6\,\text{GeV}/c$ as a function of invariant pair mass. The maximal mass of the pair used in this analysis is indicated by a green line.

The tagging efficiency $\epsilon_{\text{tagging}}$ quantifies the probability that a photonic electron in a given p_T-bin is measured. It was calculated in the minimum bias MC sample (LHC12e6) by calculating the ratio of photonic electrons for which the partner is found in the pool of associated tracks (N_{found}) divided by all electrons from photonic sources (N_{photonic}) as a function of the transverse momentum of the electron candidate ($p_{T,\,\text{inc}}$). Figure 6.7 shows the tagging efficiency as a function of transverse momentum of the electron candidate evaluated using the knowledge from MC truth (red) or by determining the number of found electrons by subtraction of the number of unlike sign pairs from the number of like sign pairs (blue). In this analysis the tagging efficiency evaluated using the information from MC truth was used.

Since the tagging efficiency depends on the p_T-shape of mother particles and the p_T-shape of the π^0 spectrum in MC differs from the measured one, the MC distribution had to be reweighed. The weighting factors were calculated as the ratio of the measured [35] and the simulated π^0 transverse momentum distributions. The spectra of the other light mesons (η, ρ, ω, η' and ϕ) in the simulation were re-weighted to distributions obtained via m_T-scaling [36] of the π^0 p_T-spectrum. More detailed information about this procedure can be found in [37].

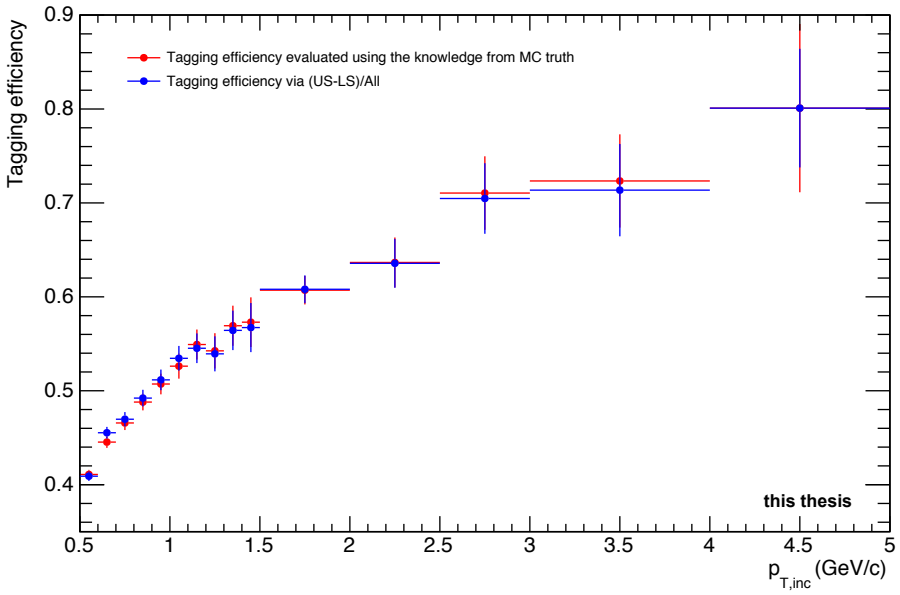

Figure 6.7: The tagging efficiency as a function of transverse momentum of the electron candidate evaluated using the knowledge from MC truth (red) or with selecting the detected electrons in a similar way as for data (blue).

The raw yield of "non-photonic" electrons is obtained by subtracting the raw yield of "photonic" electrons from the inclusive yield. Figure 6.8 summarizes all the ingredients needed to calculate the raw yield of electrons from non-photonic sources (shown in blue). The afore mentioned hadron contamination is shown in green. The slight rise below $p = 1.2\,\mathrm{GeV}/c$ is an artefact from multiplying the Error function with a very large number of inclusive electron candidates. It has no specific physical meaning and does not change the spectrum of electrons from non-photonic sources very much. The spectrum of electrons from photonic sources is drawn in red.

The non-photonic raw yield still contains electrons from dielectron decays and weak Kaon decays (K_{e3}). Therefore, the dominate contributions of the remaining cocktail (K_{e3} and J/ψ) still had to be subtracted. This subtraction was done after correction for acceptance and efficiency and normalisation. The remaining cocktail components were taken from the cocktail belonging to the published result [13]. The contribution from dielectron decays of light vector mesons (ρ, ω and ϕ) are of no practical importance compared to contributions from the photonic sources [12].

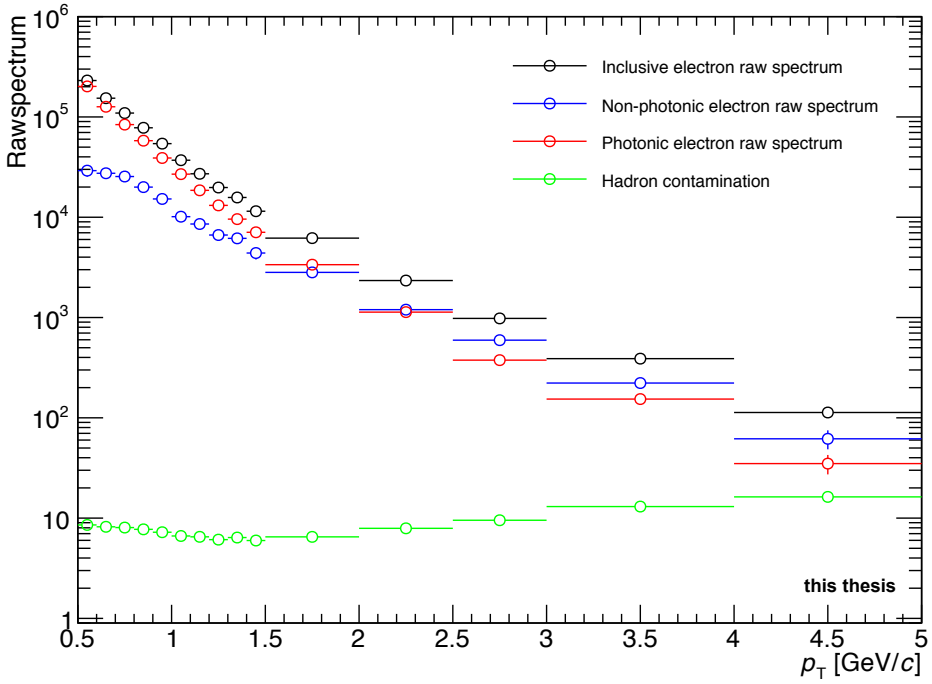

Figure 6.8: The raw inclusive, photonic and non-photonic spectrum as a function of transverse momentum as well as the hadron contamination.

6.6. Efficiency correction

The next step was to correct the raw spectrum of non-photonic electrons for the geometrical acceptance (ϵ_{geo}) of the detectors, the reconstruction efficiency (ϵ_{reco}) and the electron identification efficiency (ϵ_{eID}). The correction was done in a similar way to [13].

The efficiencies for geometrical acceptance, reconstruction and the electron identification with TOF were obtained from the full detector simulation included in the enhanced MC sample (LHC12a9), while the TPC electron identification efficiency was calculated as the integral of a Gaussian function with μ=0 and σ=1. The TPC PID selection interval (in between $-1.0\,\sigma_{\text{TPC,d}E/\text{d}x}$ and $-3.2\,\sigma_{\text{TPC,d}E/\text{d}x}$) corresponds to an efficiency of 84.07% which was corrected separately.

In addition, to the efficiency correction, the measured p_{T}-spectrum has to be corrected for effects of momentum resolution and energy loss in the detector material due to bremsstrahlung. Theses modifications of the p_{T}-spectrum can be expressed by a response matrix which acts on the natural distribution. To estimate the inverted response matrix, which is needed to restore the natural distribution, a Bayesian unfolding procedure was applied.

6.7. TOF correction factor

An additional correction factor for the TOF efficiency had to be introduced because the distributions of the TOF signals from electrons are different in data and MC. This correction factor f_{TOF} was evaluated using electron tracks, which had been identified as electron tracks from photon conversion via topological cuts and their invariant mass because, hereby, a rather clean electron sample was created. For these electron tracks, the track selection criteria listed in Table 6.3 were applied.

Table 6.3: Summary of the track selection imposed on the electron from photon conversion used to evaluate the TOF correction factor

Type	**TOF electron candidates**
η	0.8
ITS and TPC refit	required
χ^2/ TPC clusters	< 4
Number of TPC clusters	$\geq$110
Number of TPC $\frac{\mathrm{d}E}{\mathrm{d}x}$ clusters (PID)	$\geq$80
Number of ITS hits	$\geq$3
Distance of closest approach to the primary vertex in xy	< 1 cm
Distance of closest approach to the primary vertex in z	< 2 cm
Kink mothers	excluded
TPC $\frac{\mathrm{d}E}{\mathrm{d}x} - \left\langle \text{TPC } \frac{\mathrm{d}E}{\mathrm{d}x} \right\rangle\vert_{el}$	$\pm 3\,\sigma$

Differently from the analysis, we did not introduce any requirement on the SPD because demanding one hit in any of the SPD layers would already halve the statistics but the width and mean of the TOF distribution with and without SPD requirement are very similar, see Figure A.8.

Figure 6.9 shows the distribution of the TOF signals for electrons from photon conversion as a function of the particle momentum on the left panel and the projection of the TOF signals in the momentum range between 0.5 GeV/c and 1.0 GeV/c.

The distribution has a tail towards larger time-of-flight values and the mean μ and width σ of the Gaussian core of the distribution deviate from the expectation, μ=0 and σ=1. Comparing the distributions of the TOF signals in data and in the enhanced MC (LHC12a9), see Figure 6.10, we realized that both Gausssian cores have different means and widths.

By integrating the distributions in data and MC in within $\pm 3\,\sigma$ around the expected time-of-flight for electrons, an efficiency of (94,96 ±0.56)% for data and (97,0 ±1.7)% for MC was

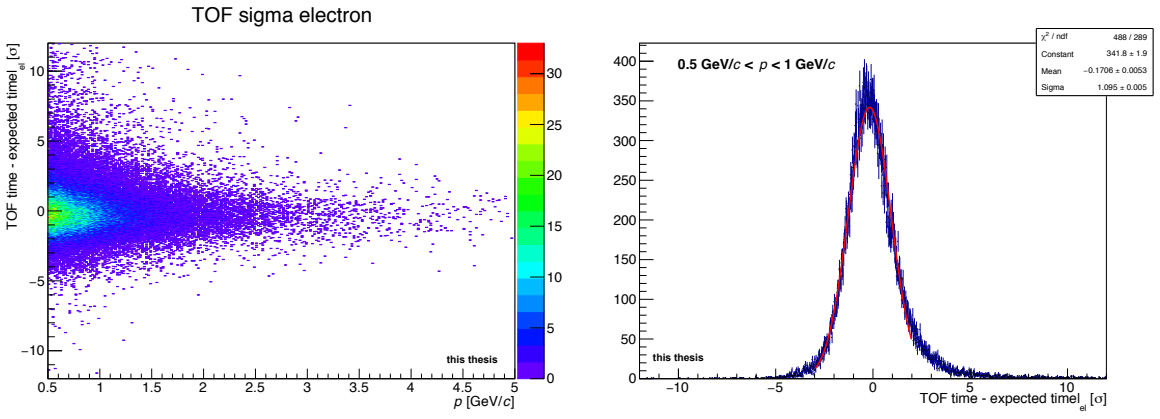

(a) TOF distribution

(b) Projection of the TOF signals in the momentum range $0.5\,\text{GeV}/c < p < 1.0\,\text{GeV}/c$

Figure 6.9: Panel (a) shows the distribution of the TOF signals for all selected tracks in data as a function of the particle momentum. The projection of the TOF signals in the momentum interval $0.5\,\text{GeV}/c < p < 1.0\,\text{GeV}/c$ is shown in panel (b).

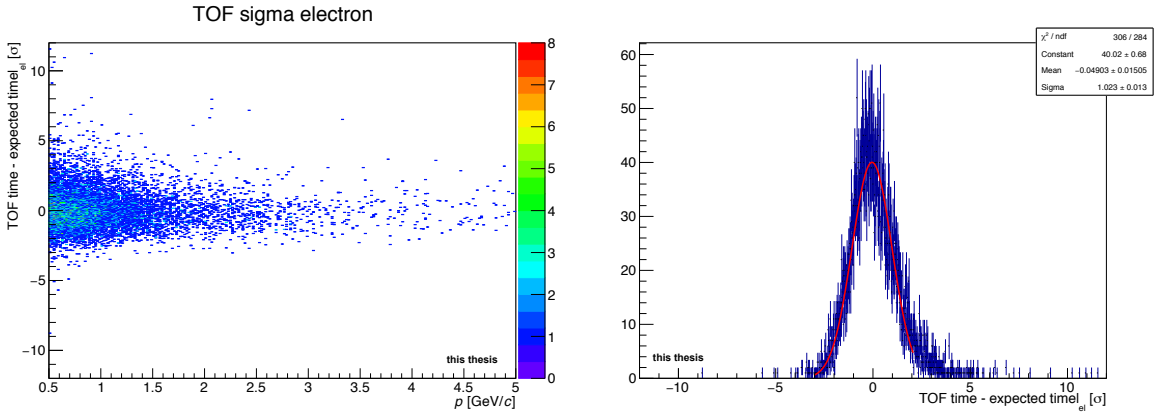

(a) TOF distribution

(b) Projection of the TOF signals in the momentum range $0.5\,\text{GeV}/c < p < 1.0\,\text{GeV}/c$

Figure 6.10: Panel (a) shows the distribution of the TOF signals for all selected tracks in the enhanced MC (LHC12a9) as a function of the particle momentum. The projection of the TOF signals in the momentum interval $0.5\,\text{GeV}/c < p < 1.0\,\text{GeV}/c$ is shown in panel (b).

found. The correction factor was evaluated by dividing the efficiency computed from real data by the one obtained from MC. The resulting correction factors for different TOF cuts are shown in Table 6.4. The uncertainties on the electron selection efficiencies in data and MC were propagated to the TOF correction factor for the TOF selection with in $\pm 3\,\sigma$ resulting in an uncertainty of 2%.

Table 6.4: The TOF correction factors for different TOF cuts obtained for MC (LHC12a9)

TOF selection[σ]	MC
±2.0	0.962
±2.5	0.971
±3.0	0.979
±3.5	0.984
±4.0	0.988
±5.0	0.993

The enhanced MC sample has very little statistics in terms of electrons from photon conversions because it was created with a triggering on events with heavy-flavour production which makes such electrons less common. Therefore, this check was performed for the other enhanced Pythia MC sample (LHC11b10b) and the minimum bias MC (LHC12e6) to confirm that the value is reasonable. Since the values from these MC samples differ at maximum by 0.5% for the TOF selection in between $\pm 3\,\sigma$, no further checks on the heavy-flavour enhanced MC sample (LHC12a9) were made.

6.8. Normalisation

The spectrum was normalized to the number of minimum bias events, which survive the event selection. The number of events was calculated using the following formula

$$N_{\text{MB}} = N_{\text{vertex}} + f_{\text{vertex}} \cdot N_{\text{no vertex}} \tag{6.5}$$

where f_{vertex} is the fraction of events which have passed the event selection criteria and $N_{\text{no vertex}}$ is the number of events where no vertex from track could be found. N_{vertex} denotes the number of events with a vertex from tracks which have passed the event selection. The second term is an estimated for the events without tracks in the central detectors but hits in the V0 detector which would have passed the event selection. It was needed because the minimum bias cross-section was measured including events which had only signals in the V0.

In addition, the measured yield of electrons from heavy-flavour decays was normalised to unit rapidity by dividing by the rapidity range $\Delta y = 1.6$. For electron, which have usually negligible mass compared to their momentum, the pseudorapidity and rapidity are the same. Therefore the rapidity range was determined by the pseudorapidity range $\Delta\eta = 2 \cdot 0.8$.

To obtain a production cross-section, the spectrum was multiplied with the minimum bias cross-section for pp collisions at $\sqrt{s} = 2.76\,\text{TeV}$, $\sigma_{\text{MB}} = (55.4 \pm 1.0)\,\text{mb}$. The minimum bias cross-section was measured via van-der-Meer scans in pp collisions selecting events which gave signals in the SPD or both sides of the V0 scintillator detector. The resulting cross-section had to be corrected for the difference in efficiency between requiring at least one hit in the V0 arrays (MB_{OR}) or hits in both (MB_{AND}). This was done by dividing by the normalisation factor $\frac{\text{MB}_{\text{AND}}}{MB_{\text{OR}}}$. More detailed information about the measurement of the minimum bias cross-section can be found in [38].

The final invariant production cross-section for electrons ($\frac{e^+ + e^-}{2}$) from heavy-flavour hadron decays was thus calculated using the following equation:

$$\frac{1}{2\pi p_{\text{T}}} \frac{\text{d}^2\sigma^{e^\pm}}{\text{d}p_{\text{T}}\text{d}y} = \frac{1}{2} \frac{1}{2\pi\, p_{\text{T}}^{\text{centre}}} \frac{1}{\Delta y \Delta p_{\text{T}}} \frac{N_{\text{raw}}^{e^\pm}(p_{\text{T}})}{(\epsilon^{\text{geo}} \times \epsilon^{\text{reco}} \times \epsilon^{\text{eID}}) \cdot f_{\text{TOF}}} \frac{\sigma_{\text{MB}}}{N_{\text{MB}}} \tag{6.6}$$

Figure 6.11 shows the cross-section for electrons from semi-electronic decays of beauty and charm hadrons measured in this analysis before evaluation of the systematic uncertainties.

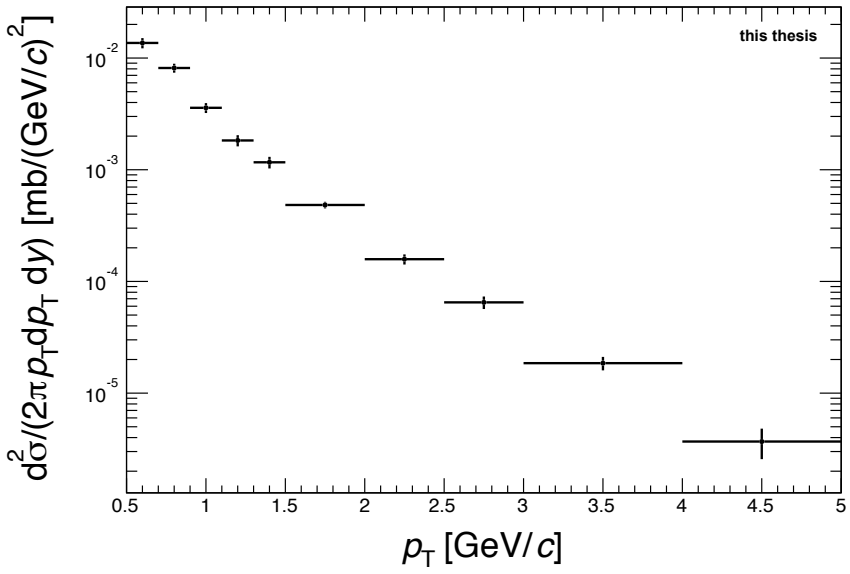

Figure 6.11: The p_{T}-differential cross-section for electrons from heavy-flavour hadron decays using the photonic method. The statistical uncertainties are shown as bars.

A MC closure test was performed to demonstrate that the photonic method can be applied to pp data to evaluate the cross-section of electrons from heavy-flavour hadron decays without biasing the result. The MC closure test was performed using two minimum bias MC samples produced using the Pythia and the Phojet event generators. For the MC closure

test, one of the MC samples was used as data and the other MC sample was used to evaluate the acceptance and efficiency. Since the MC samples were created using different generators, the distributions in the MC sample used to correct for acceptance and efficiency had to be re-weighted to correct their shapes to match the descriptions in the MC sample used as data. The resulting p_{T}-differential cross-section of electrons from semi-electronic decays of heavy-flavour hadrons should be equal to the simulated cross-section. Figure 6.12 shows the results of the MC closure test. The MC samples used for the MC closure test have very little statistics. Therefore, the number of tracks especially at high transverse momenta get very low and the photonic method cannot be used anymore to evaluate a precise value. This effect is reflected by the fact that cross-sections evaluated using the photonic method is too low above $p_{\mathrm{T}} = 3\,\mathrm{GeV}/c$ for the Pythia MC sample and above $p_{\mathrm{T}} = 2.5\,\mathrm{GeV}/c$ for the Phojet MC sample. Hence, the MC closure test is affected by the low statistics of the MC samples used but it does not show a sign of problems in the region where the statistics is large enough. Hence, the photonic method can be used in pp collisions.

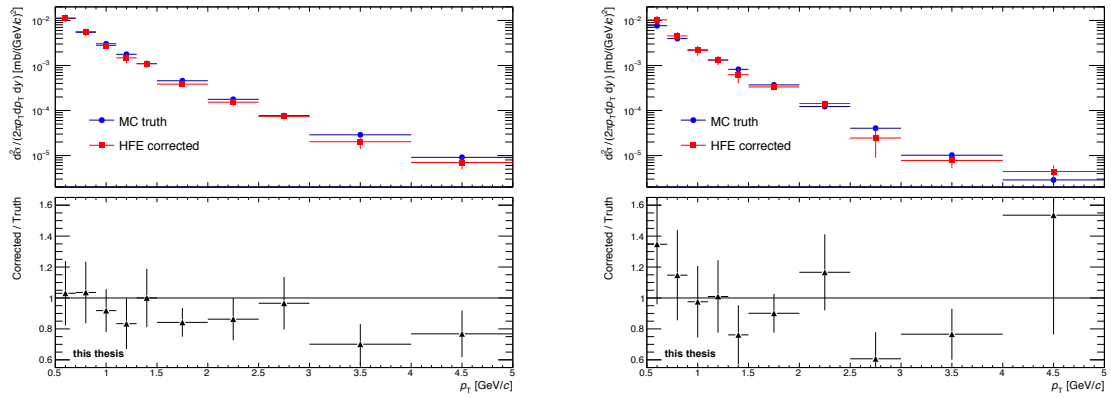

(a) Pythia as data

(b) Phojet as data

Figure 6.12: Comparison of the cross-section stored in the MC truth and the one evaluated using the photonic method. Here, one of the MC samples (LHC12f1a or LC12f1b) was used as data and the other one was used to correct for acceptance and efficiency. The distributions in the MC used to correct were re-weighted to match the ones in the MC used as data. Panel (a) shows the result when the Pythia MC sample was used as data and panel (b) the one using the Phojet MC sample as data.

6.9. Systematic uncertainties

To estimate the systematic uncertainties, the requirements for the track selection and electron identification were varied separately in a similar way as in [13]. The individual contributions were estimated looking at the ratio of fully corrected cross-sections.
If not mentioned differently the statistical uncertainties of the ratios shown in this section were calculated using binomial error propagation. The binomial error propagation takes the fact into account that the numerator is a sub-set of the denominator and, therefore, the uncertainties are correlated.

To ensure that the measured production cross-section of electrons from semi-electron decays of charm and beauty hadrons ($H_{b/c}$) is not biased by the lack of the information from the SDD, the cross-sections for the data samples with and without SDD were compared. Figure 6.13 shows that the results with and without the information from the SDD are compatible within statistical uncertainties. Hence, no contribution to the systematic uncertainty was assigned.

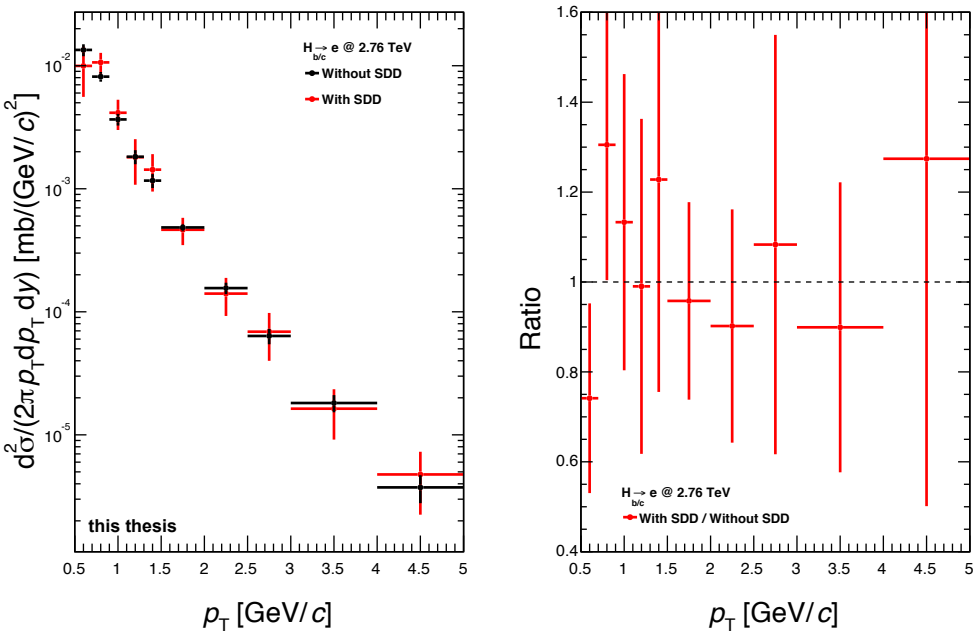

Figure 6.13: The cross-section for electrons from heavy-flavour hadron decays evaluated using the data sample with and without the information from the SDD.

6.9.1. Systematic uncertainties belonging to the selection of electron candidates

The spectrum of electrons from heavy-flavour hadron decays has limited statistics which restricts the precision and sensitivity of estimating the systematic uncertainties via ratios of differential cross-sections obtained by varying the track selection criteria. Therefore, the systematic uncertainty from track selection criteria, which do not depend on the source of the electron tracks, was evaluated using the spectrum of the inclusive electrons to profit from the higher statistics compared to the spectrum of electrons from heavy-flavour decays.

Table 6.5: Summary of the systematic uncertainties linked to the track selection and particle identification for electron candidate tracks

Source of Uncertainty	Reference	Variations	Uncertainty
TPC clusters[1]	110	100, 105, 115, 120	1%
TPC PID clusters[1]	80	70, 75, 85, 90	negligible
ITS hits	3	2, 4	negligible
SPD	kBoth	kAny, kFirst	20% for 0.5-0.7 GeV/c
DCA radial	1 cm	2 cm, 0.5 cm	negligible
DCA z	2 cm	4 cm, 1 cm	negligible
Kink mothers[1]	Excluded	Included	2% above 1.5 GeV/c
TOF PID[1]	3.0 σ	2.0 σ, 2.5 σ, 3.5 σ, 4.0 σ, 5.0 σ	covered by the uncertainty of the correction factor
TPC PID lower boundary[1]	-1.0σ	0.25 σ, -0.0 σ, -0.25 σ, -0.5 σ, -0.75 σ, -1.3 σ	negligible
TPC PID upper boundary[1]	3.2 σ	1.0 σ, 1.5 σ, 2.0 σ	1%

[1] These tests were performed on the inclusive electron yield and the cross-section of electrons from heavy-flavour hadron decays.

- The quality requirements of the tracks in the TPC was varied by changing the minimum number of clusters used. For this check, the parametrisation of the hadron contamination from the standard track selection was used but by requiring more clusters used for tracking, electrons and pions can be distinguished better because electrons in average have a larger number of clusters than minimum ionizing particles. Therefore, the deviations in the last bin were expected to be larger than in the other bins because in

this bin the hadron contamination, which is mostly misidentified pions, has the largest impact on the measured production cross-section. This effect is also visible when the number of PID clusters was varied because the number of PID clusters and the number of clusters used for tracking depend on each other. For the variation of the TPC clusters used for tracking and the calculation of the energy loss a systematic uncertainty of 1% was assigned, see Figure 6.14.

- The maximum number of hits in the ITS was reduced to 4 instead of 6 because the SDD was not used for reconstruction in the data sample used in this analysis. Therefore, using only tracks which have 4 hits in the ITS will largely reduce the number of tracks. In addition the minimum number of hits in the ITS was limited to two by the additional requirement of having 2 hits in the SPD. Figure A.9 indicates that the track selection using the ITS information does not correspond to a systematic uncertainty.

- To test the robustness of the photonic method against taking more electrons from photon conversion into account the SPD requirement was lowered to ask for at least one hit in any of the layers because this adds all electrons from photons converting in the first layer and in the very first part of the second layer to the electron candidate tracks. In addition, the cross-section was determined with a SPD selection asking for at least one hit in the first layer. For both variations, more tracks from photon conversion to which a hit in the first SPD layer was assigned falsely, are kept in the electron candidate sample. Figure 6.15 shows that, for these looser SPD requirements, more tracks were kept in the region below 1.5 GeV/c which were not compensated by the efficiency corrections because they are not included in the MC description to the same amount. Since the information from the SDD improves the tracking in the ITS, the variation of the SPD requirement was cross-checked using the data sample where the information of the SDD is available, see Figure 6.15. Using this data sample, no effect from changing the SPD requirement was visible. Hence, the structure in the data sample without SDD seems to be caused by keeping to many electron candidate tracks which are not from decays of heavy-flavour hadron decays. We used the additional information from the data sample with SDD and assigned 20% systematic uncertainty linked to the SPD requirement in thep_{T}-region from 0.5 to 0.7 GeV/c because both data samples show an excess in this kinematic region.

- To test the systematic effect of the maximum distance of closest approach (DCA) for electron candidate tracks in the radial and z direction the value of this selection cri-

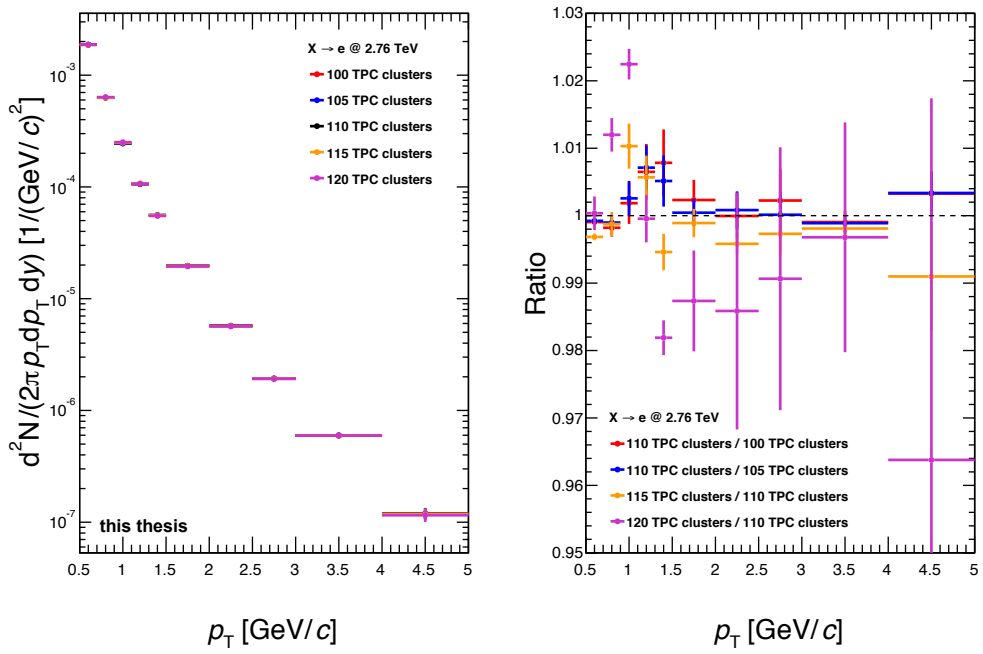

(a) TPC clusters

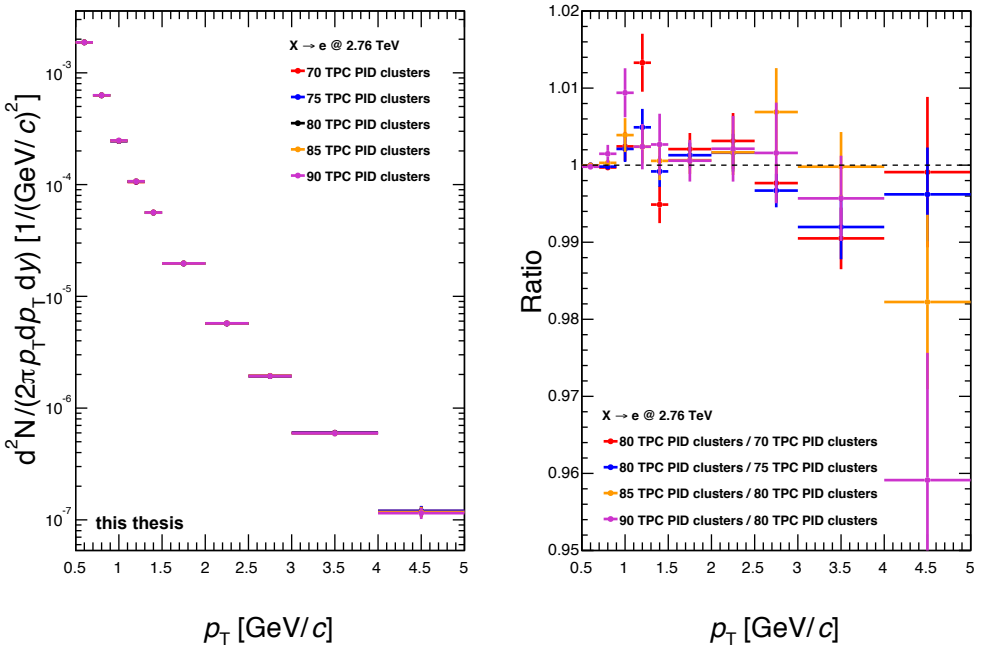

(b) TPC PID clusters

Figure 6.14: Variation of the required TPC clusters for tracking and PID of electron candidate tracks performed on the inclusive spectrum. The variation of the clusters used for tracking is shown in panel (a) and panel (b) displays the ones used for the energy loss calculation.

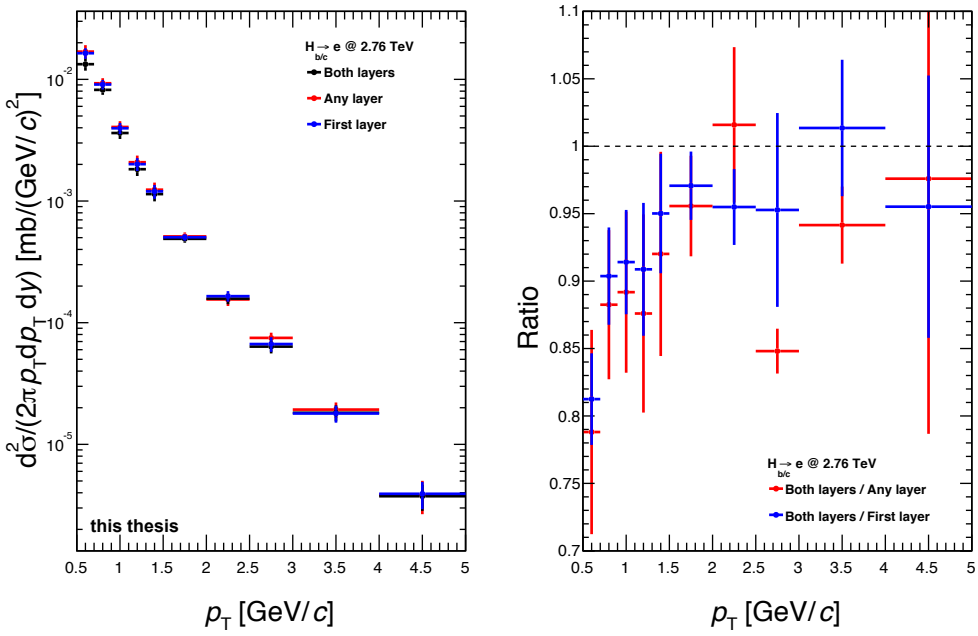

(a) Without SDD

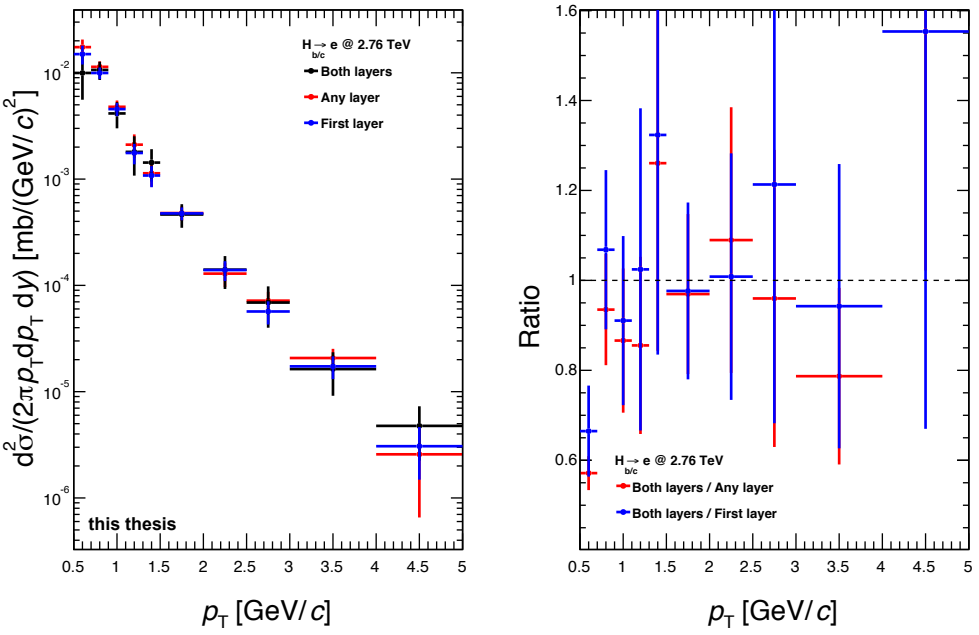

(b) With SDD

Figure 6.15: The production cross-section for electrons from semielectronic decays of beauty and charm hadrons for different requirements on the hits in the SPD on electron candidate tracks with and without SDD information. For panel (a) the data sample without SDD information was used and panel (b) shows the same variation for the data sample with the information from SDD.

terion was varied by a factor of 2. Since the resulting cross-sections are compatible within statistical uncertainties, no systematic uncertainty was assigned, see Figure A.10.

- As mentioned before kink mothers were excluded from the analysis, but if the description and abundance of such tracks in the MC simulation is consistent with data, the analysis result should not change when including this type of tracks. Therefore, the analysis was repeated including the kink mothers and the result was compared with the result excluding kink mothers. The difference between including and excluding the kink mothers is shown in Figure 6.16 and corresponds to 2% systematic uncertainty above 1.5 GeV/c. The problematic of the kink mothers is one of the issues which have to be investigated further in future.

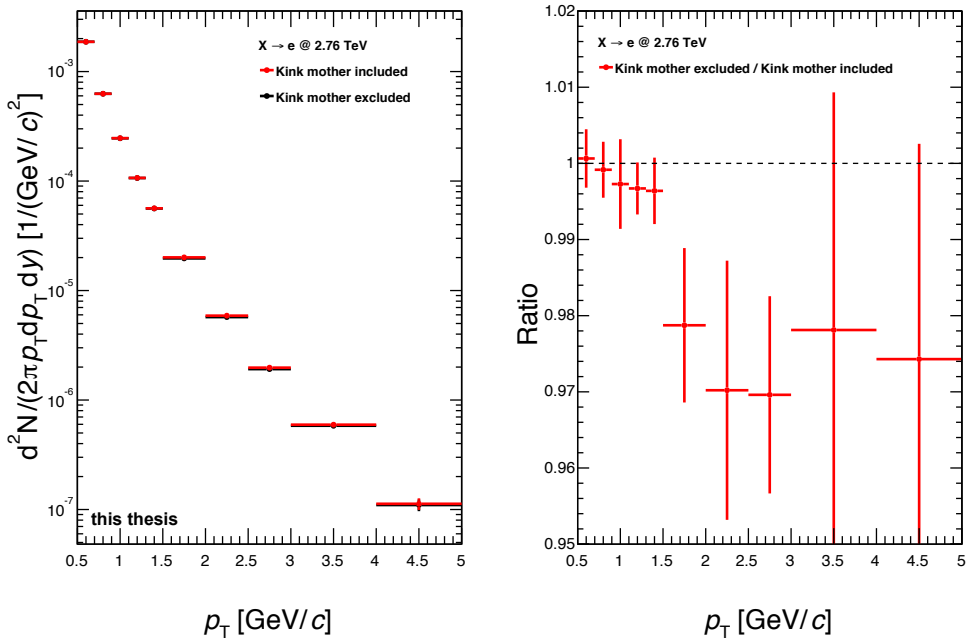

Figure 6.16: The yield of inclusive electrons evaluated excluding and including the kink mothers.

- For the variation of the TOF PID selection, the respective TOF correction factors for the different selection intervals were used. Figure 6.17 clearly shows that the maximum deviation from the variation of the TOF PID requirement is about 2% at high p_T and even lower for the other p_T-regions. Since the uncertainty on the TOF correction factor is already 2%, we did not assign any additional uncertainty linked to the TOF PID.

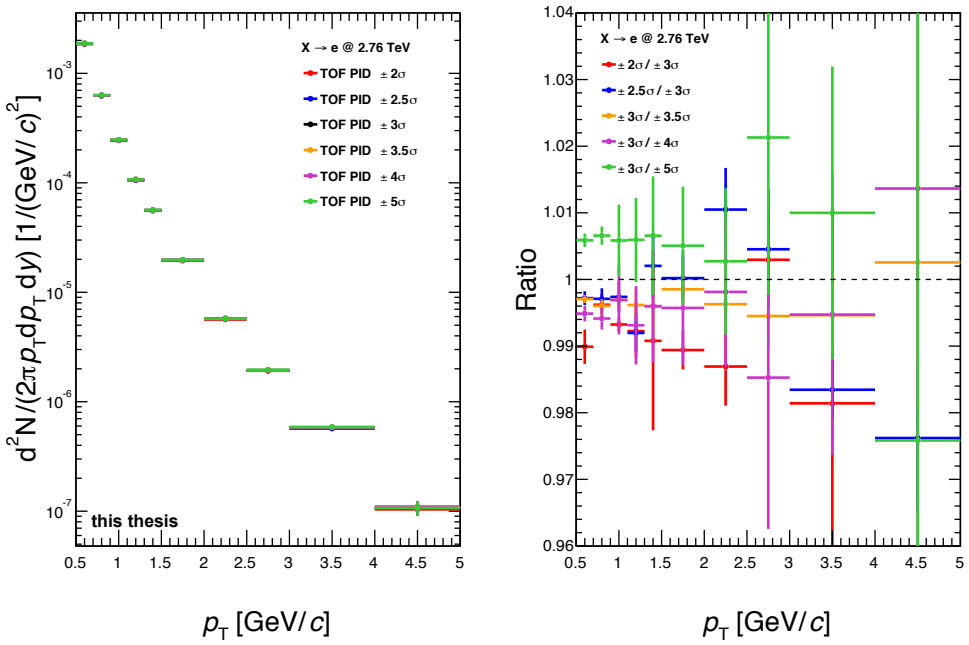

Figure 6.17: The variation of the TOF PID cuts for electron candidate tracks performed on the inclusive spectrum.

- In contrast to the test performed on the TPC clusters, the hadron contamination was not subtracted when varying the TPC PID requirement. This leads to larger deviations in the last bin compared to the other bins when varying the lower bound of the TPC PID selection criterion because the amount of misidentified hadrons depends on this selection. If the lower boundary of the TPC PID requirement was chosen to be 0.25 σ above the expected electron signal, no hadron contamination was expected but the reference, which has a lower boundary at -1.0 σ, is affected by an hadron contamination described by Equation 6.2. Therefore, the ratio of these cross-sections was expected to be about 17% below 1 in the last bin. According to Figure 6.18, a systematic uncertainty belonging to the TPC PID selection accounts for 1%.

6.9.2. Systematic uncertainties due to the photonic electron subtraction

- The restriction on the minimum transverse momentum of the associated track does not contribute to the systematic uncertainty. The respective plot can be found in the appendix (Figure A.11).

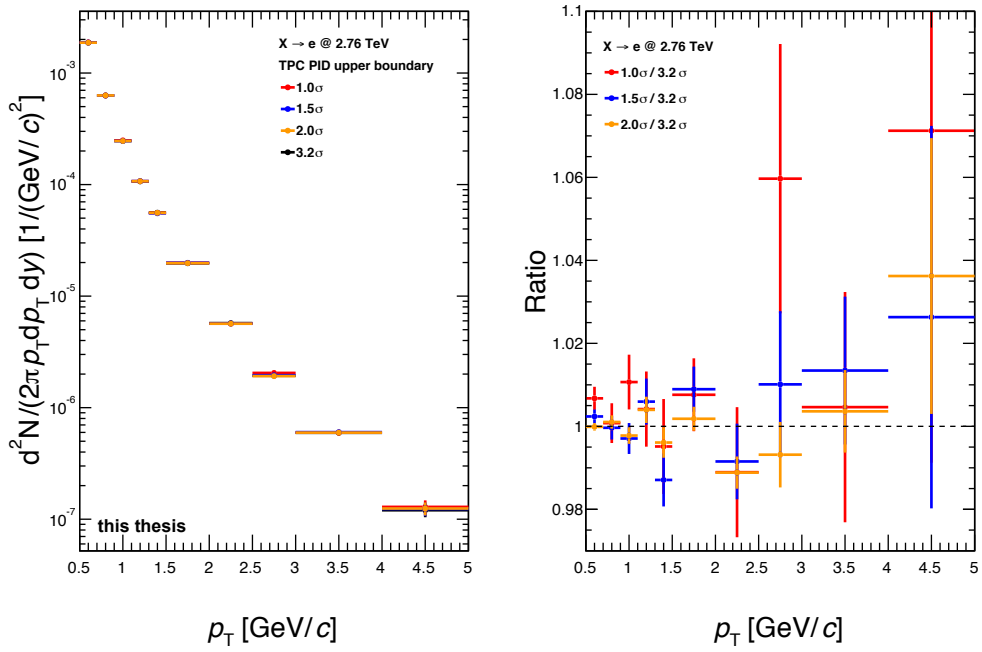

(a) TPC PID upper boundary

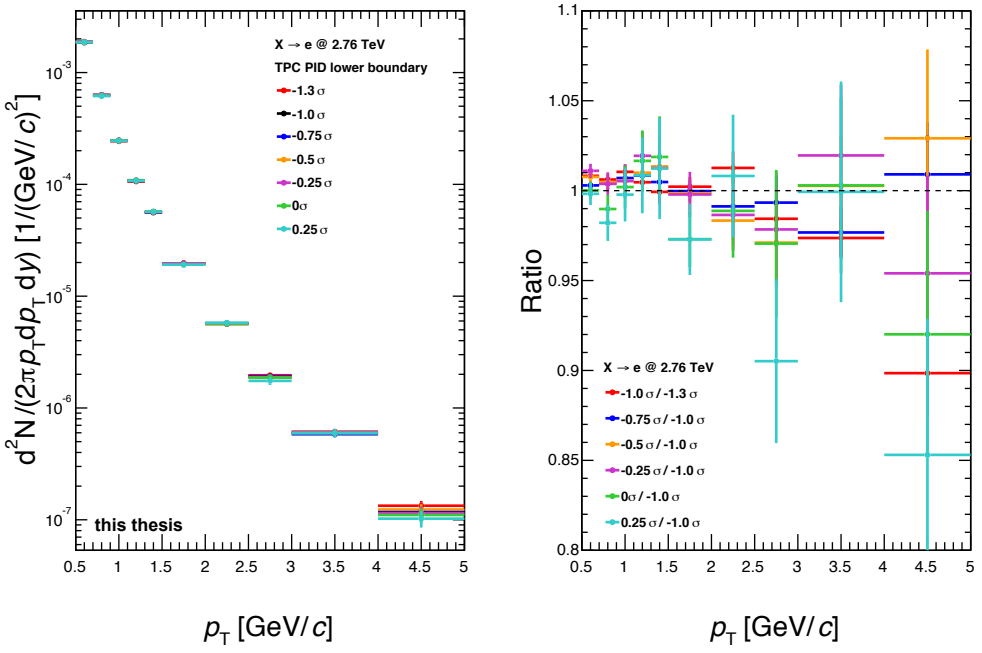

(b) TPC PID lower boundary

Figure 6.18: The variation of the TPC PID cuts on electron candidate tracks performed on the inclusive spectrum. The variation of the upper boundary of the TPC PID selection is shown in panel (a) and panel (b) displays the variation of the lower one.

Table 6.6: Summary of the systematic uncertainties linked to the photonic electron subtraction

Source of Uncertainty	Reference	Variations	Uncertainty
$p_{\text{T}}^{\text{min}}$	$0.1\,\text{GeV}/c$	$0.0\,\text{GeV}/c$, $0.05\,\text{GeV}/c$, $0.15\,\text{GeV}/c$	negligible
TPC (PID) clusters	60 (60)	80 (50 , 60, 70, 80), 70 (50), 60 (50), 50 (50)	2%
ITS hits	2	1, 3	2% above $3.0\,\text{GeV}/c$
DCA radial	1 cm	2 cm, 0.5 cm	1%
DCA z	2 cm	4 cm, 1 cm	negligible
TPC PID	$3.0\,\sigma$	$2.0\,\sigma$, $4.0\,\sigma$	1%
Pair mass	$0.14\,\text{GeV}/c^2$	$0.10\,\text{GeV}/c^2$, $0.12\,\text{GeV}/c^2$, $0.16\,\text{GeV}/c^2$, $0.18\,\text{GeV}/c^2$, $0.20\,\text{GeV}/c^2$	1%
Method of calculating the tagging efficiency	MC truth	US-LS	2% below $1.5\,\text{GeV}/c$
Weights	standard	tilted up, tilted down	5% for 0.5-0.7 GeV/c 2% for 0.7-0.9 GeV/c 1% below $1.5\,\text{GeV}/c$

- According to Figure 6.19, the variation of the minimum number of clusters used for tracking and the calculation of the energy loss in the TPC accounts for 2% systematic uncertainty.

- For the associated electron candidates a restriction on the minimal number of hits in the ITS was used. Changing this requirement from at least 2 hits to 1 hit or 3 hits, respectively, has no influence on the result below $3\,\text{GeV}/c$ which has to be taken into account for the systematic uncertainty. Above $3\,\text{GeV}/c$, a systematic uncertainty of 2% was assigned, see Figure 6.20.

- The analysis was performed requiring a maximum distance of closest approach (DCA) to the primary vertex of 1 cm in radial direction and 2 cm along the beam axis for the associated electron tracks. The DCA was varied in the same way as for the electron candidate tracks and according to Figure A.12 1% systematic uncertainty was assigned.

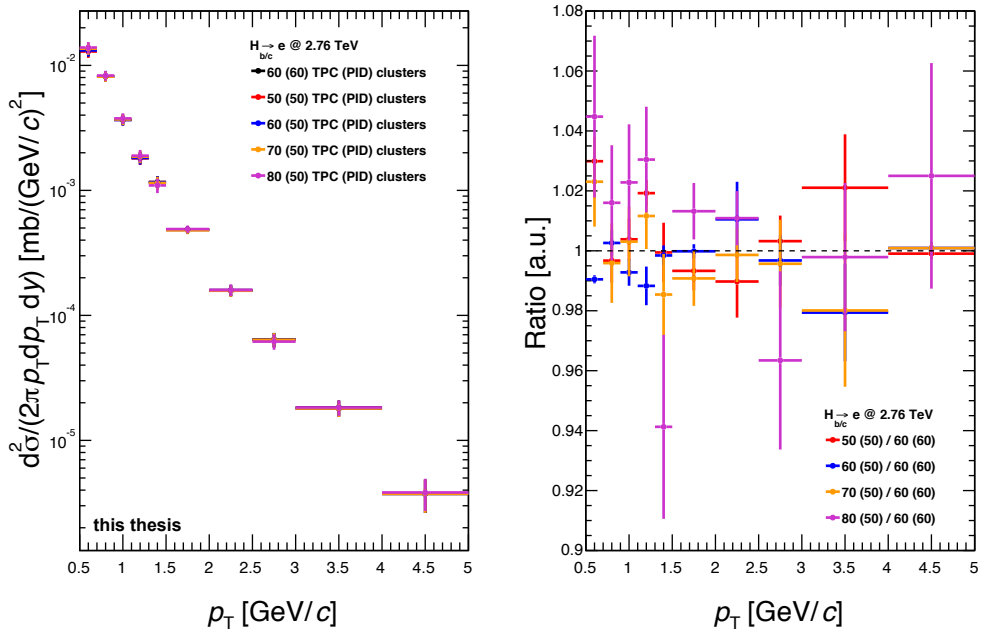

(a) TPC clusters

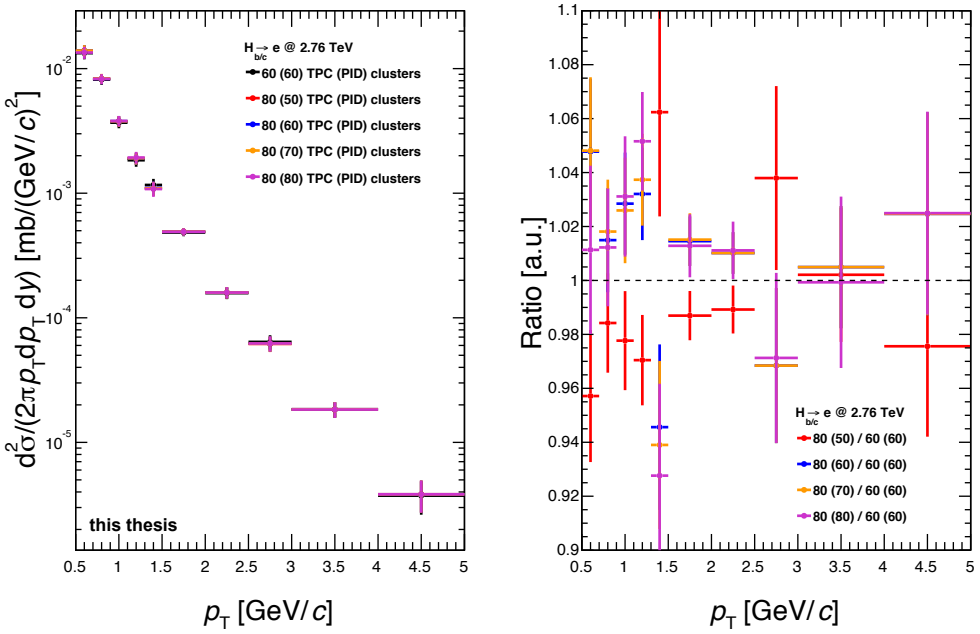

(b) TPC PID clusters

Figure 6.19: The variation of the required TPC clusters for tracking and PID on associated electron tracks.

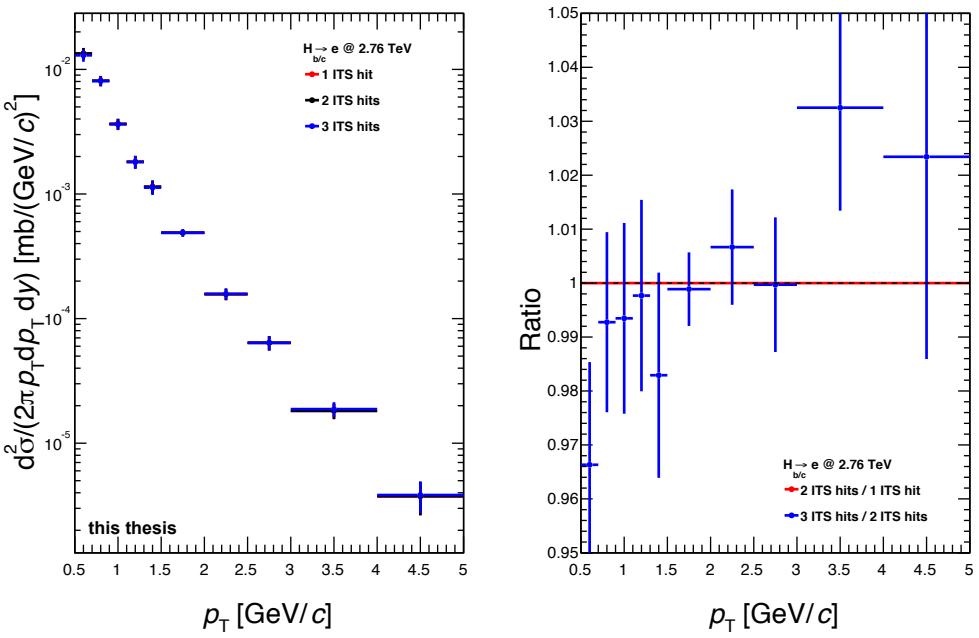

Figure 6.20: The variation of the requirements on the number of ITS hits for associated electron tracks.

- Figure 6.21 indicates that the systematic uncertainty linked to the loosening or tightening of the track selection based on the TPC PID for the associated electrons is 1%.

- Varying the maximum invariant mass still taken into account for this analysis, yields a systematic uncertainty of 1%, see Figure A.13.

- By default, the tagging efficiency is evaluated using the number of identified electrons from the MC truth. This information can be obtained using unlike sign and like sign pairs in a similar way as for data, too. Therefore, the results using the two different methods to compute the tagging efficiency were compared. According to Figure 6.22, the result was only influenced by the difference of the tagging efficiencies below $p_T = 1.5\,\text{GeV}/c$ where a systematic uncertainty of 2% was assigned.

- As mentioned before the transverse momentum distribution of the photonic sources is not described correctly in the MC simulations, which leads to the need of weights to correct the shape of those distributions. The weights were calculated using the central values of the measured spectrum of π^0 and depend on the slope of the spectrum of

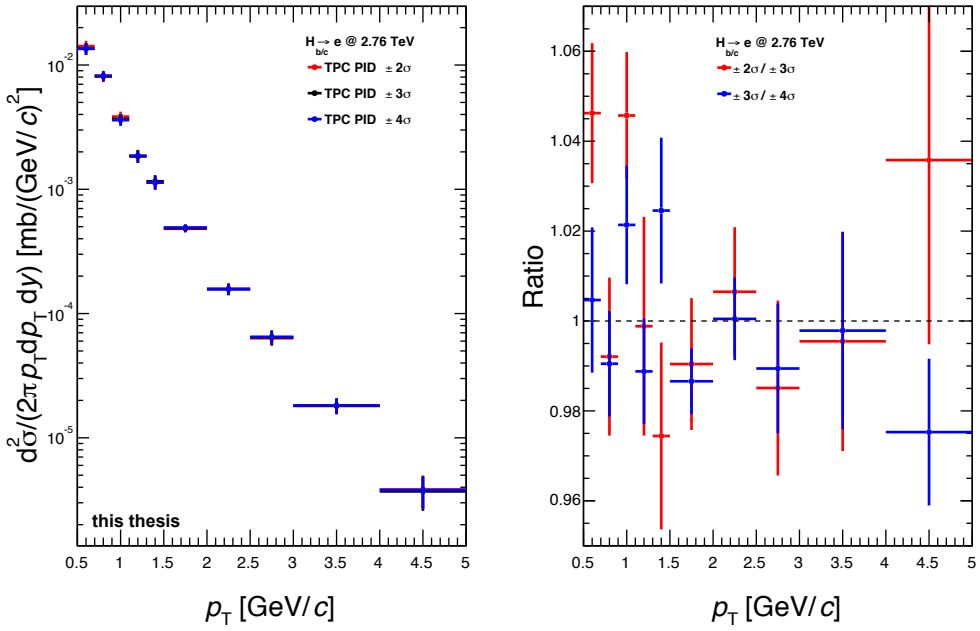

Figure 6.21: The variation of the TPC PID selection for associated electron tracks.

π^0 used. Therefore, additional weights were calculated for which the measured values at the lowest transverse momenta measured were shifted up by their systematic uncertainties and the values at the highest transverse momenta were shifted down, and vice versa, see Figure A.14. The values in between the lowest and the highest p_T were obtained by interpolation. Using these weights the systematic uncertainty introduced by re-weighting the distributions on the enhanced MC sample (LHC12a9) was evaluated. The first two bins (0.5-0.7 GeV/c and 0.7-0.9 GeV/c) are affected by an uncertainty of 5% and 2%, respectively. The remaining bins are only influenced by 1% up to $p_T = 1.5$ GeV/c, see Figure 6.23.

6.9.3. Systematic uncertainties from other sources

- For this analysis, events with a primary vertex reconstructed using tracks was used. To ensure that this choice did not bias the result, the cross-section was evaluated keeping the event if the primary vertex was reconstructed with the information from the SPD, too. For these events an additional requirement on the resolution of the vertex z position was introduced if only the z position of the vertex was reconstructed. The

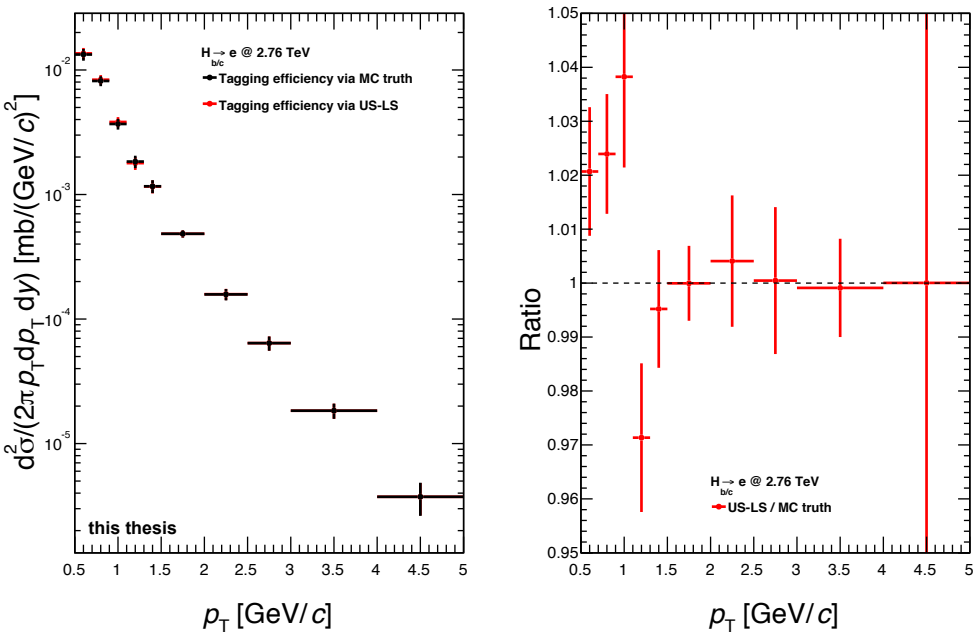

Figure 6.22: Comparison of the cross-section using the two methods for evaluating the tagging efficiency.

resolution along the beam direction had to be better than 0.25 cm. Figure A.15 shows that the choice of events with track vertex only does not bias the result.

- The analysis was performed using tracks inside $|\eta| < 0.8$ which is close to the maximum acceptance of the detectors used. To ensure that the result was not affected by problems caused by being at the edges of the detectors, the cross-section inside $|\eta| < 0.7$ and $|\eta| < 0.6$ was determined and compared to the reference result. The η-range used for this analysis is fine and no systematic uncertainty linked to the η-range was found, see Figure A.16 in the appendix.

- The systematic uncertainties linked to the track matching were taken from [12, 13]. For the matching of the information from TOF and the TPC, the uncertainty was taken from [12, 13].

- At high transverse momenta, the hadron contamination starts to play an important role. To estimate the systematic uncertainty corresponding to the method to determine it and the subtraction procedure, the fit of the fraction of hadron contamination was repeated using a Landau function as functional form and moving the point at the

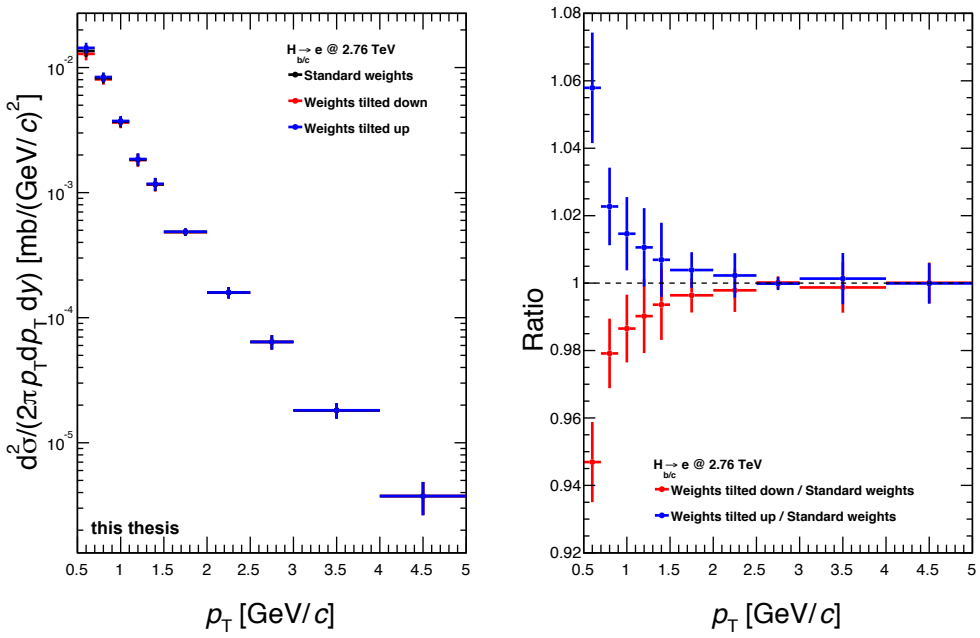

Figure 6.23: Comparison of the production cross-sections obtained using weights from tilted pion spectra to the reference weights.

upper and lower edges of the statistical uncertainty, see Figure A.17 in the appendix. In accordance with Figure 6.24, 3% and 8% systematic uncertainty were assigned for 3-4 GeV/c and for 4-5 GeV/c, respectively.

- The stability of the unfolding procedure used to correct for acceptance and efficiency was checked by varying the number of iterations used. Comparing the results for 8, 100 and 1000 iterations with the reference cross-section which was evaluated using 10 iterations proves the stability of the unfolding procedure used, see Figure A.18 in the appendix.

- In addition, the cross-section corrected for acceptance and efficiency extracted from the minimum bias MC sample (LHC12e6) using the unfolding procedure and direct correction were compared to ensure that the unfolding procedure was not biasing the result, see Figure A.19. For the direct correction method the tracking efficiency from MC as a function of the reconstructed transverse momentum after the simulation of the detector response is used to divide the raw spectrum for electrons from heavy-flavour hadron decays with. This test was performed using the minimum bias MC sample because the shape of the transverse momentum distributions of the electrons in the

Table 6.7: Summary of the systematic uncertainties neither linked to the track selection and particle identification for electron candidate nor to the subtraction of the photonic electrons directly

Source of Uncertainty	Reference	Variations	Uncertainty
Event selection	Primary vertex from long tracks only	Primary vertex from long tracks and SPD	negligible
$\|\eta\|$	0.8	0.6, 0.7	negligible
Track matching [12, 13]			2%
TPC-TOF matching			2%
Hadron contamination	Error function	Landau function, fit to upper and lower edges of the contamination	3% for 3-4 GeV/c 8% for 4-5 GeV/c
Unfolding	10 iterations	8, 100, 1000	negligible
Efficiency correction method	unfolded	direct	negligible
TOF correction factor			2%
Remaining cocktail components (J/ψ, K_{e3})			3.8% for 0.5-0.7 GeV/c 1.1% for 0.7-0.9 GeV/c 2.4% for 4-5 GeV/c
MC closure	-	Minimum bias MC generated with Pythia or Phojet	negligible

enhanced MC (LHC12a9) do not match the ones in data. This mismatch is caused by the triggering on events with heavy-flavour quark production and leads to the need of applying the Unfolding procedure.

- Additional contributions to the systematic uncertainty are the uncertainty belonging to the TOF correction factor (2%) and the systematic uncertainty of the remaining cocktail components (J/ψ, K_{e3}).

6.9.4. Total systematic uncertainty

The total systematic uncertainty was calculated by summing the different contributions in quadrature because these were considered as uncorrelated which is already reflected by in-

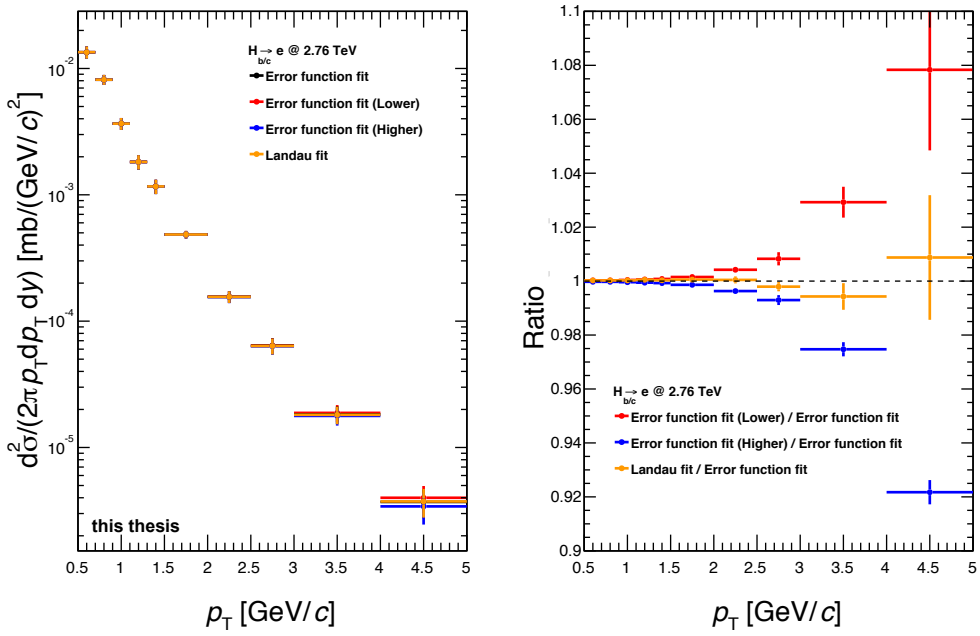

Figure 6.24: The variation of the function used to describe the hadron contamination.

vestigating the variations separately. The resulting systematic uncertainty for the different transverse momentum bins are summarized in Table 6.8.

Table 6.8: Summary of the total systematic uncertainties

Transverse momentum range	Total systematic uncertainty
0.5-0.7GeV/c	21.5%
0.7-0.9GeV/c	5.5%
0.9-1.1GeV/c	5.1%
1.1-1.3GeV/c	5.1%
1.3-1.5GeV/c	5.1%
1.5-2.0GeV/c	5.0%
2.0-2.5GeV/c	5.0%
2.5-3.0GeV/c	5.0%
3.0-4.0GeV/c	6.2%
4.0-5.0GeV/c	9.9%

The uncertainty belonging to the minimum bias cross-section is given separately and is called normalization uncertainty in the following.

6.10. Result

The p_{T}-differential cross-section for electrons from heavy-flavour hadron decays at mid rapidity in pp collisions at $\sqrt{s} = 2.76\,\text{TeV}$ using the photonic method is shown in Figure 6.25.

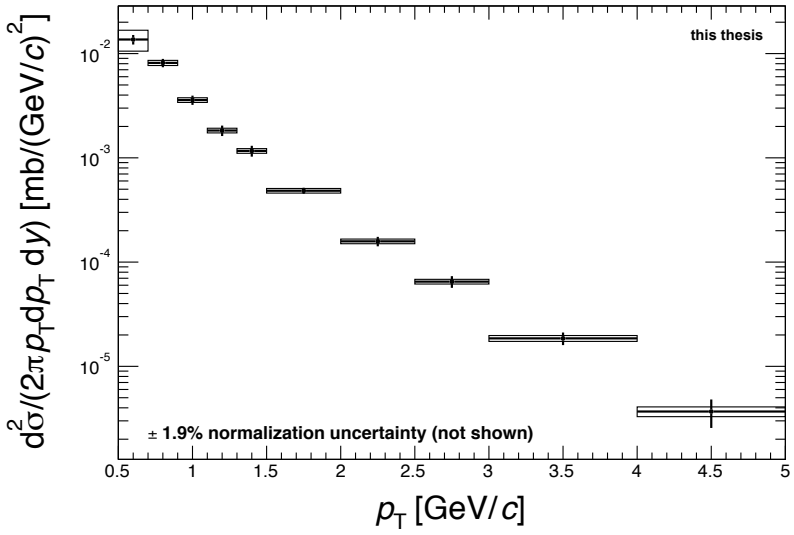

Figure 6.25: The p_{T}-differential cross-section for electrons from heavy-flavour hadron decays at mid rapidity in pp collisions at $\sqrt{s} = 2.76\,\text{TeV}$ using the photonic method. The statistical and systematic uncertainties are shown as bars and boxes, respectively.

To compare the cross-sections, calculated in this thesis and the published one [13], the binning of the published result had been adjusted to the new binning by averaging neighbouring bins according to

$$c_{\text{new}} = \frac{c_1 \cdot p_{\text{T},1} + c_2 \cdot p_{\text{T},2}}{p_{\text{T},1} + p_{\text{T},2}} \tag{6.7}$$

Here, c_1 and c_2 are the values of the cross-section in the first and second bin, respectively, while $p_{\text{T},1}$ and $p_{\text{T},2}$ are the corresponding mean transverse momenta. The statistical uncertainties of the bins were added in quadrature and divided by the number of bins added up taking the mean transverse momentum of the bins into account. Assuming that the systematic uncertainties in neighbouring bins are correlated, these were added linearly.

$$\Delta_{\text{stat.,new bin}} = \frac{\sqrt{(\Delta_{\text{stat.,bin1}} \cdot p_{\text{T},1})^2 + (\Delta_{\text{stat.,bin2}} \cdot p_{\text{T},2})^2}}{p_{\text{T},1} + p_{\text{T},2}} \tag{6.8}$$

$$\Delta_{\text{syst.,new bin}} = \frac{(\Delta_{\text{syst.,bin1}} \cdot p_{\text{T},1} + \Delta_{\text{syst.,bin2}} \cdot p_{\text{T},2})}{p_{\text{T},1} + p_{\text{T},2}} \tag{6.9}$$

The photonic method was applied to reduce the systematic uncertainties compared to the published result for which the cocktail-subtraction method was used. Figure 6.26 demonstrates that cross-section measured in this analysis has remarkable lower systematic uncertainties, especially for the bins up to $p_{\mathrm{T}} = 2.5\,\mathrm{GeV}/c$. In this transverse momentum range, it was reduced by more than a factor of 3. A direct comparison of the systematic uncertainties of the result of this analysis and the published one can be found in Table 6.9.

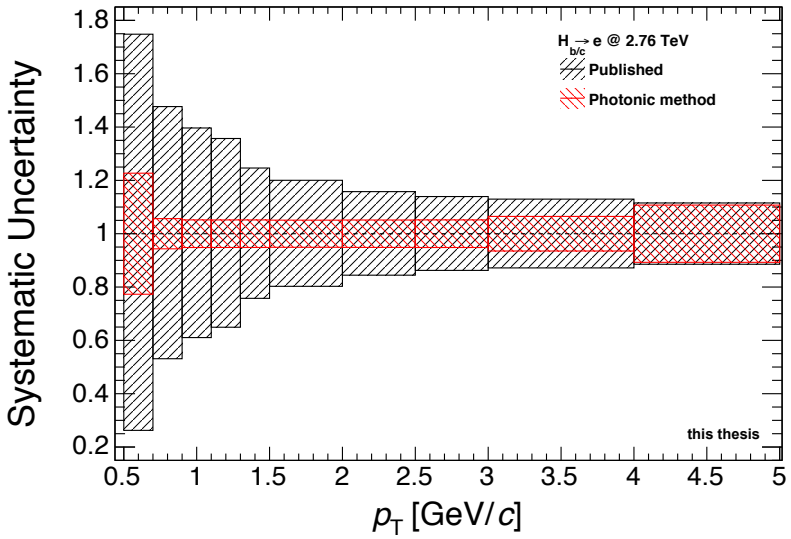

Figure 6.26: Comparison of the new systematic uncertainties and the published ones.

Table 6.9: Comparison of the total systematic uncertainty of the cross-section evaluated in this thesis and the published one.

p_{T} range	Photonic method	Published Lower Uncertainty	Published Upper Uncertainty	Reduction factor
0.5-0.7GeV/c	21.5%	73.8%	74.8%	3.5
0.7-0.9GeV/c	5.5%	46.9%	47.7%	8.6
0.9-1.1GeV/c	5.1%	39.0%	39.7%	7.7
1.1-1.3GeV/c	5.1%	35.1%	35.7%	6.9
1.3-1.5GeV/c	5.1%	24.2%	24.6%	4.8
1.5-2.0GeV/c	5.0%	19.7%	20.0%	4.0
2.0-2.5GeV/c	5.0%	15.6%	15.8%	3.1
2.5-3.0GeV/c	5.0%	13.8%	13.9%	2.8
3.0-4.0GeV/c	6.2%	12.8%	13.0%	2.1
4.0-5.0GeV/c	9.9%	11.5%	11.5%	1.2

Even though the new result is about 20% higher it is compatible with the published result within uncertainties, see Figure 6.27.

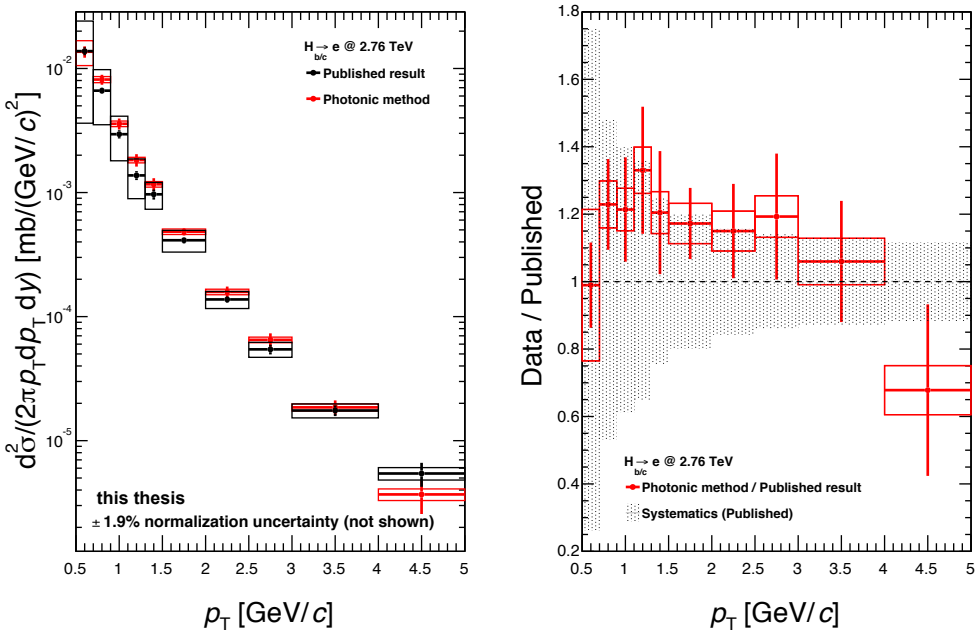

Figure 6.27: The cross-section of electrons from heavy-flavour decays compared to the published result. The statistical and systematic uncertainties are shown as bars and boxes, respectively.

The large deviation in the last bin (4-5 GeV/c) is an effect of having very limited statistics. This problem can be cured by using a slightly different analysis approach for the data at intermediate p_{T} where the requirement on the TOF is removed. For the published result, this analysis type was used above 2.0 GeV/c and was combined with the TPC-TOF approach and an analysis based on the EMCal using triggered events which was employed to evaluate the cross-section above 4.5 GeV/c [13].

The difference between the new and the published result is caused by two different aspects. First of all, the inclusive electron spectrum evaluated using the recent analysis code is 2% higher than the one belonging to the published result, see Figure 6.28.

Both inclusive electron spectra shown were determined using the TPC and TOF detector to identify electron candidates. This difference is caused by changes in the way the information from the TOF detector is used in the current ALICE analysis framework.

In addition to the difference of the inclusive electron spectrum, the corrected yield of the electrons from photonic sources is about 3% lower than the one for electrons from conver-

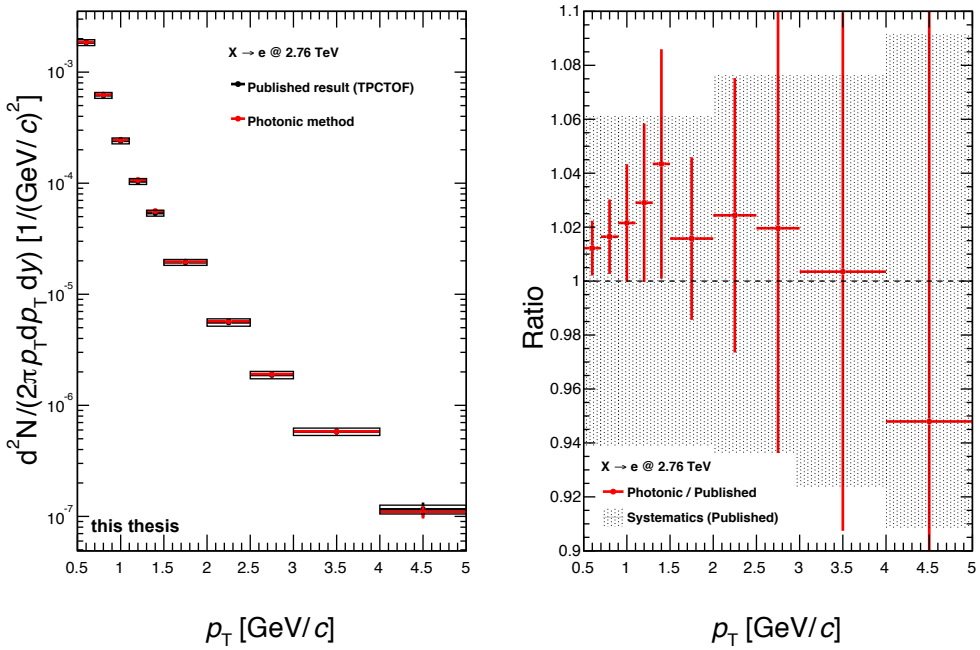

Figure 6.28: The inclusive electron spectrum corrected for efficiencies using the enhanced MC (LHC12a9) compared to the inclusive electron spectrum of the publication where the electron candidates were selected using the TOF detector and the TPC.

sions or decays of light particles but still compatible within uncertainties, see Figure 6.29. For this comparison, the systematic uncertainties of the photonic spectrum were evaluated varying the track selection criteria linked to the selection of electrons from photonic sources.

Since the signal-to-background ratio is very low, this difference of 3% between the background estimation accounts for about half of the difference of the published and the new cross-section, see Figure 6.30.

In Figure 6.31, the cross-section of electrons from semi-electronic decays of beauty and charm hadrons measured with the photonic method is compare to pQCD calculations from FONLL [2]. In addition, the published result is shown for completeness. The uncertainty on the FONLL calculations from different choices for the quark mass, factorization and normalisation scale, as well as the uncertainty from the PDF set used, are indicated by the red boxes. The FONLL calculation is consistent with both measurements of the production cross-section.

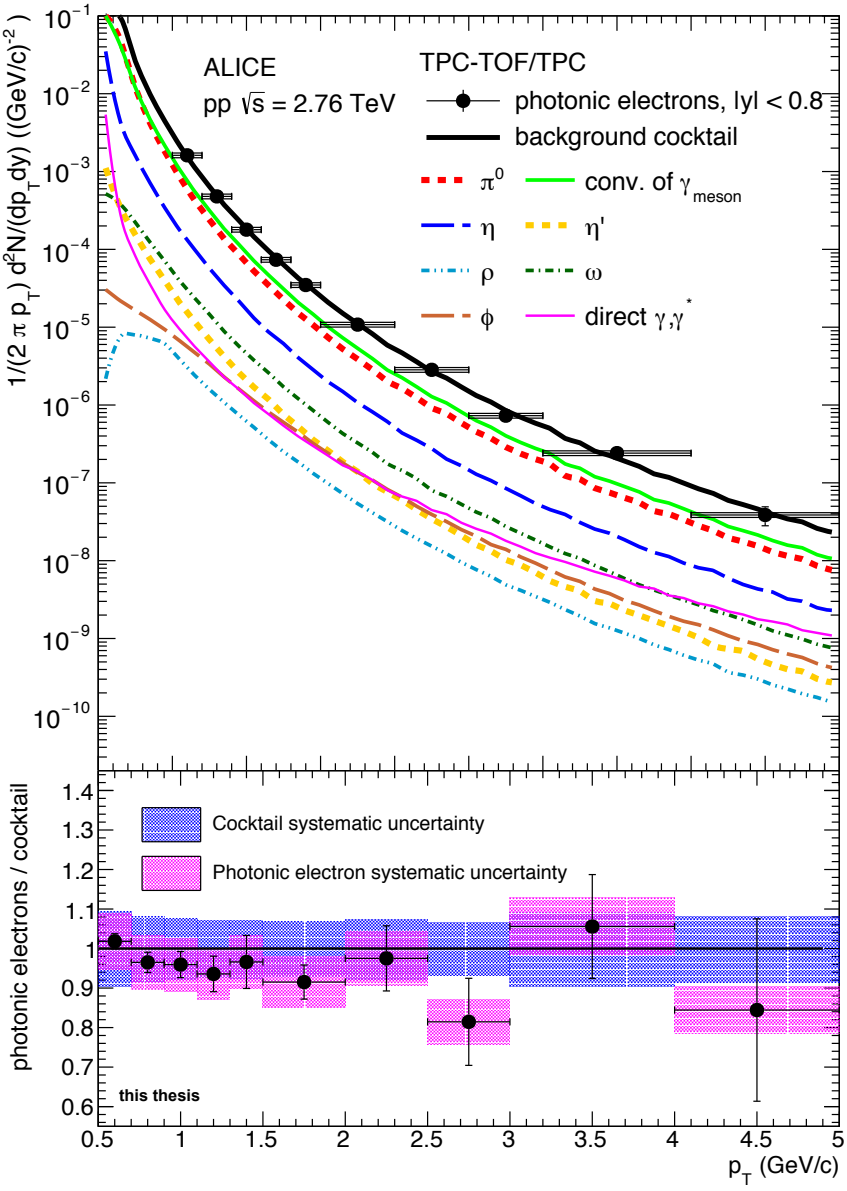

Figure 6.29: The spectrum of electrons from photonic sources corrected for efficiencies using the enhanced MC sample (LHC12a9) compared to the cocktail components from conversions or decays of light particles. The systematic uncertainties of the photonic spectrum were evaluated varying the track selection criteria linked to the selection of electrons from photonic sources.

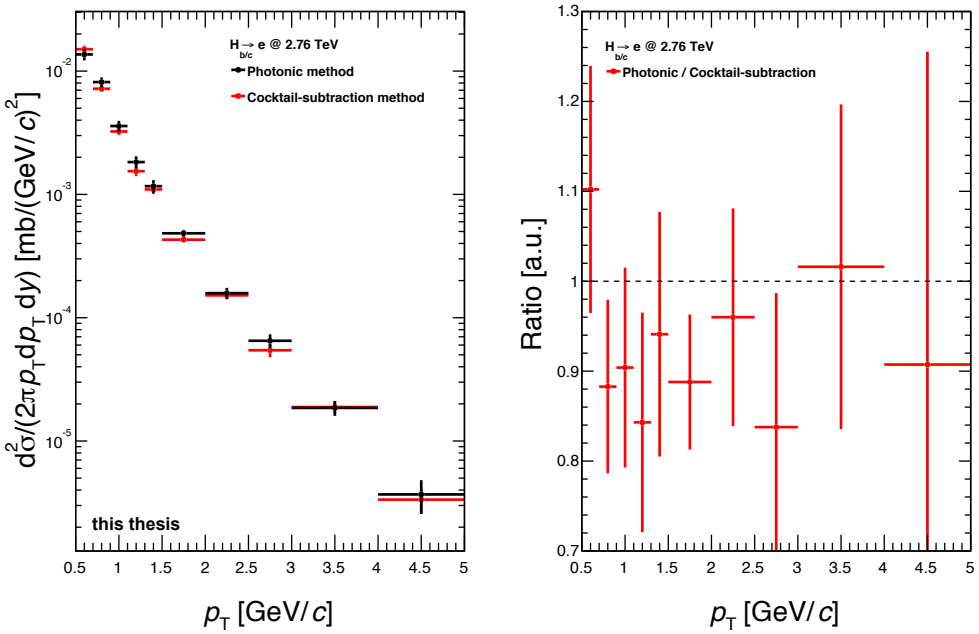

Figure 6.30: Comparison of the cross-section for electrons from heavy-flavour hadron decays evaluated using the photonic method or the cocktail-subtraction method within the current ALICE analysis framework.

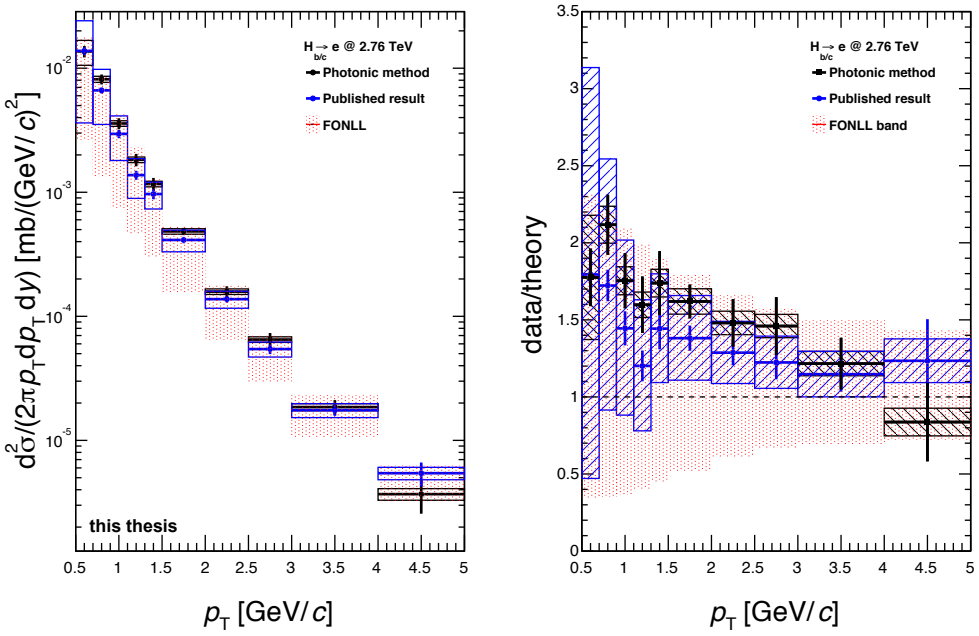

Figure 6.31: Comparison of the production cross-section measured with the photonic method and the published one with the pQCD calculations from FONLL.

7. Conclusions

In the last section, the p_{T}-differential production cross-section for electrons from semi-electronic decays of beauty and charm hadrons was measured with ALICE in the transverse momentum range $0.5\,\mathrm{GeV}/c < p_{\mathrm{T}} < 5.0\,\mathrm{GeV}/c$ at mid-rapidity in pp collisions at $\sqrt{s} = 2.76\,\mathrm{TeV}$. This result was obtained using the photonic method to estimate the electrons from the dominate background sources. FONLL pQCD calculations are in good agreement with this measurement and the published cross-section measurement is compatible within uncertainties.

Even though the systematic uncertainties on this cross-section were reduced by more than a factor of 3 over most of the transverse momentum region, the new result cannot be used to restrict the range of the parameter values used for the FONLL calculations because the statistical uncertainties had not been reduced. To continue with the attempt of using ratios of differential cross sections at different centre-of-mass energies, we have to wait for the cross-sections measured in pp collisions at $\sqrt{s} = 13\,\mathrm{TeV}$, which have much larger statistics than the measurements at $\sqrt{s} = 2.76\,\mathrm{TeV}$ and combine these with measurements at $\sqrt{s} = 7\,\mathrm{TeV}$. Another possibility would be to use measurements of muons from decays of heavy-flavour hadron decays at forward or backward rapidity because the FONLL calculations in this kinematic region are more sensitive to the parton distribution functions (PDFs) than at mid-rapidity [19].

The new result for the cross-section of electrons from heavy-flavour hadron decays at $\sqrt{s} = 2.76\,\mathrm{TeV}$ was used to calculate the nuclear modification factor

$$R_{\mathrm{AA}} = \frac{\frac{\mathrm{d}N_{\mathrm{AA}}}{\mathrm{d}p_{\mathrm{T}}}}{\langle T_{\mathrm{AA}} \rangle \frac{\mathrm{d}\sigma_{\mathrm{pp}}}{\mathrm{d}p_{\mathrm{T}}}} \tag{7.1}$$

It is used to quantify the energy loss of the heavy quarks while travelling through the Quark-Gluon-Plasma. Here, $\frac{\mathrm{d}N_{\mathrm{AA}}}{\mathrm{d}p_{\mathrm{T}}}$ and $\frac{\mathrm{d}\sigma_{\mathrm{pp}}}{\mathrm{d}p_{\mathrm{T}}}$ are the differential yield measured in Pb–Pb and the differential cross-sections measured in pp collisions, respectively. The average nuclear

overlap function, T_{AA}, is proportional to the average number of binary nucleon-nucleon collisions in nucleus-nucleus collisions and is estimated using a Glauber model calculation [39, 40]. The R_{AA} is unity when no nuclear effects are present by construction. Figure 7.1 shows the R_{AA} for the 10% most central collisions in Pb–Pb collisions at $\sqrt{s_{\mathrm{NN}}} = 2.76\,\mathrm{TeV}$ and demonstrates that the new pp reference described in the previous chapter improves the precision at low p_{T}. Further information about the measurement in Pb–Pb collisions and the R_{AA} can be found in [31] and [41].

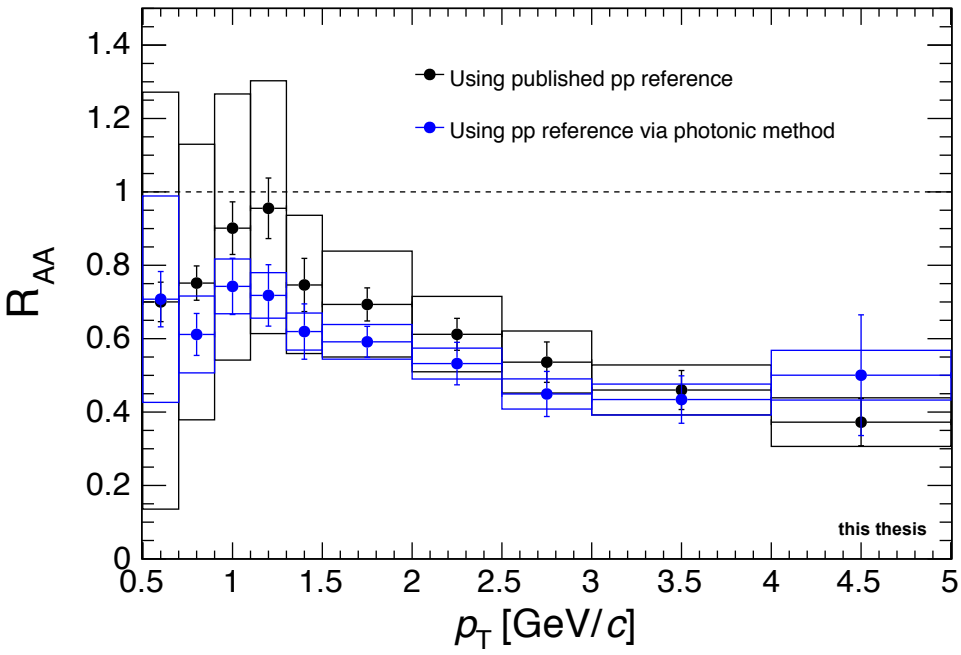

Figure 7.1: The nuclear modification factor R_{AA} using the measurement of the cross-section for electrons from semi-electronic decays of beauty and charm hadrons in the 10% most central Pb–Pb collisions and pp collisions at $\sqrt{s_{\mathrm{NN}}} = 2.76\,\mathrm{TeV}$. The published result using the cocktail subtraction method was used as pp reference for the black points and the new reference cross-section using the method of tagging photonic electrons was used for the blue ones. The cross-section in Pb–Pb collision was evaluated using the method of tagging photonic electrons, too.

The nuclear modification factor was compared to theoretical models that include heavy-quark interactions with the medium in Figure 7.2, which shows the preliminary result. Note that these models not only differ in the theoretical realisation of the medium properties, its dynamics and in the implementations related to the hadronisation and hadron-hadron interactions in the late stages of the heavy-ion collision. But also in the heavy-quark cross-section used as the input to the calculations (PYTHIA [21, 22], FONLL [2, 3] and POWHEG

[14]) in some cases. Several models provide a good description of the R_{AA} in 10% most central collision events. More information about the model can be found in [41].

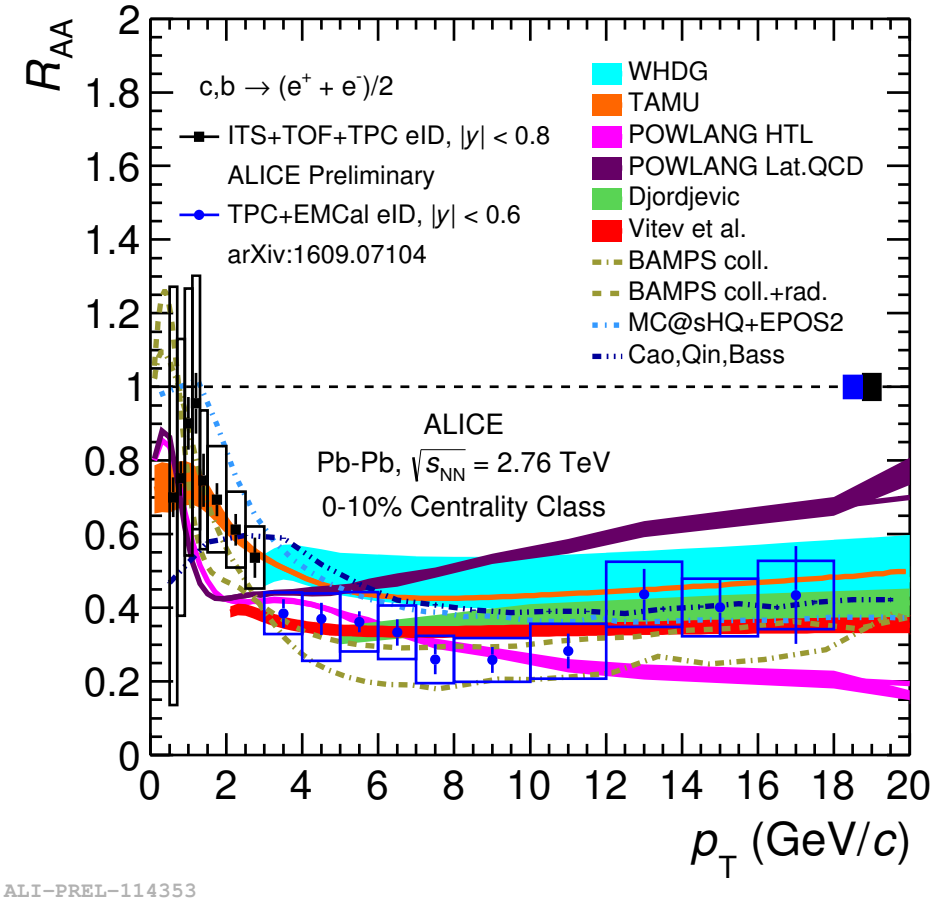

Figure 7.2: The R_{AA} of electrons from heavy-flavour hadron decays measured in 10% most central Pb–Pb collisions at $\sqrt{s_{\mathrm{NN}}} = 2.76\,\mathrm{TeV}$ compared to various theoretical calculations.

A. Appendix

A.1. FONLL

Table A.1: Overview of the different parameters used for the FONLL webform

Parameter	Value	Description
Collider	LHC (pp, 2.75 / 7 / 13 TeV)	Collider and energy
PDFs	CTEQ6.6	PDF set
Perturbative order	FONLL	Perturbative order of calculation
Quark	charm / bottom	Type of heavy-quark
Final state	D^0, D^+, D^{*+}	For D meson references
Hadron state	B meson or 0.7 D^0 + 0.3 D^+	Only for the semi-electronic decay references
Further decay	B (to D) / D to electron	Only for the semi-electronic decay references
Cross-section type	$\frac{d\sigma}{dp_T}$	For D meson references
p_T^{min}	0	Minimum transverse momentum
p_T^{max}	25	Maximum transverse momentum
y^{min}	-0.5	Minimum rapidity
y^{max}	0.5	Maximum rapidity
n_{points}	251	Number of point calculated with FONLL
BR(D→l)	0.103	Branching ratio for semi-leptonic decay of D hadrons
BR(B→l)	0.1086	Branching ratio for direct semi-leptonic decay of B hadrons
BR(B→D→l)	0.096	Branching ratio for semi-leptonic decay of B hadrons via D hadrons
FF(D^0)	0.56	Fragmentation Fraction for D^0
FF(D^+)	0.23	Fragmentation Fraction for D^+
FF(D^{*+})	0.23	Fragmentation Fraction for D^{*+}

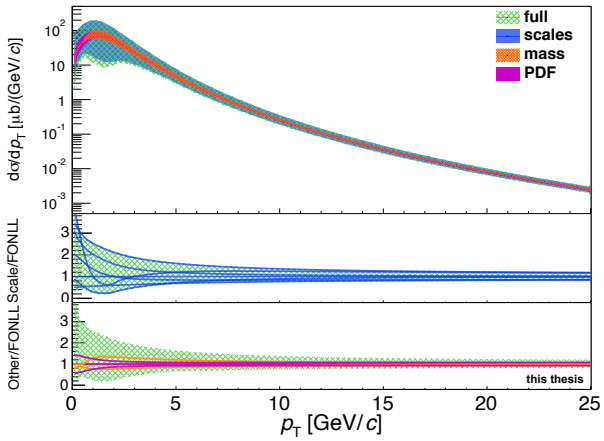

(a) FONLL band and single curves for D^0

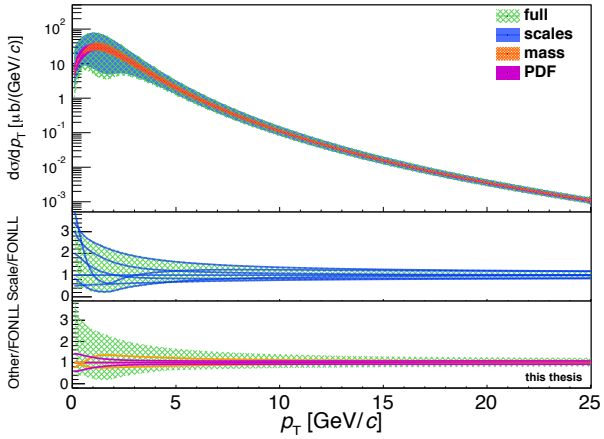

(b) FONLL band and single curves for D^+

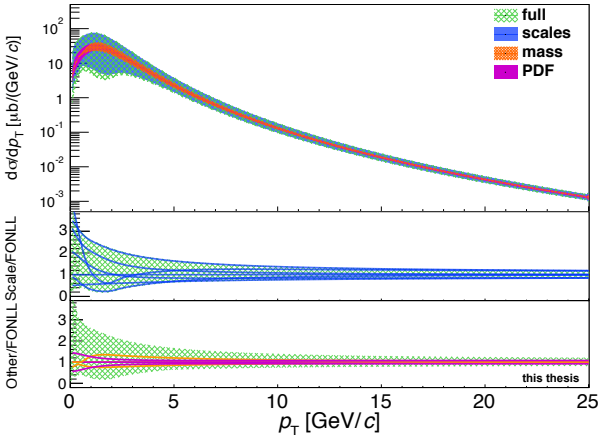

(c) FONLL band and single curves for D^{*+}

Figure A.1: The calculations for the p_T-differential cross-section of D^0, D^+ and D^{*+} at $\sqrt{s} = 2.76\,\text{TeV}$ obtained within the FONLL framework. The uncertainties introduced by the scales, the quark mass and the PDFs are shown as blue, orange and violet band, respectively. The full uncertainty band is shown in green. The two pads below show the ratios of the scale and mass variation, as well as, the curves belonging to the maximum and minimum deviations caused by the PDF uncertainties to the central value of FONLL.

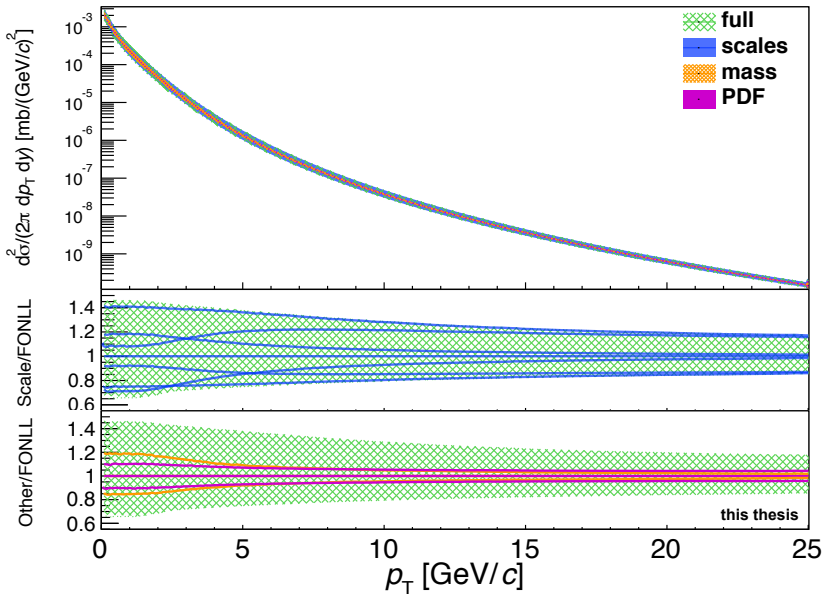

(a) FONLL band and single curves for the semi-electronic decay of beauty hadrons

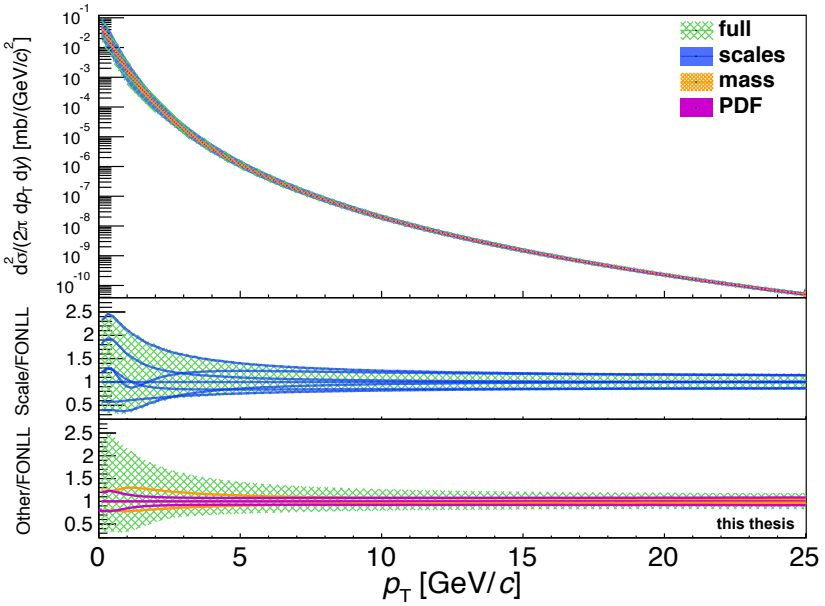

(b) FONLL band and single curves for the semi-electronic decay of charm hadrons

Figure A.2: The calculations for the p_T-differential cross-section of electrons coming from the semi-electronic decay of beauty and charm hadrons at $\sqrt{s} = 2.76\,\text{TeV}$ obtained within the FONLL framework.The uncertainties introduced by the scales, the quark mass and the PDFs are shown as blue, orange and violet band, respectively. The full uncertainty band is shown in green. The two pads below show the ratios of the scale and mass variation, as well as, the curves belonging to the maximum and minimum deviations caused by the PDF uncertainties to the central value of FONLL.

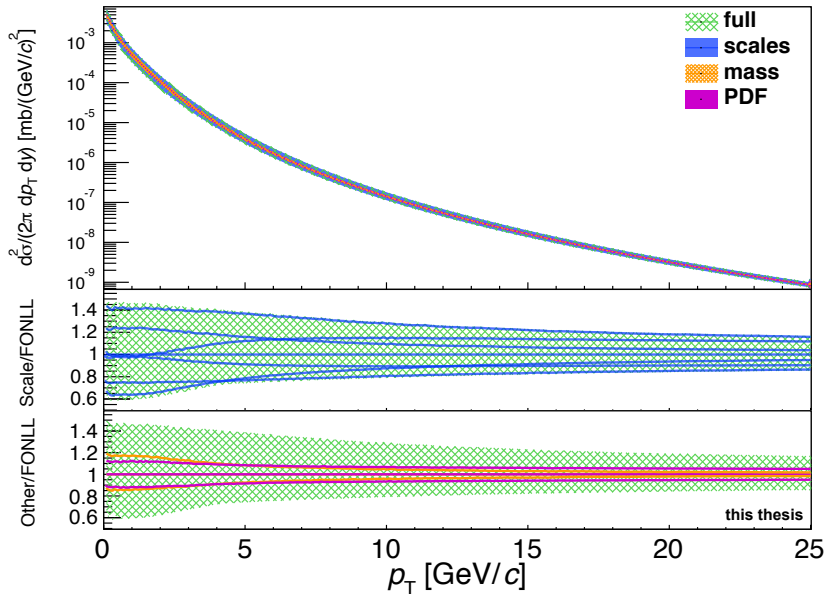

(a) FONLL band and single curves for the semi-electronic decay of beauty hadrons

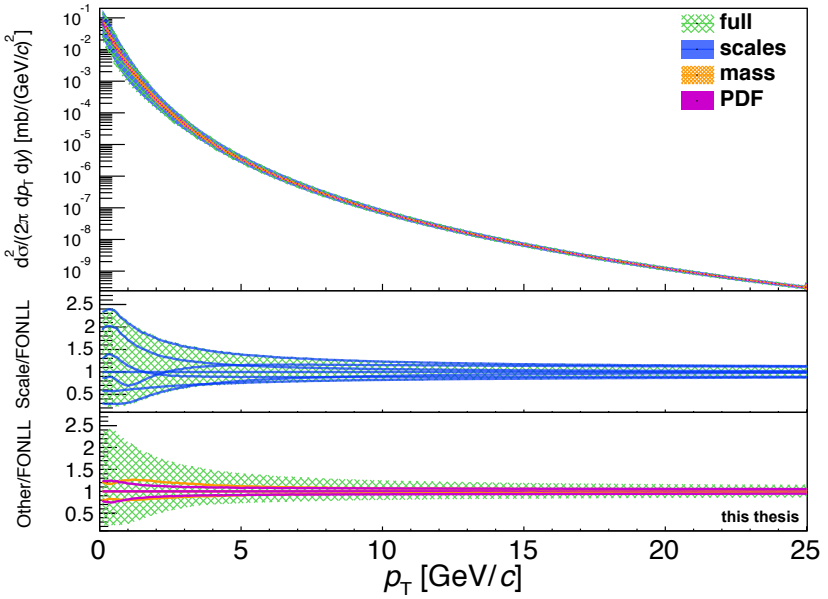

(b) FONLL band and single curves for the semi-electronic decay of charm hadrons

Figure A.3: The calculations for the p_T-differential cross-section of electrons coming from the semi-electronic decay of beauty and charm hadrons at $\sqrt{s} = 7$ TeV obtained within the FONLL framework. The uncertainties introduced by the scales, the quark mass and the PDFs are shown as blue, orange and violet band, respectively. The full uncertainty band is shown in green. The two pads below show the ratios of the scale and mass variation, as well as, the curves belonging to the maximum and minimum deviations caused by the PDF uncertainties to the central value of FONLL.

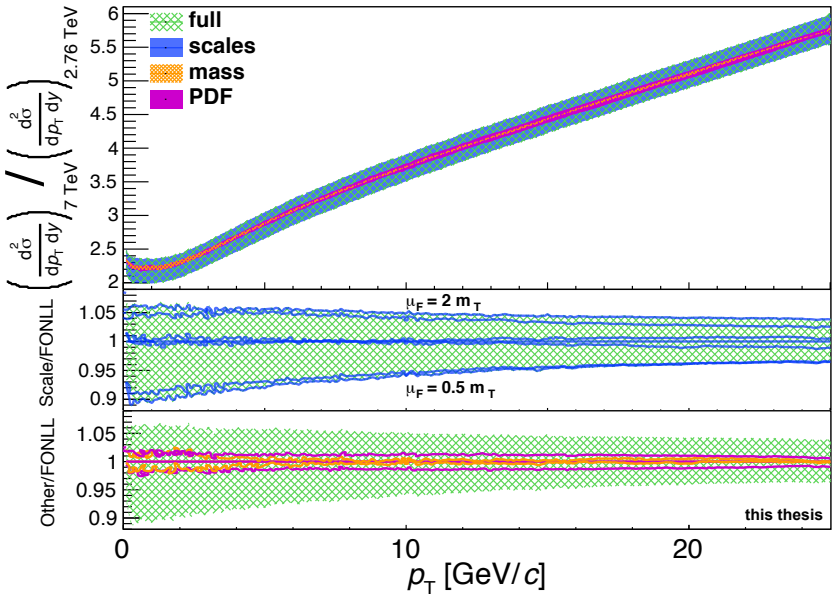

(a) FONLL band and single for the semi-electronic decay of beauty hadrons

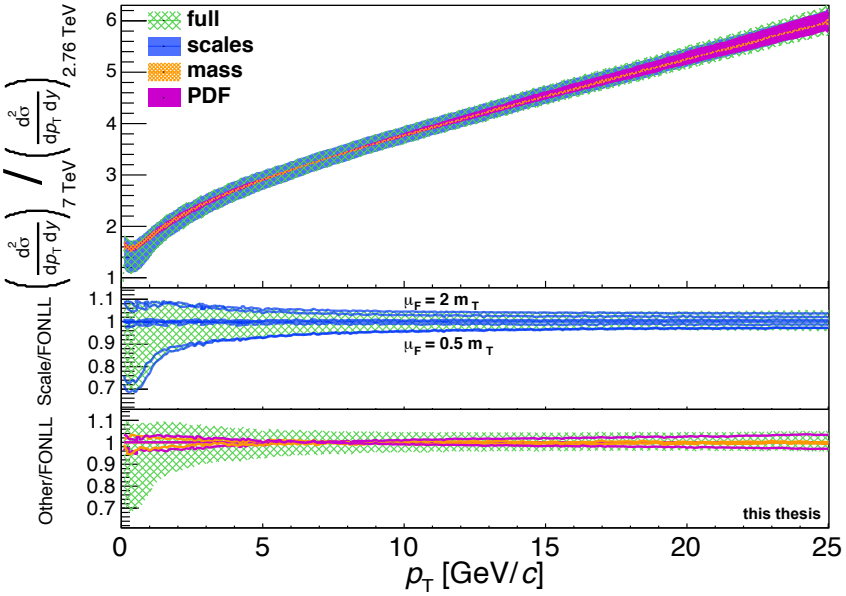

(b) FONLL band and for the semi-electronic decay of charm hadrons

Figure A.4: The ratio of the calculations for the p_T-differential cross-section of electrons from semi-electronic decays of beauty and charm hadrons at $\sqrt{s} = 7\,\text{TeV}$ and $\sqrt{s} = 2.76\,\text{TeV}$ obtained within the FONLL framework. The uncertainties introduced by the scales, the quark mass and the PDFs are shown as blue, orange and violet band, respectively. The full uncertainty band is shown in green. The two pads below show the ratios of the scale and mass variation, as well as, the curves belonging to the maximum and minimum deviations caused by the PDF uncertainties to the central value of FONLL.

A.2. POWHEG

Table A.2: Overview of the different parameters of POWHEG-Box simulations

Parameter	Value	Description
Number of events	150000	Number of events generated per split
Number of splits	1000	Number of separate calls of POWHEG-BOX per GRID job
ih1 / ih2	1	Type of colliding particle (here: proton)
lhans1 / lhans2	10550	PDF set for hadron 1 or 2, LHA numbering (here: CTEQ6.6)
ebeam1 / ebeam 2	1380/3500	Energy of beam 1 or 2
qmass	1.3/1.5/1.7	Mass of heavy-quark in GeV
facscfact	0.5/1/2	Factorization scale factor: $\mu_{\text{fact}} = \mu_{\text{ref}} \cdot$ facscfact
renscfact	0.5/1/2	Renormalization scale factor: $\mu_{\text{fact}} = \mu_{\text{ref}} \cdot$ renscfact
use-old-grid	1	Use old grid if file pwggrids.dat is present
use-old-ubound	1	Use norm of upper bounding function stored in pwgubound.dat, if present
ncall1	50000	Number of calls for initializing the integration grid
itmx1	5	Number of iterations for initializing the integration grid
ncall2	100000	Number of calls for computing the integral and finding upper bound
itmx2	5	Number of iterations for computing the integral and finding upper bound
foldcsi	5	Number of folds on x integration
foldy	5	Number of folds on y integration
foldphi	1	Number of folds on phi integration
nubound	500000	Number of bbarra calls to setup norm of upper bounding function
iymax	1	<= 10, normalization of upper bounding function in x $\log(m_{qq}^2)$
ixmax	1	<= 10, normalization of upper bounding function in y $\log(m_{qq}^2)$
xupbound	2	Increase upper bound for radiation generation

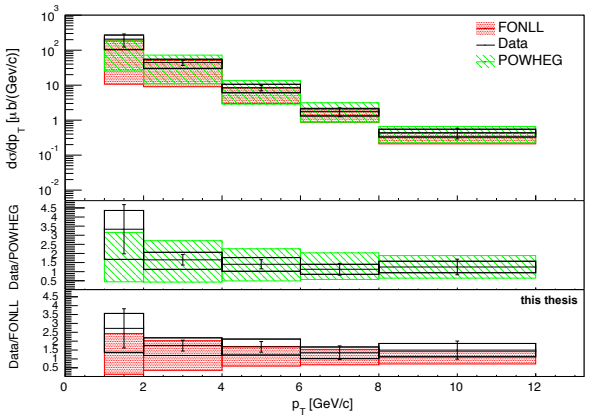

(a) p_{T}-differential cross-section for D^0

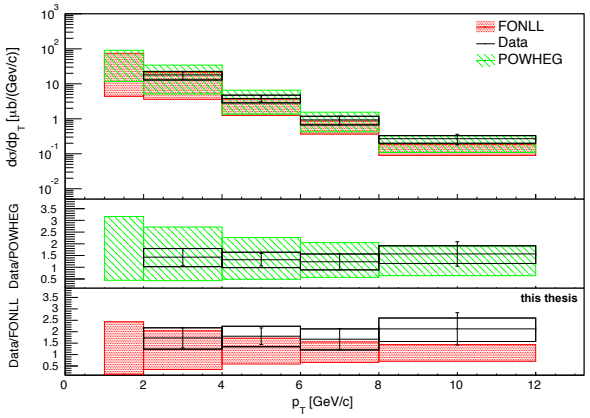

(b) p_{T}-differential cross-section for D^+

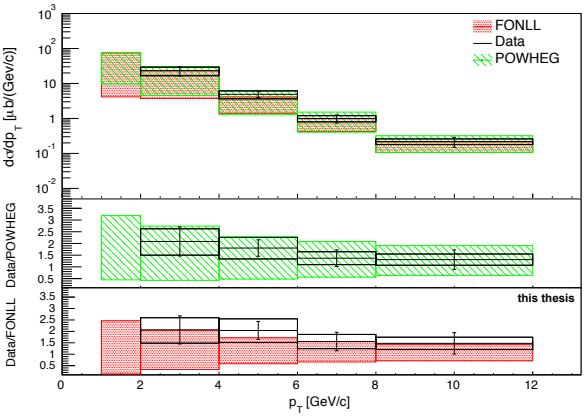

(c) p_{T}-differential cross-section for D^{*+}

Figure A.5: Comparison of the measured p_{T}-differential cross-section of D^0, D^+ and D^{*+} production at $\sqrt{s} = 2.76$ TeV to FONLL calculations (red) and POWHEG simulations (green). The two panels below show the ratios of data to the central value of POWHEG and FONLL. In all panels, the statistical and systemtical uncertainties are represented by the bars and boxes, respectively.

A.3. Estimate

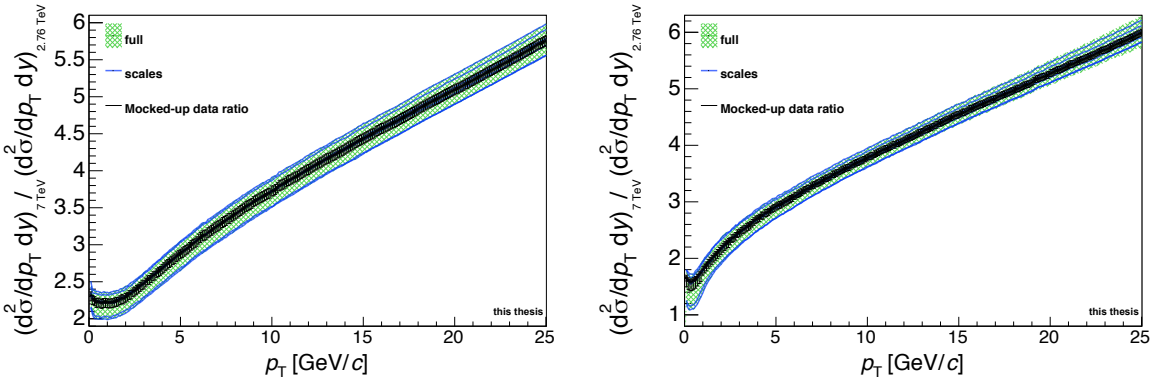

(a) Semi-electronic decay of beauty hadrons

(b) Semi-electronic decay of charm hadrons

Figure A.6: The ratio of the p_T-differential cross-sections at $\sqrt{s} = 7$ TeV and 2.76 TeV evaluated using the FONLL webpage. Here the mocked-up data is assumed to lie at the centre of the FONLL reference, which leads to rather small asymmetric uncertainties allowed to be still decisive.

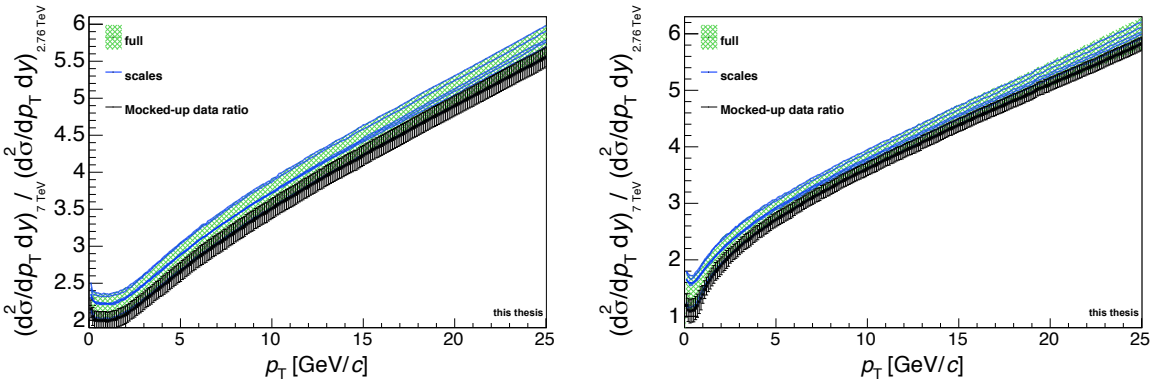

(a) Semi-electronic decay of beauty hadrons

(b) Semi-electronic decay of charm hadrons

Figure A.7: The ratio of the p_T-differential cross-sections at $\sqrt{s} = 7$ TeV and 2.76 TeV evaluated using the FONLL webpage. Here the mocked-up data is assumed to lie at the lower edge of the FONLL reference, which leads to a little bit larger uncertainties allowed to be still decisive.

A.4. Re-analysis of electrons from heavy-flavour decays

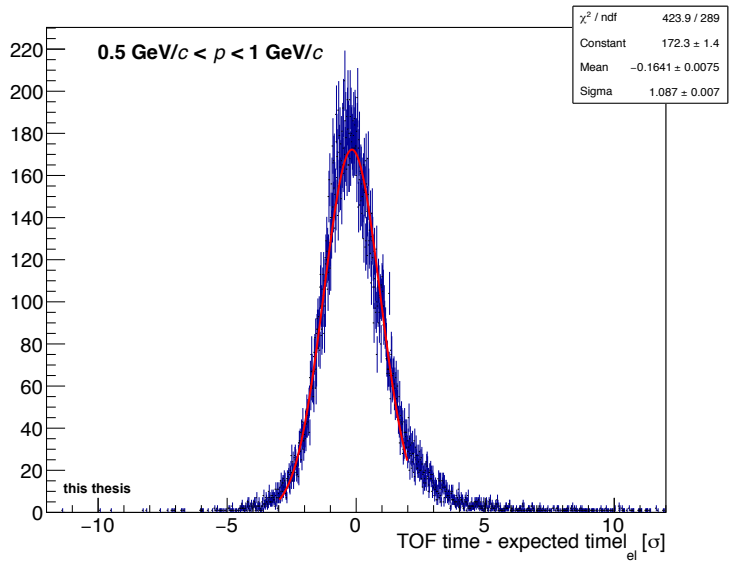

(a) SPD kAny

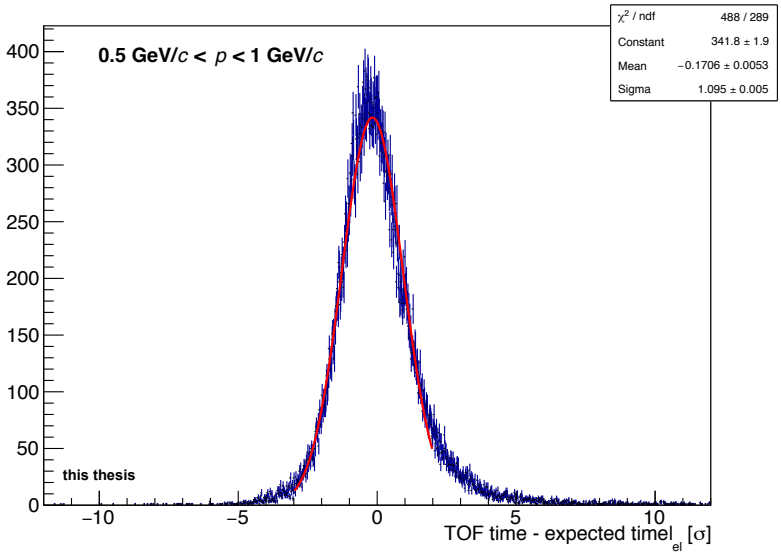

(b) Without SPD requirement

Figure A.8: TOF slice $0.5\,\mathrm{GeV}/c < p < 1.0\,\mathrm{GeV}/c$ after all cuts for data with [panel (a)] and without [panel (b)] SPD requirement.

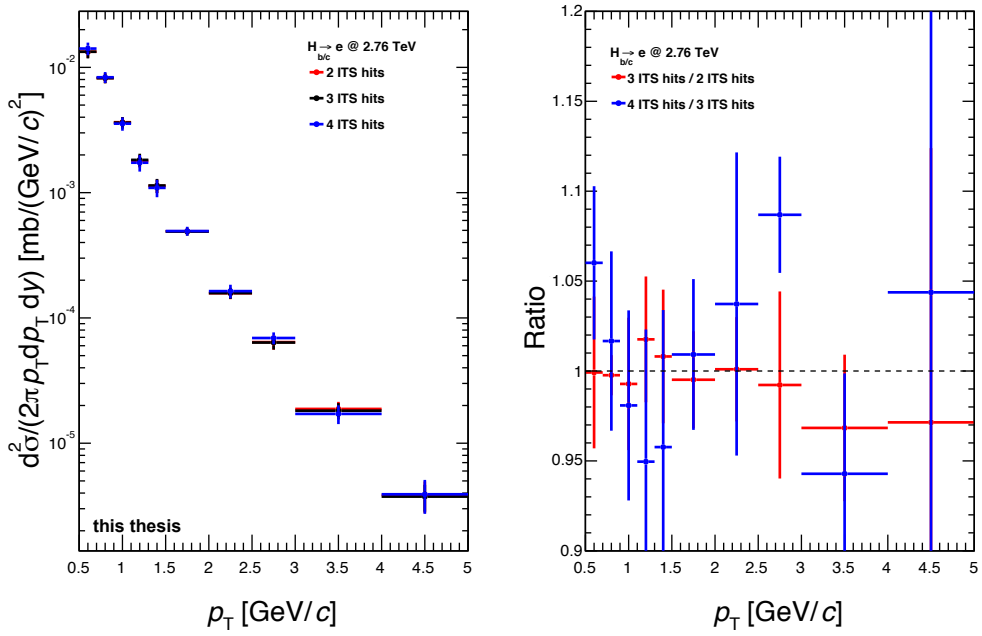

Figure A.9: The variation of ITS hits for electron candidate tracks.

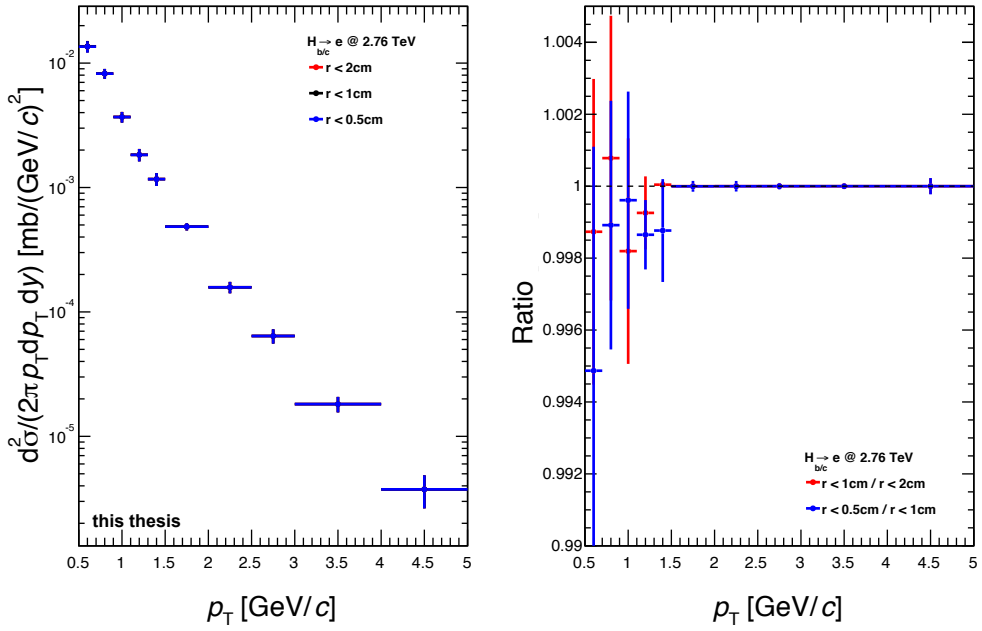

(a) Radial DCA

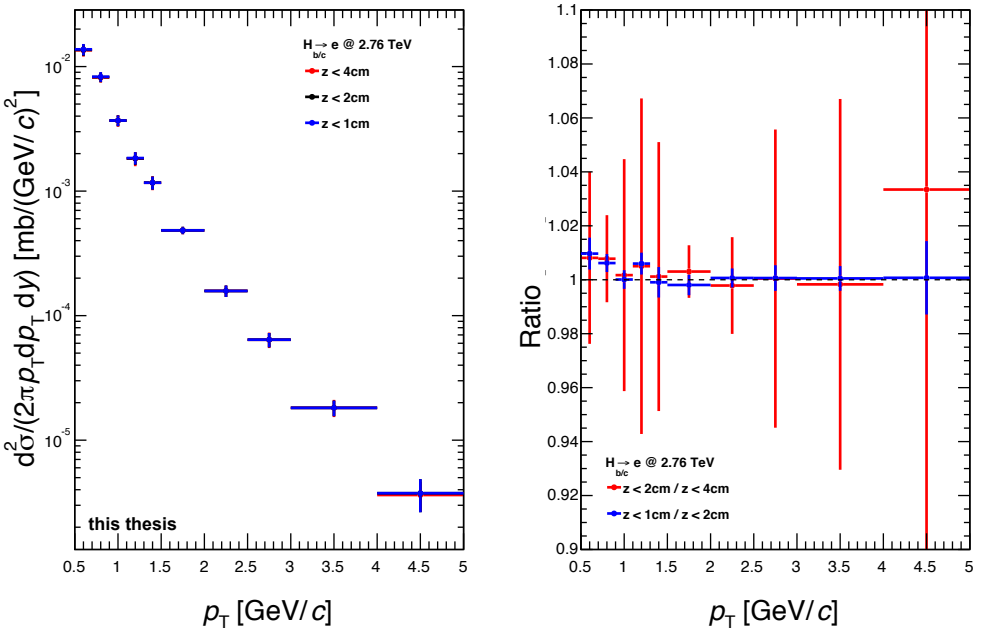

(b) DCA in z direction

Figure A.10: The variation of the maximum allowed distance of closest approach (DCA) for electron candidate tracks. The radial DCA is shown in panel (a) and panel (b) displays the DCA along the beam direction.

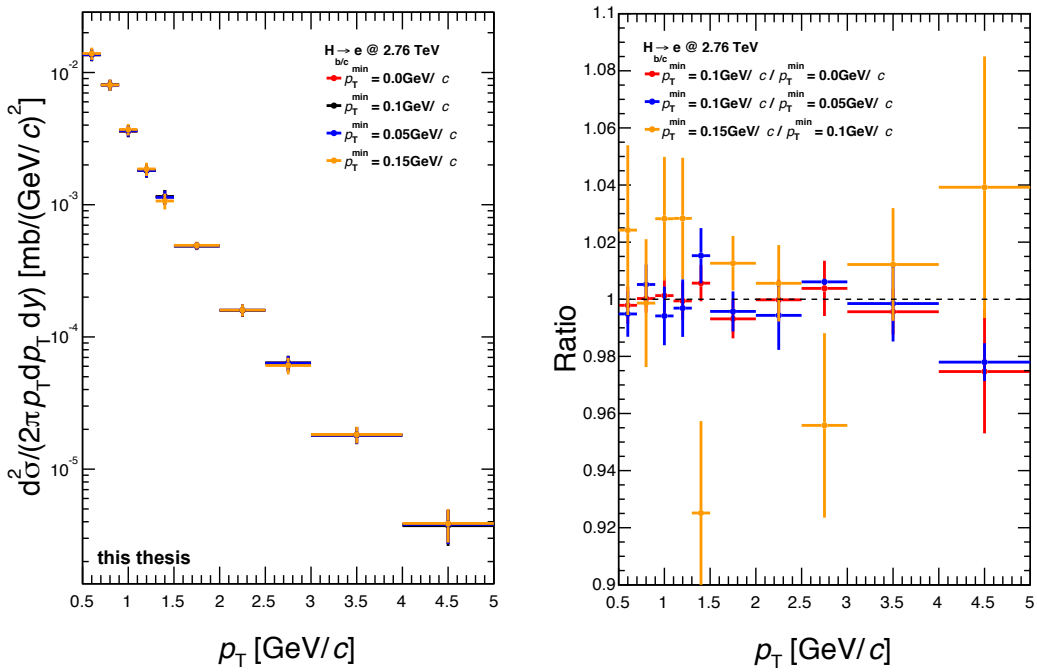

Figure A.11: The variation of the requirement on the minimum p_T on associated electron tracks.

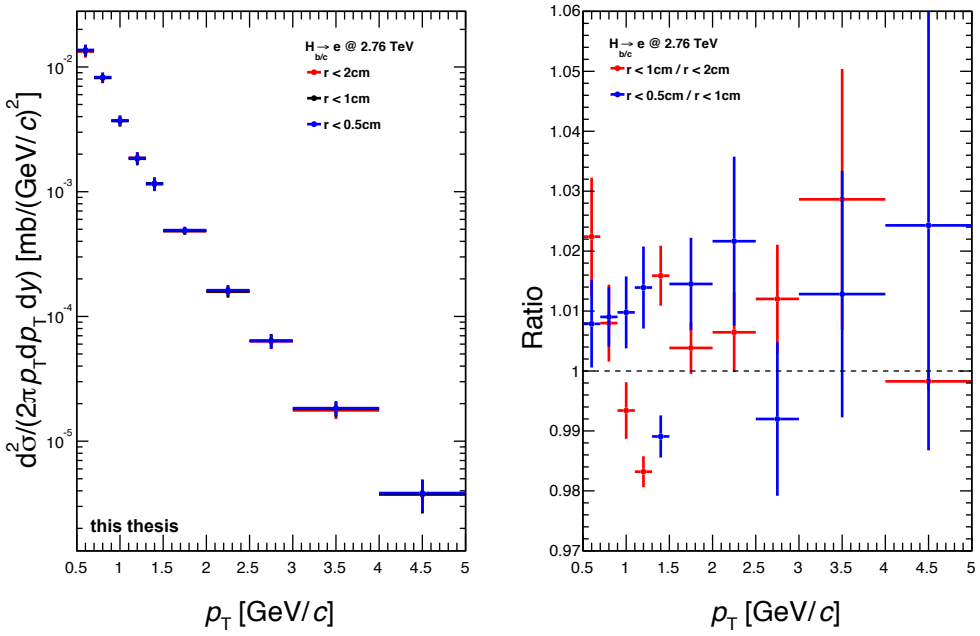

(a) Radial DCA

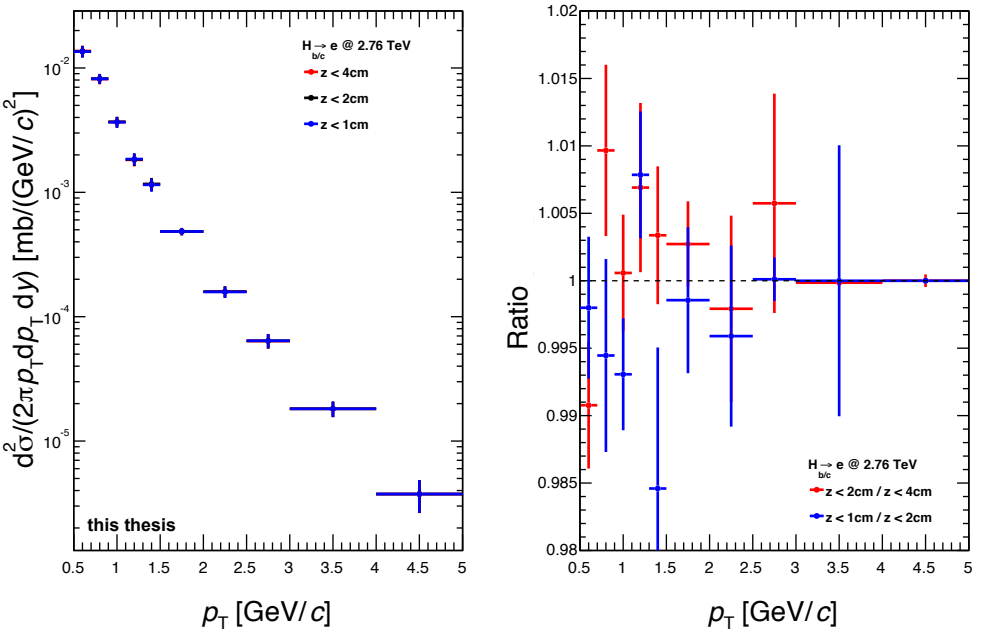

(b) DCA in z direction

Figure A.12: The variation of the maximum allowed distance of closest approach (DCA) for associated electron tracks. The radial DCA is shown in panel (a) and panel (b) displays the DCA along the beam direction.

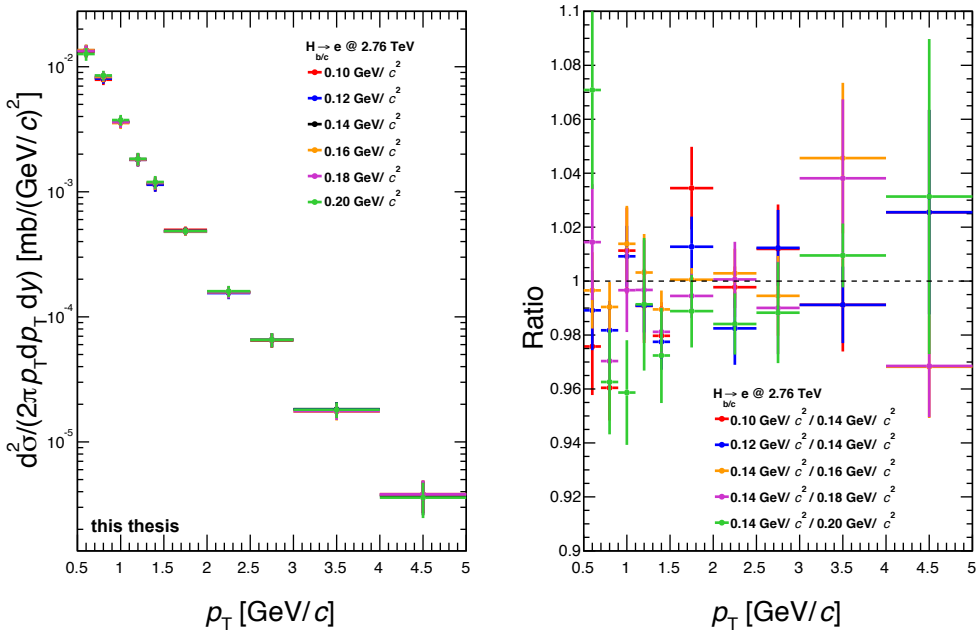

Figure A.13: The variation of the requirement on the maximum m_{pair} on the associated electron tracks.

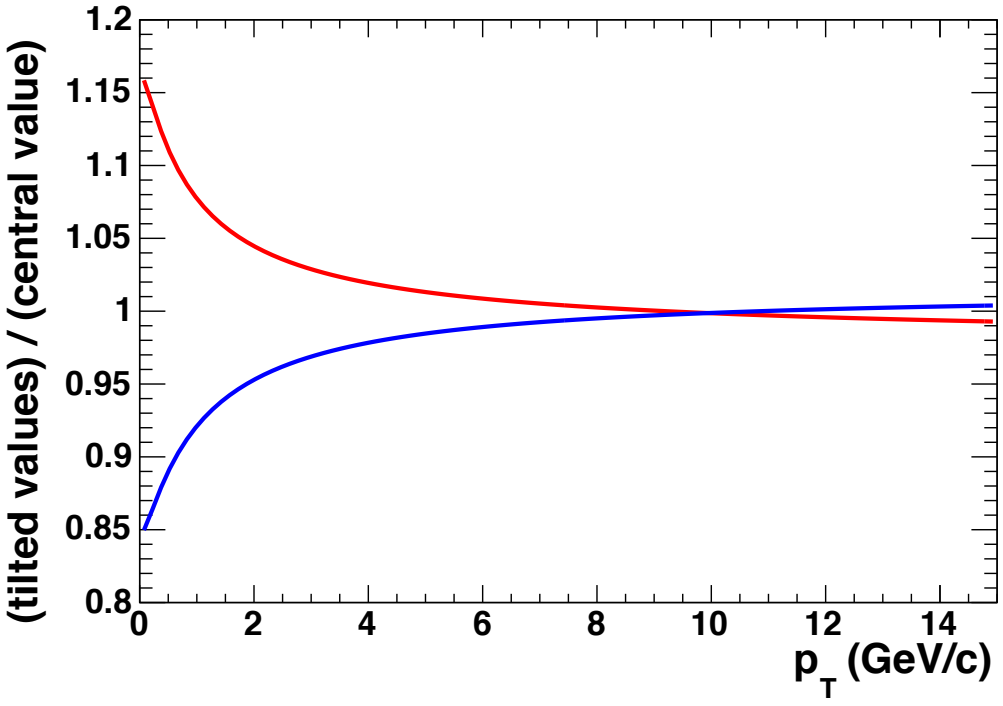

Figure A.14: Comparison of the tilted vales of the π^0-spectrum to the central values.

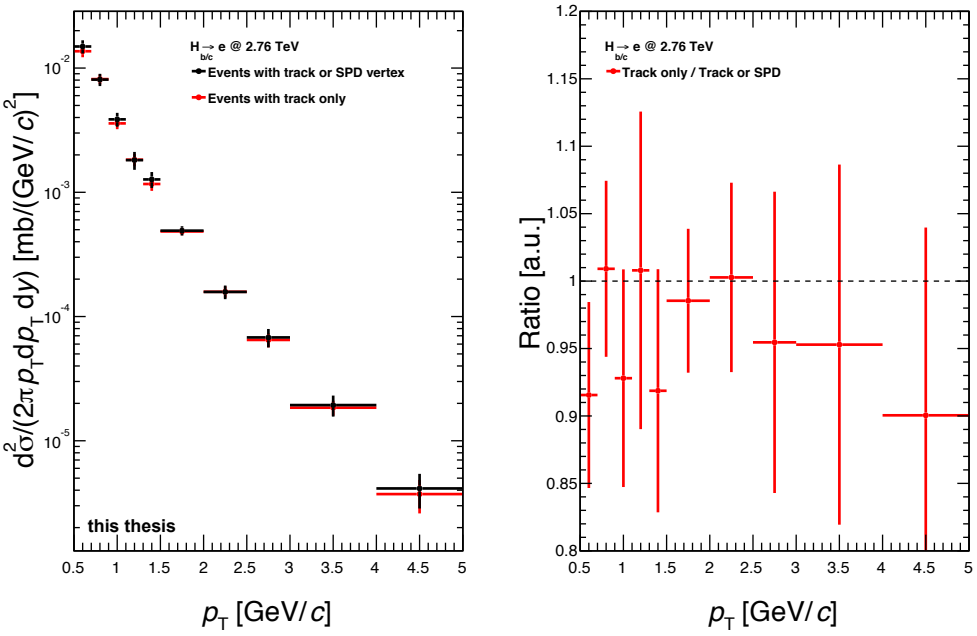

Figure A.15: The cross-section for electrons from heavy-flavour hadron decays using only events with primary vertex reconstructed with long tracks or events with primary vertex from long tracks and SPD.

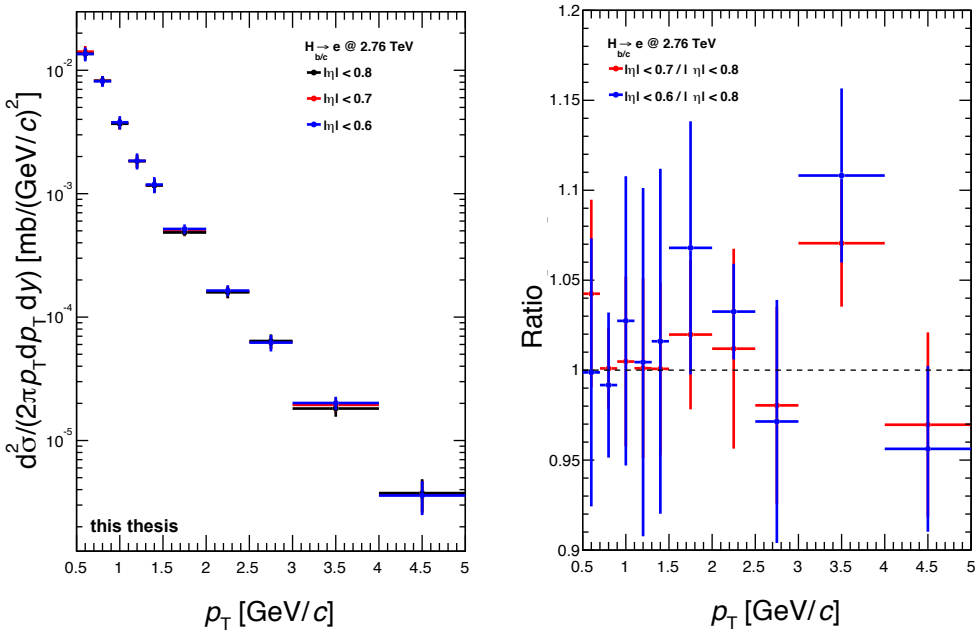

Figure A.16: The variation of the η-range used in this analysis.

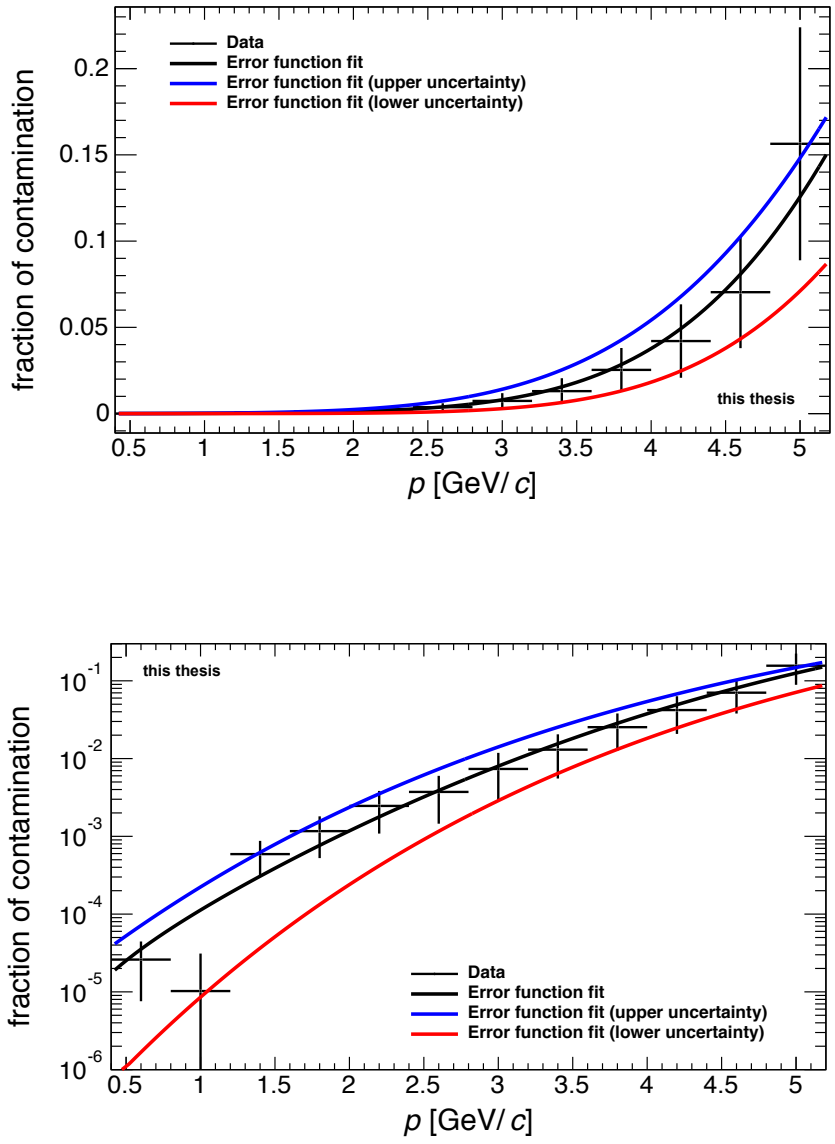

Figure A.17: The hadron contamination shown with the Error function fitted to the central values as well as the fits to the upper and lower edges of the statistical uncertainties.

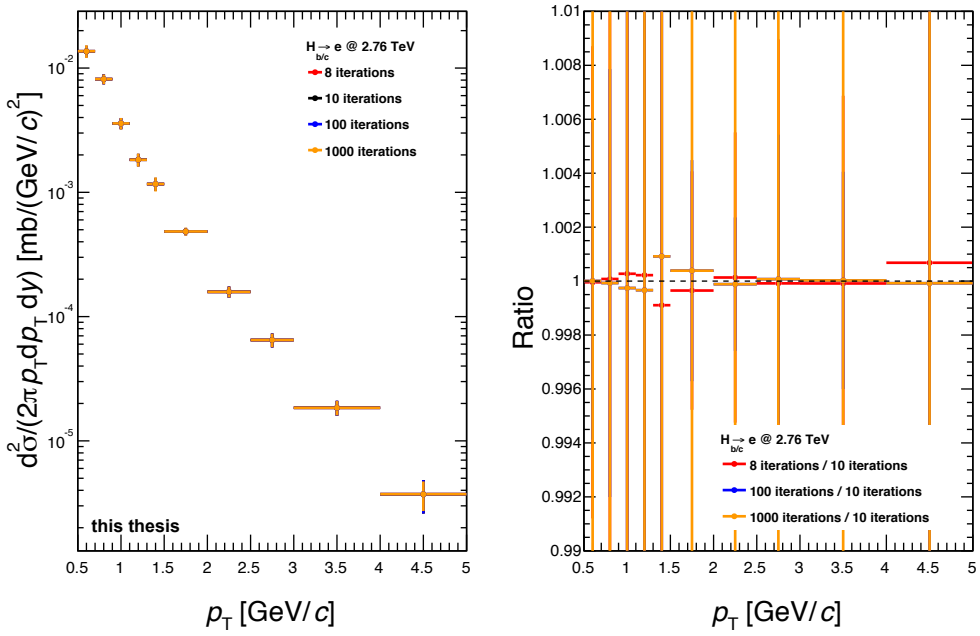

Figure A.18: The variation for the number of iterations performed in the unfolding procedure.

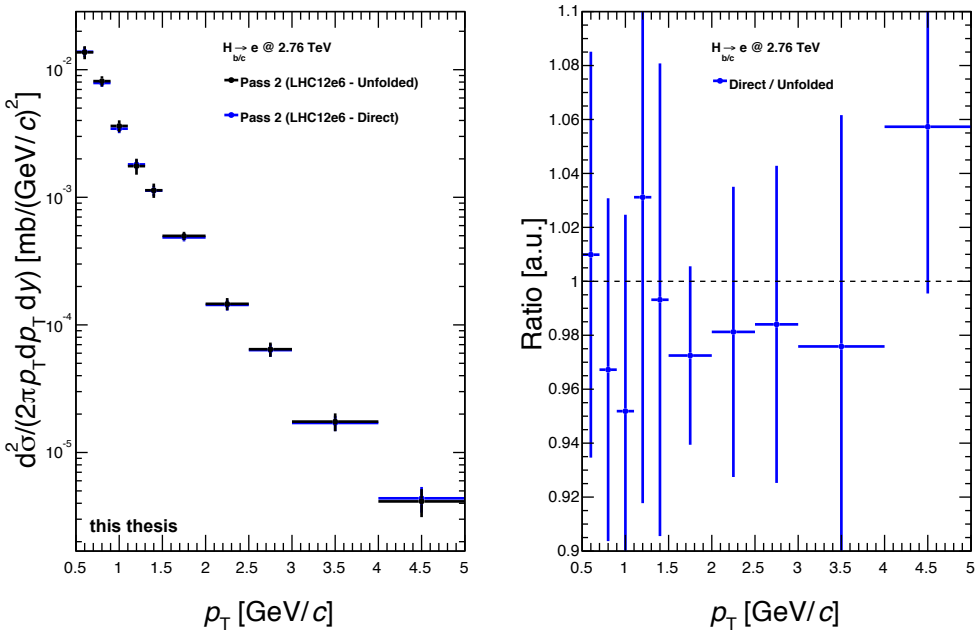

Figure A.19: Comparison of the two different methods used for correcting for acceptance and efficiency.

List of Figures

List of Tables

Bibliography

[1] R. Averbeck. "Heavy-flavor production in heavy-ion collisions and implications for the properties of hot QCD matter". In: *Prog. Part. Nucl. Phys.* 70 (2013), pp. 159–209. DOI: 10.1016/j.ppnp.2013.01.001. arXiv: 1505.03828 [nucl-ex].

[2] Matteo Cacciari, Mario Greco, and Paolo Nason. "The p_T spectrum in heavy flavor hadroproduction". In: *JHEP* 05 (1998), p. 007. DOI: 10.1088/1126-6708/1998/05/007. arXiv: hep-ph/9803400 [hep-ph].

[3] Matteo Cacciari et al. "Theoretical predictions for charm and bottom production at the LHC". In: *JHEP* 10 (2012), p. 137. DOI: 10.1007/JHEP10(2012)137. arXiv: 1205.6344 [hep-ph].

[4] B. A. Kniehl et al. "Hadroproduction of D and B mesons in a massive VFNS". In: *AIP Conf. Proc.* 792 (2005). [,867(2005)], pp. 867–870. DOI: 10.1063/1.2122174. arXiv: hep-ph/0507068 [hep-ph].

[5] B. A. Kniehl et al. "Inclusive Charmed-Meson Production at the CERN LHC". In: *Eur. Phys. J.* C72 (2012), p. 2082. DOI: 10.1140/epjc/s10052-012-2082-2. arXiv: 1202.0439 [hep-ph].

[6] Betty Abelev et al. "Measurement of charm production at central rapidity in proton-proton collisions at $\sqrt{s} = 2.76$ TeV". In: *JHEP* 07 (2012), p. 191. DOI: 10.1007/JHEP07(2012)191. arXiv: 1205.4007 [hep-ex].

[7] Rafal Maciula and Antoni Szczurek. "Open charm production at the LHC - k_t-factorization approach". In: *Phys. Rev.* D87.9 (2013), p. 094022. DOI: 10.1103/PhysRevD.87.094022. arXiv: 1301.3033 [hep-ph].

[8] Betty Bezverkhny Abelev et al. "Beauty production in pp collisions at $\sqrt{s}$ = 2.76 TeV measured via semi-electronic decays". In: *Phys. Lett.* B738 (2014), pp. 97–108. DOI: 10.1016/j.physletb.2014.09.026. arXiv: 1405.4144 [nucl-ex].

[9] J. Schukraft. "Heavy-ion physics with the ALICE experiment at the CERN Large Hadron Collider". In: *Royal Society of London Philosophical Transactions Series A* 370 (Feb. 2012), pp. 917–932. DOI: 10.1098/rsta.2011.0469. arXiv: 1109.4291 [hep-ex].

[10] The ALICE Collaboration. "Performance of the ALICE Experiment at the CERN LHC". In: *ArXiv e-prints* (Feb. 2014). arXiv: 1402.4476 [nucl-ex].

[11] K. Aamodt et al. "The ALICE experiment at the CERN LHC". In: *JINST* 3 (2008), S08002. DOI: 10.1088/1748-0221/3/08/S08002.

[12] Betty Abelev et al. "Measurement of electrons from semileptonic heavy-flavour hadron decays in pp collisions at $\sqrt{s}$ = 7 TeV". In: *Phys. Rev.* D86 (2012), p. 112007. DOI: 10.1103/PhysRevD.86.112007. arXiv: 1205.5423 [hep-ex].

[13] Betty Bezverkhny Abelev et al. "Measurement of electrons from semileptonic heavy-flavor hadron decays in pp collisions at $\sqrt{s} = 2.76$ TeV". In: *Phys. Rev.* D91.1 (2015), p. 012001. DOI: 10.1103/PhysRevD.91.012001. arXiv: 1405.4117 [nucl-ex].

[14] Stefano Frixione, Paolo Nason, and Giovanni Ridolfi. "A Positive-weight next-to-leading-order Monte Carlo for heavy flavour hadroproduction". In: *JHEP* 09 (2007), p. 126. DOI: 10.1088/1126-6708/2007/09/126. arXiv: 0707.3088 [hep-ph].

[15] M. Klasen et al. "NLO Monte Carlo predictions for heavy-quark production at the LHC: pp collisions in ALICE". In: *JHEP* 08 (2014), p. 109. DOI: 10.1007/JHEP08(2014)109. arXiv: 1405.3083 [hep-ph].

[16] Matteo Cacciari, Paolo Nason, and Carlo Oleari. "A Study of heavy flavored meson fragmentation functions in e+ e- annihilation". In: *JHEP* 04 (2006), p. 006. DOI: 10.1088/1126-6708/2006/04/006. arXiv: hep-ph/0510032 [hep-ph].

[17] Matteo Cacciari and Paolo Nason. "Charm cross-sections for the Tevatron Run II". In: *JHEP* 09 (2003), p. 006. DOI: 10.1088/1126-6708/2003/09/006. arXiv: hep-ph/0306212 [hep-ph].

[18] 2016. URL: http://www.lpthe.jussieu.fr/~cacciari/fonll/fonllform.html.

[19] Matteo Cacciari, Michelangelo L. Mangano, and Paolo Nason. "Gluon PDF constraints from the ratio of forward heavy-quark production at the LHC at $\sqrt{S} = 7$ and 13 TeV". In: *Eur. Phys. J.* C75.12 (2015), p. 610. DOI: 10.1140/epjc/s10052-015-3814-x. arXiv: 1507.06197 [hep-ph].

[20] Johan Alwall et al. "A Standard format for Les Houches event files". In: *Comput. Phys. Commun.* 176 (2007), pp. 300–304. DOI: 10.1016/j.cpc.2006.11.010. arXiv: hep-ph/0609017 [hep-ph].

[21] Torbjorn Sjostrand, Stephen Mrenna, and Peter Z. Skands. "A Brief Introduction to PYTHIA 8.1". In: *Comput. Phys. Commun.* 178 (2008), pp. 852–867. DOI: 10.1016/j.cpc.2008.01.036. arXiv: 0710.3820 [hep-ph].

[22] Torbjorn Sjostrand, Stephen Mrenna, and Peter Z. Skands. "PYTHIA 6.4 Physics and Manual". In: *JHEP* 05 (2006), p. 026. DOI: 10.1088/1126-6708/2006/05/026. arXiv: hep-ph/0603175 [hep-ph].

[23] Peter Zeiler Skands. "Tuning Monte Carlo Generators: The Perugia Tunes". In: *Phys. Rev.* D82 (2010), p. 074018. DOI: 10.1103/PhysRevD.82.074018. arXiv: 1005.3457 [hep-ph].

[24] B. Abelev et al. "Measurement of charm production at central rapidity in proton-proton collisions at $\sqrt{s} = 7$ TeV". In: *JHEP* 01 (2012), p. 128. DOI: 10.1007/JHEP01(2012)128. arXiv: 1111.1553 [hep-ex].

[25] Betty Abelev et al. "Measurement of electrons from beauty hadron decays in pp collisions at $\sqrt{s} = 7$ TeV". In: *Phys. Lett.* B721 (2013), pp. 13–23. DOI: 10.1016/j.physletb.2013.01.069. arXiv: 1208.1902 [hep-ex].

[26] Betty Abelev et al. "Measurement of prompt J/ψ and beauty hadron production cross sections at mid-rapidity in pp collisions at $\sqrt{s} = 7$ TeV". In: *JHEP* 11 (2012), p. 065. DOI: 10.1007/JHEP11(2012)065. arXiv: 1205.5880 [hep-ex].

[27] Betty Abelev et al. "D_s^+ meson production at central rapidity in proton–proton collisions at $\sqrt{s} = 7$ TeV". In: *Phys. Lett.* B718 (2012), pp. 279–294. DOI: 10.1016/j.physletb.2012.10.049. arXiv: 1208.1948 [hep-ex].

[28] Jaroslav Adam et al. "Measurement of charm and beauty production at central rapidity versus charged-particle multiplicity in proton-proton collisions at $\sqrt{s} = 7$ TeV". In: *JHEP* 09 (2015), p. 148. DOI: 10.1007/JHEP09(2015)148. arXiv: 1505.00664 [nucl-ex].

[29] René Brun et al. "GEANT Detector Description and Simulation Tool". In: (1994).

[30] Ralf Averbeck et al. "Measurement of electrons from semi-leptonic heavy-flavour hadron decays in p–Pb collisions at $\sqrt{s} = 5.02$ TeV". Analysis note. 2015.

[31] Andrea Dubla. "Low p_{T} nuclear modification factor of electrons from of heavy-flavour hadron decays in central Pb–Pb collision at $\sqrt{s_{\mathrm{NN}}}$ = 2.76 TeV". Analysis note. 2016.

[32] R. Engel and J. Ranft. "Hadronic photon-photon interactions at high-energies". In: *Phys. Rev.* D54 (1996), pp. 4244–4262. DOI: 10.1103/PhysRevD.54.4244. arXiv: hep-ph/9509373 [hep-ph].

[33] R. Engel. "Photoproduction within the two component dual parton model. 1. Amplitudes and cross-sections". In: *Z. Phys.* C66 (1995), pp. 203–214. DOI: 10.1007/BF01496594.

[34] Martin Völkl. "Study of the Transverse Momentum Spectra of Semielectronic Heavy Flavor Decays in pp Collisions at $\sqrt{s} = 7$ TeV and Pb–Pb Collisions at $\sqrt{s_{NN}} = 2.76$ TeV with ALICE". MA thesis. University of Heidelberg, 2012.

[35] Betty Bezverkhny Abelev et al. "Neutral pion production at midrapidity in pp and Pb-Pb collisions at $\sqrt{s_{\mathrm{NN}}} = 2.76$ TeV". In: *Eur. Phys. J.* C74.10 (2014), p. 3108. DOI: 10.1140/epjc/s10052-014-3108-8. arXiv: 1405.3794 [nucl-ex].

[36] P. K. Khandai, P. Shukla, and V. Singh. "Meson spectra and m_T scaling in $p+p$, d+Au, and Au + Au collisions at $\sqrt{s_{NN}} = 200$ GeV". In: *Phys. Rev.* C84 (2011), p. 054904. DOI: 10.1103/PhysRevC.84.054904. arXiv: 1110.3929 [hep-ph].

[37] Jaroslav Adam et al. "Measurement of electrons from beauty-hadron decays in p-Pb collisions at $\sqrt{\mathbf{s}_{\mathrm{NN}}} = \mathbf{5.02}$ TeV and Pb-Pb collisions at $\sqrt{\mathbf{s}_{\mathrm{NN}}} = \mathbf{2.76}$ TeV". In: (2016). arXiv: 1609.03898 [nucl-ex].

[38] Betty Abelev et al. "Measurement of inelastic, single- and double-diffraction cross sections in proton–proton collisions at the LHC with ALICE". In: *Eur. Phys. J.* C73.6 (2013), p. 2456. DOI: 10.1140/epjc/s10052-013-2456-0. arXiv: 1208.4968 [hep-ex].

[39] Michael L. Miller et al. "Glauber modeling in high energy nuclear collisions". In: *Ann. Rev. Nucl. Part. Sci.* 57 (2007), pp. 205–243. DOI: 10.1146/annurev.nucl.57.090506.123020. arXiv: nucl-ex/0701025 [nucl-ex].

[40] R. J. Glauber and G. Matthiae. "High-energy scattering of protons by nuclei". In: *Nucl. Phys.* B21 (1970), pp. 135–157. DOI: 10.1016/0550-3213(70)90511-0.

[41] Jaroslav Adam et al. "Measurement of the production of high-p_{T} electrons from heavy-flavour hadron decays in Pb-Pb collisions at $\sqrt{s_{\mathrm{NN}}}$ = 2.76 TeV". In: (2016). arXiv: 1609.07104 [nucl-ex].

Erklärung:

Ich versichere, dass ich diese Arbeit selbstständig verfasst habe und keine anderen als die angegebenen Quellen und Hilfsmittel benutzt habe.

Heidelberg, den 11. November 2016 . . . . . .